

**MICROFLUIDIC TECHNOLOGIES FOR CONTINUOUS
CULTURE AND GENETIC CIRCUIT
CHARACTERIZATION**

Thesis by
Frederick Kiguli Balagaddé

In Partial Fulfillment of the Requirements
for the Degree of
Doctor of Philosophy

CALIFORNIA INSTITUTE OF TECHNOLOGY

Pasadena, California

2007

(Defended May 30, 2007)

© 2007

Frederick Kiguli Balagaddé

All Rights Reserved

ACKNOWLEDGEMENTS

A doctorate degree does not happen in a vacuum. It starts with a student's vision and utmost commitment. It is then seasoned with the experience, expert advice, inspiration, and guidance of others. I am eternally grateful to my research advisor, Dr. Stephen Quake, who has groomed me to become a first-rate independent researcher. He continuously conveyed a spirit of adventure and excitement in regard to bioengineering research. But above all, I thank him for believing in me.

I am indebted to the members of the Quake group at Caltech and later Stanford University for providing a stimulating environment for intellectual development and research. From the day I joined the group, Carl Hansen played a crucial role in getting me up to speed with microfluidic large scale integration, chip design, and programming and automation using Lab View. I owe him a huge debt of gratitude. Todd Thorsen also got me excited about microfluidics and explained to me the significance of persistence. Informal discussions with Sebastian Maerkl, Emil Kartalov, Robert Bao, Todd Squires, and Heun-Jin Lee were crucial for the success of my research project.

A special line of credit is reserved for the scientists who invented multilayer soft lithography technology, key among them Mark Unger, Hou-pu Chou, Todd Thorsen, Axel Scherer, and Stephen Quake. Without it, my thesis project would not have been possible.

I also thank my collaborators, especially Frances Arnold and Lingchong You, who initiated me into the world of synthetic biology and designed the synthetic circuits that

validated my efforts as far as the utility of the microchemostat is concerned. Jeff Ram has inspired me to take on an active role in furthering the understanding of bacterial chemotaxis using microfluidics.

I am particularly grateful to John Choi, Gentian Buzi, Jimmy Fung, Amos Anderson, Jonathan So, and Terrell Neal for making graduate life at Caltech interesting socially, intellectually, and spiritually. I appreciate my undergraduate teachers at Manchester College, key among them Gregory Clark and James Gaier, who introduced me to research in physics. My undergraduate research mentors at Fermilab; Victor Daniel Elvira and Jay Dittmann encouraged me to pursue the PhD.

Finally, I thank those that are dearest to me, who have loved me unconditionally, and stood by me during times of confusion and frustration. My siblings Connie, Joyce, Angela and Anthony have always believed in my dreams since I was a little child and are a continuous source of encouragement. My brother-in-law, Dr. Andrew Kambugu, has brought a lot of joy and inspiration to my life. My loving wife, Catherine, has helped me get through some of the most difficult challenges that I have faced to date. I thank her for her patience and understanding over the past two years. Her continued support saw me through various critical “tip-over” points, during which the temptation to abscond was vivid. Most importantly, I dedicate this doctoral degree to my parents Sam Balagaddé-Kiguli and Proscovia Namakula Balagaddé, who sacrificed a life of material comfort to put us through the best education programs in Kenya and Uganda. Due to their persistent troubles in Uganda, my native country, I have gained a new and better future within the global village. Particularly, my father ingrained in me the value of higher education in the sciences and

inspired me to travel abroad in its pursuit, as far back as my conscious memory can recall. My mother taught me the virtues of hard work and self-sacrifice as a necessary price for excellence. Their unconditional love, unwavering trust, and constant support have transcended their natural lives and materialized into who I am today. I am forever grateful to them.

Frederick K. Balagaddé

May 17, 2007

ABSTRACT

In this thesis, I have used microfluidics—*the science and technology of systems that manipulate small amounts of fluids (10^{-9} to 10^{-18} liters) in micro-sized channels*—to invent and implement a miniaturized continuous culture device or microchemostat. It relies on a novel *in silicone* sterilization approach to circumventing biofilm formation. The microchemostat system has inbuilt automation, which allows it to run, unattended, indefinitely (for up to months at a time). With a working volume of ~ 10 nL, the microchemostat is capable of culturing extremely small populations of bacteria (100 to $\sim 10^4$ cells vs $\sim 10^9$ in macroscale cultures). The micro-sized population reduces the number of cell-division events per unit time and hence slows down microbial evolution. This aspect facilitates long-term monitoring of the behavior of genetically engineered microbes while preserving their genetic homogeneity. Unlike its conventional continuous-culture counterparts, the microchemostat allows simultaneous operation of fourteen (or more) independent microreactors which enjoy ultralow consumption of medium and biological reagents, allowing high-throughput research at low cost. It also facilitates automated, noninvasive monitoring of bacterial behavior in terms of bacterial count, cell morphology as well as single-cell resolved gene-expression dynamics reported by fluorescence or luminescence. The unprecedented temporal and single cell resolution readings allow the microchemostat to capture dynamics such as delicate oscillations that have eluded detection in conventional settings.

Thanks to its unique capability for long-term culturing and suppression of microbial evolution, the microchemostat promises to become integrated as an ingredient of a multicomponent monolithic entity in future applications. The microchemostat would mainly

be responsible for *in silicone* production and supply of genetically homogeneous bacteria for use in various capacities.

Thesis Advisor: Stephen R. Quake

Title: Professor of Bioengineering, Stanford University

TABLE OF CONTENTS

	Acknowledgements	iii
	Abstract	vi
	Table of Contents	viii
	List of Figures	xii
	List of Tables	xv
Chapter 1:	Overview	1
1.1	Introduction	1
1.2	Organization	2
Chapter 2:	Description of the Chemostat	6
2.1	Introduction	6
2.2	Origins of the Chemostat	7
2.3	Utility of the Chemostat	8
2.4	Operational Drawbacks of Conventional Chemostats	10
2.5	Theoretical Description of the Chemostat	13
2.5.1	The Basic Chemostat Apparatus	13
2.5.2	Microbial Growth at Equilibrium in the Chemostat	15
2.5.3	Substrate-Limited Chemostat Operation	18
2.5.4	Logistic Growth Chemostat Operation	23

Chapter 3:	A Microfabricated Chemostat	25
3.1	Introduction	25
3.2	Fabrication and Design	26
3.2.1	Motivation of the Microchemostat Design	26
3.2.2	A Microchemostat from Soft Lithography	29
3.2.3	Optical Detection and Microscopic Counting	34
3.2.3.1	The Microchemostat Reader	34
3.2.3.2	Microscopic Counting	36
3.2.3.3	Modification to Allow for Monitoring of Multi- Population Cultures	36
3.2.3.4	Microscopic Counting of Mixed Populations	38
3.3	Theory of Chemostat Miniaturization	39
3.3.1	The Effect of Discontinuous Dilution	45
3.4	Results	48
3.5	The Future of Microreactor Design	55
Chapter 4:	Quorum Sensing and Population Control	58
4.1	Introduction	58
4.1.1	Synthetic Biology and the Microchemostat	58
4.1.2	Quorum Sensing in Bacteria	61
4.2	The Population Control Circuit	65

4.3	Results and Discussion	67
4.3.1	Population Control in the Microchemostat	67
4.3.2	Modeling Population Control in the Microchemostat	73
4.4	Materials and Methods	77
4.5	Conclusion	79
Chapter 5:	A Synthetic Predator Prey Ecosystem	80
5.1	Introduction	80
5.2	Predator Prey-Synthetic Ecosystem	81
5.2.1	Circuit Description	81
5.2.2	Circuit Optimization	85
5.3	Results	91
5.3.1	Macroscale Experimental Verification	91
5.3.2	Microchemostat Characterization	94
5.4	Circuit Mathematical Model	103
5.4.1	Simplification of the Model	108
5.4.2	Parameter Values	110
5.5	Materials and Methods	117
5.5.1	Plasmids	117
5.5.2	Strains, Growth Conditions and Macroscale Data Acquisition	119

	xi	
5.5.3	Microchemostat Medium, Preculture Preparation and Growth Conditions	120
5.6	Acknowledgements	121
Chapter 6:	Bacterial Chemotaxis Chip	122
6.1	Introduction	122
6.1.1	Bacterial Chemotaxis	122
6.1.2	Conventional Quantification of Bacterial Chemotaxis	125
6.2	Microfluidic Quantification of Chemotaxis	128
6.2.1	Microfluidic Chemotaxis Interface Chip	128
6.2.2	Experimental Procedure	131
6.3	Results	132
6.3.1	Observation of Chemotaxis on a Chip	132
6.3.2	Longterm Chemotaxis Response	135
6.4	Discussion and Conclusion	139
6.5	Materials and Methods	141
Appendix A:	Chemostat Mathematical Parameters	144
Appendix B:	Fabrication Protocols	145
Appendix C:	Matlab Script for Image Processing	151
Bibliography		156

LIST OF FIGURES

Chapter 2

2.1	Modern conventional chemostat	14
-----	-------------------------------	----

Chapter 3

3.1	Microbial biofilms in microfluidic channels	28
3.2	Microchemostat chip	30
3.3	Optical micrograph of microchemostat reactor	32
3.4	Sequential lysis and the discontinuous dilution scheme	33
3.5	Microchemostat reader schematic	35
3.6	Modification of the growth chamber to allow fluorescent imaging	37
3.7	Microchemostat chip—version 2	38
3.8	Theoretical chemostat growth curves (n vs t) for various reactor volumes	40
3.9	Theoretical chemostat growth curves (ρ vs t) for various reactor volumes	43
3.10	Steady-state density (ρ) vs D for various reactor volumes	44
3.11	Effect of discontinuous dilution on microbial chemostat behavior	47
3.12	Experimental microchemostat growth curves	48
3.13	Experimental graph for steady state density vs D	49
3.14	Effect of discontinuous dilution during actual experiment	51
3.15	Growth rate (μ) vs time in the microchemostat	52
3.16	Curve fitting to logistic and exponential growth equations	53
3.17	Concentric reactor design	56

3.18	240 Microreactor chemostat	57
------	----------------------------	----

Chapter 4

4.1	Genetic circuit engineering process	59
4.2	Population control circuit design schematic	65
4.3	Population control plasmid	66
4.4	Growth of MC4100Z1 under population control	68
4.5	Growth of 'Top10F' under population control	70
4.6	Effect of the dilution rate on population control	72
4.7	Typical simulation of population control dynamics	76

Chapter 5

5.1	Predator-prey circuit diagram	83
5.2	Plausible dynamics of predator-prey	85
5.3	Killing dynamics of $\text{LacZ}\alpha\text{—CcdB}$ and $\text{LacZ}\alpha'\text{-CcdB}$	86
5.4	Quorum-sensing cross talk on solid state medium	89
5.5	Configuration of plasmids in host strains	90
5.6	Response of the predator or prey to IPTG and exogenous AHL	92
5.7	IPTG dose response curves for predator and prey	93
5.8	Microchemostat predator-prey graphs	96
5.9	Predator-prey characterization matrix in the microchemostat	98
5.10	Bifurcation diagram for predator and prey dynamics	100

5.11	Dilution rate dependence of the predator-prey system	101
5.12	Simulation of dilution rate dependent dynamics	102
5.13	Detailed reaction mechanism of the predator-prey ecosystem	103

Chapter 6

6.1	Palleroni chamber	126
6.2	Microfluidic chemotaxis interface module	129
6.3	Schematic of chemotaxis chip	130
6.4	Sample images illustrating bacterial chemotaxis on a chip	133
6.5	Chemotaxis response graphs	134
6.6	Long-term chemotaxis response graph	135
6.7	Zoom in on figure 6.6 showing only the first iteration	136
6.8	Normalized chemotaxis response graph	137
6.9	Difference between serine and aspartate response	138

LIST OF TABLES

Chapter 3

3.1	Logistic and exponential growth constants	54
-----	-------------------------------------------	----

Chapter 5

5.1	Predator-prey model reaction description	112
5.2	Predator-prey model variables	114
5.3	Kinetic parameters of full model	115
5.4	Base values for the key parameters	116

Chapter 1

Overview

“People (graduate students) don’t choose their careers (projects); they are engulfed by them.”

—John Dos Passos, New York Times (October 25, 1959)

1.1 Introduction

The area of micro total analysis (μ TAS), also called “lab on a chip” or miniaturized analysis systems, is growing rapidly(1). Miniaturization enables ultra-low consumption of reagents allowing high throughput research at low cost. It also facilitates automation of experimental processes, which increases speed, precision, accuracy and reproducibility relative to equivalent procedures performed by hand. Other benefits include rapid device prototyping and disposability. A critical mission of this technological juggernaut seeks to integrate high levels of wet laboratory procedures into a single monolithic process on a microfabricated fluidic chip(2, 3). Matter-of-factly, this compulsion has already spread to continuous culture device (chemostat) technology.

This thesis describes the first application of microfluidics to the continuous culture technique, embodied in the development of the microchemostat device. It exploits an *in situ* sterilization paradigm (sequential lysis) to prevent biofilm formation.

The microchemostat has advanced past the proof-of-principle phase and has been extensively used to characterize synthetic genetic circuits, engineered to control the behavior of microbial populations.

A microfluidic chemotaxis device has also been developed for high throughput characterization of microbial chemotactic response to a variety of attractants. This device allows for several different bacterial strains to be tested for chemotaxis against several different attractants or repellants in a parallel fashion.

The technological progress described in this thesis builds upon the Multilayer Soft Lithography (MSL) technology developed previously in our lab by Unger et al(4).

1.2 Organization

The core purpose of chapter 2 is to provide a concise mathematical basis for continuous flow device operation that is relevant to this monograph. I start by describing the canonical chemostat apparatus and then introduce the idea of microbial growth at steady state. Next, I present a concise mathematical basis for all the quantitative arguments made within this monograph. In addition, I derive the relevant equations and models governing microbial growth in the chemostat, within the scope of this thesis. The usefulness and application of the continuous culture technique in laboratory and industrial settings is highlighted. Furthermore, operational bottlenecks that impede widespread use of the continuous culture technology in spite of its obvious advantages are also discussed.

Chapter 3 is a comprehensive description of the microchemostat fabricated according to Microfluidics Large Scale Integration (MLSI) design principles(4). I begin with the underlying forces that motivated the microchemostat design, which exploits a discretized dilution scheme. I spend some time pondering the use of chemical agents such as lysis buffer as a paradigm for *in situ* sterilization of microfluidic chip compartments. The actual fabrication recipes based on Multi-layer Soft Lithography (MSL) from design to device have been conferred to appendix B, to preserve the theoretical line of thought within the chapter. Furthermore, I describe the operation of the entire chemostat chip within the context of the microchemostat reader, including methods for data acquisition (DAQ), data processing and data analysis. The Matlab scripts according to which both the fluorescent and phase contrast images were processed occupy appendix C. Next, I contemplate the theory of chemostat miniaturization by answering the questions: What does it mean to operate a micro-sized reactor volume? What are the consequential benefits and bottlenecks and how should the canonical chemostat equations be reinterpreted? In addition, the decision to adopt the logistic growth in preference to the substrate-limited mode of operation for the microchemostat is defended. I also discuss the effect of the discontinuous dilution scheme employed in microchemostat operation on the steady state. At this point, the characteristic growth curves that were used to characterize the microchemostat are presented. Finally, I explore possible future directions and applications of the continuous flow approach developed in this thesis.

Chapter 4 describes a key application of the microchemostat to characterize a synthetic circuit designed by Lingchong You and Frances Arnold(5) to control cell density population of a microbial population through a quorum sensing based negative feedback loop(6). I begin by highlighting the significance of “synthetic biology”(7-9) both as a science and an engineering paradigm. I then present the microchemostat as a high-throughput screening device that could inexpensively perform rapid characterization of synthetic circuits under a matrix of conditions with unprecedented capabilities: long-term, non-invasive characterization of microbial properties under steady-state conditions with single cell resolving power and advanced automation. Equally important, the microchemostat’s miniaturized working volume of ~ 10 nL is capable of culturing extremely small populations of bacteria ($\sim 10^2$ to $\sim 10^4$ cells versus at least $\sim 10^9$ in macroscale cultures). We showed that this micro-sized population reduces the number of cell-division events per unit time and hence slows down microbial evolution(10). I explain how this aspect facilitated monitoring of programmed population control behavior of bacterial populations for hundreds of hours despite strong selection pressure to evade population control, something that may not be achieved in macroscopic reactors(6). In this chapter, we show that bacterial quorum sensing can take place, even in small microbial populations ($\sim 10^4$ cells).

Along the same lines as the fourth chapter, chapter 5 describes a synthetic predator-prey ecosystem, designed by Lingchong You and Frances Arnold, as well as its characterization in the microchemostat. It consists of two genetically engineered

Escherichia coli populations that communicate through “quorum sensing” and mutually regulate each other’s gene expression and survival via *de novo* engineered regulatory circuits. It resembles the canonical predator-prey system in terms of basic logic and dynamics. A mathematical model developed by Hao Song to predict the plausible system dynamics (e.g., population densities of predator and prey) controlled by the gene circuits. The modified version of microchemostat described in chapter 3 was used to make single-cell resolved fluorescence readings.

Chapter 6 explores microfluidic designs for quantifying bacterial chemotaxis on a chip. Particularly, we investigate the effects of the bacterial physiological state on its ability to chemotax. This work was a collaborative and interdisciplinary venture with Jeffrey Ram’s laboratory at Wayne State University.

Chapter 2

Description of the Chemostat

“The intrinsic advantage of the chemostat lies in the fact that the rate of the dilution also controls the rate of growth...” (11)

2.1 Introduction

A chemostat(12-18) is a piece of laboratory apparatus used for continuous cultivation of microbial populations in a steady state of constant active growth. By continually substituting a fraction of a bacterial culture with sterile nutrients, the chemostat, also known as a continuous culture device or a Continuously Stirred Tank Reactor (CSTR) in engineering literature, presents a near-constant environment ideal for controlled studies of microbes and microbial communities (19-22). It eliminates the artificial lag and stationary growth phase phenomena characteristic for closed (batch) culture systems, creating the technical possibility of measuring microbial activities over indefinitely long periods of time. While steady-state systems are not accurate reproductions of natural conditions, they ascertain the reproducibility of data and offer a possibility of studying one or a few environmental factors at a time with the aim of reconstructing more complex naturally occurring systems from known elements. The

chemostat serves as a model of a simple lake where populations compete for the available nutrients in a purely exploitative manner, which makes it the ideal place to study competition in its most primitive form(21, 23). It is also used as a laboratory model of the wastewater treatment process. Commercially, chemostats play a central role in pharmaceutical (recombinant) protein production using genetically altered organisms (e.g., in the production of insulin). This chapter presents a theoretical and utilitarian description of the chemostat including various growth-limited modes of operation.

2.2 Origins of the Chemostat

The inception of the chemostat in 1950 is attributed to Leo Szilard (1898—1964), a Hungarian-born American physicist and biophysicist, who immigrated to the US in 1938 and became a naturalized citizen in 1943. Working at the University of Chicago with Enrico Fermi, Szilard developed the first self-sustained nuclear reactor based on uranium fission in 1940.

“We turned the switch, saw the flashes, watched for ten minutes, then switched everything off and went home. That night I knew the world was headed for sorrow.”

—Leo Szilard

Having been one of the first to realize that nuclear chain reactions could be used in bombs, Szilard urged the U.S. government to prepare the first atomic bomb as a necessary counter-measure to the possibility of nuclear development and deployment by others. After the Second World War, he actively protested nuclear warfare, and in 1947

Szilard embarked on a new career in biology. In 1950, Szilard and his colleague Aaron Novick invented a different kind of chain reactor, a continuous microbial bioreactor based on binary fission, which they called a chemostat(12). French biologist Jacques Lucien Monod is also recognized for concurrently developing a similar device independently, which he called a “continuous culture device,”(18) nevertheless, it was Szilard who coined the term “chemostat.”

2.3 Utility of the Chemostat

In batch cultures, where nothing is added or removed during the period of incubation, the regime of dynamic growth is bounded on both sides by lag and stationary growth phases that are characteristic of closed systems. Moreover, the growth rate changes over time because of an ever-changing environment: as the organism grows it depletes the nutrients and dissolved oxygen while polluting its environment with waste products. These factors conspire to ultimately suppress the ability of the organism to divide. The chemostat, however, establishes an indefinitely long steady-state period of active growth, which enables long-term experimentation on microbes under essentially invariant conditions. Therefore, the chemostat has become an indispensable tool in the study of microbial metabolism, regulatory processes, adaptations and mutations. It provides constant environmental conditions for microbial growth and product formation(24) and facilitates characterization of microbial response to specific changes in

the growth environment, one factor at a time. From such studies, it is possible to reconstruct the general behavior of microorganisms in their native settings (11, 25).

The ability to control and direct the microbial growth factors in detail is commercially exploited to screen for the conditions that maximize yield in regard to bioprocesses such as pharmaceutical protein production(26) and chemical biotransformation(27) by genetically modified organisms. When multiple species compete for the same growth-limiting substrate in the chemostat, the fastest growing species will prevail because of the constant and indiscriminate removal of cells by dilution. The chemostat can be used to select for the most efficient species for a given set of growth factors out of a pool of species (11, 21).

Strain improvement is the science and technology of manipulating and improving microbial strains in order to enhance their metabolic capabilities for biotechnological applications(28). The uniformity of the chemostat environment subjects a microbial population to strong selection pressure(29) over an indefinitely long period of time. Thanks to spontaneous mutations, mutants with qualities superior to those of the original strain may appear. For example improved growth rate and nutrient uptake(30) as well as ability to degrade toxic refractory compounds(25, 31). A mutant which gains a growth advantage over the others will compete successfully and ultimately displace the slower growing competitors. This process can also be directed by slowly changing the growth conditions in the chemostat, for example, a gradual substitution of glucose with a complex hydrocarbon as the sole carbon source could foster evolution toward degradability of the hydrocarbon. Chemostats are therefore widely employed in

industrial microbial studies to understand the toxicity, carcinogenicity and degradability of complex substrates such as crude hydrocarbons, pesticides and sewage(11, 32).

2.4 Operational Drawbacks of the Conventional Chemostat

Operation of the microbial chemostat is often fraught with difficulties. Microbial biofilms, which exist in virtually all nutrient-sufficient ecosystems(33), attach to growth chamber walls and probe surfaces(33-35) and interfere with continuous bioreactor operation(36). Such microbial wall growth, which is not removable during the course of a dilution, may consume a significant fraction of the growth substrate. This compromises the fixed biomass fundamental conservation principle of the chemostat, and introduces hybrid batch/chemostat characteristics(11). Phenotypically distinct from their planktonic counterparts(33), biofilm cells shed their progeny into the bulk culture and create mixed cultures. At high dilution rates, the captive population, which has an indefinite mean-residence time, supplies most of the bulk-culture cells(37) and prevents the possibility of washout.

The amount of variation in fitness an organism maintains increases as the logarithm of the population size and the mutation rate, which leads to a similar logarithmic increase in the speed of evolution(10). Such evolution can render a continuous culture experiment invalid(21), especially if it alters the desired behavior of

the microbial population. The number of mutations is proportional to the number of cell division events within a unit time period. By maintaining a population in a state of active growth, the chemostat creates susceptibility to mutation and hence evolution.

Accurate quantification of the growth rate of bacteria relies on methods to determine their number at any given point in time. One technique for measuring the size and growth rate of bacterial cultures involves counting bacteria colonies using plating, which relies on the colony-forming ability of viable cells. A sample of an appropriately diluted culture is dispersed on a solid medium and the number of colonies that form is determined. Unfortunately, plating can produce inexact measurements because the culture may continue to grow at an unknown rate during the period of dilution in preparation for plating. In another technique, the total number of cells can be determined microscopically by determining the number of cells per unit area in a counting chamber (a glass slide with a central depression of known depth, whose bottom is ruled into squares of known area). However, this technique is a hands-on, serial process that is prone to human error.

Counting errors may be reduced by using electronic counting devices, such as a Coulter counter, which can determine the size distribution as well as the number of bacteria in a sample culture of known volume. Coulter counters (also known as resistive pulse sensors) are well-developed devices used to measure the size and concentration of biological cells and colloidal particles suspended in an electrolyte. In Coulter devices, an electrolyte solution containing particles is allowed to pass through a microchannel separating two compartments or chambers. When a particle flows through the channel, it

causes a change in the electrical resistance of the channel. The change in resistance can be measured as current or voltage pulses, which can be correlated to size, shape, mobility, surface charge and concentration of the particles(38). Although the counter is rapid and accurate, it is also expensive and subject to a number of artifactual complications. For example, the Coulter counter relies on a pore, through which a known volume of suspension is pumped. This pore is prone to clogging if the media and diluents are not carefully prepared.

Another technique for studying and measuring bacterial cultures involves determining the dry weight of cells in a known volume of suspension. This technique is time consuming and requires a considerable amount of sacrificial culture. As such, it is unsuitable for routine monitoring of the growth rate.

Optical density has also been used to determine growth rates using cell density. However, the correlation between cell density and optical density of the culture may change during production of proteins that may aggregate and form inclusion bodies.

Cells in a culture may differ from each other and the general culture composition may vary depending on environmental growth factors(25, 39). Therefore determining the cell density indirectly by measuring the quantity of some cellular constituent, for example DNA, RNA, protein or peptidoglycan(40) can compromise the accuracy of the measured growth rate.

Continuous bioreactors are also generally challenging and laborious to maintain, consume large amounts of culture medium, and can become expensive to operate when the reagents are pricey.

2.5 Theoretical Description of the Chemostat

From its introduction into microbial research in 1950, much has been written about the description of the chemostat. Therefore only a concise summary of the work originally presented by others (Novick and Szilard(12), Spicer(14), Herbert, Elsworth and Telling(15), Jannasch and Mateles(11), and Smith and Waltman(21)) will be presented.

2.5.1 The Basic Chemostat Apparatus

The chemostat apparatus (figure 2.1) consists of a culture vessel (henceforth referred to as the growth chamber), which contains one or more microbial populations. It also includes a reservoir, which houses sterile growth medium containing the nutrients needed for growth of the cultured microorganism(s). A steady stream of sterile medium flows from the nutrient reservoir to the growth chamber at a constant rate. An overflow on the growth chamber sets the level of the liquid in the growth chamber and imposes a fixed volume of the growth culture. Through this overflow, the displaced bacteria suspension leaves at the same rate at which fresh nutrient enters the growth chamber from the nutrient reservoir. The growth chamber is well stirred and the bacteria are kept homogeneously dispersed throughout the culture at all times. All other significant parameters (e.g., temperature) that may affect growth are kept constant. Due to the continuous flux of medium, the chemostat is often referred to as a “continuous culture” device.

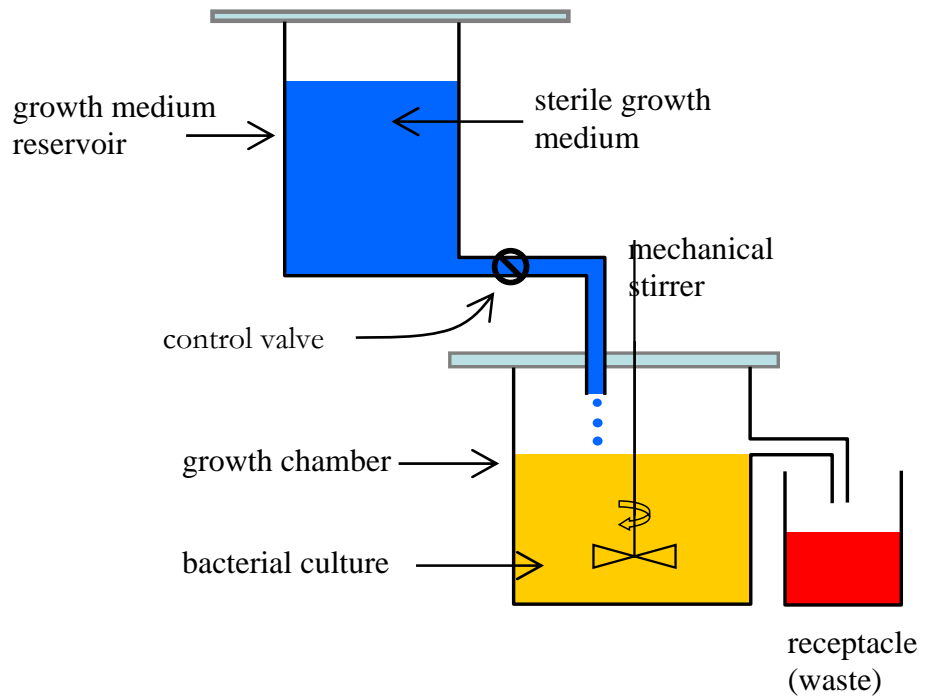


Figure 2.1. A schematic of the modern conventional chemostat.

2.5.2 Microbial Growth at Steady State in the Chemostat

In a limited constant volume of nutrient without continuous flow, an organism in the growth chamber would grow freely. After some period of growth, factors come into play, which depress the power of the organism to divide and eventually stop it from growing altogether. These factors may be of several different kinds: for example exhaustion of nutrient, insufficiency of oxygen, production of toxic metabolites, or direct cell—cell sensing(41). The general effect however, in such a closed environment, is that the growth rate of the population at any time is a function of its size (n) so that

$$\frac{1}{n} \frac{dn}{dt} = f(n), \quad (2.1)$$

where $f(n)$ is some function of n .

For the case with continuous flow (chemostat), let V denote the volume of the growth chamber (V has units of l^3 , where l stands for length), and let w denote the volumetric flow rate (w has units of l^3/t , where t is time). The change of the organism per unit time is the increase of the organism via growth less the fraction removed during washout ($n \cdot [w/V]$), such that

$$\frac{dn}{dt} = nf(n) - n \frac{w}{V}.$$

The quantity $[w/V]$, called the dilution rate (or the washout rate), is denoted by D and has units of t^{-1} . The above equation thus becomes

$$\frac{dn}{dt} = nf(n) - nD. \quad (2.2)$$

The continuous dilution process establishes a continuous influx of fresh growth medium and simultaneously, a steady outflow of toxic metabolites as well as microorganisms. This practice mitigates the factors that would otherwise suppress cell division (such as exhaustion of nutrient, insufficiency of oxygen, toxic metabolite production, or microbial overcrowding(41), and facilitates continuous binary fission, essentially maintaining the population in a state of active growth. After a certain time of such operation, a stationary steady state ($dn/dt = 0$) is reached in the growth chamber characterized by a constant microbial population, whose growth rate is equal to the dilution rate. In other words, the chemostat culture gravitates toward a steady state condition, during which the microbial growth rate is just sufficient to replenish the cells lost in the effluent during the dilution process, establishing constant cell density. This steady-state cell density may be varied by changing the dilution rate or growth limiting factors such as the chemical composition of the incoming medium (equations (2.13) and (2.24)).

At steady state, equation (2.2) thus becomes:

$$\frac{dn}{dt} = nf(n) - nD = 0, \quad (2.3)$$

and the dilution rate required to maintain a population of a given population size is given by solving the equation $f(n) = D$.

At the steady state population denoted as n_{ss} , $D = f(n_{ss})$. Such steady state is not necessarily stable. For instance, if the population of a given size is growing exponentially, it is not possible in practice to maintain a constant number by simply renewing the medium as small discrepancies between the growth rate of the organism

and the turnover of the medium always occur which result in either washing out of the organism or growth. Generally, if the steady state population n_{ss} accidentally becomes $(n_{ss} + \eta)$, where $\eta \ll n_{ss}$ we have

$$\frac{d(n_{ss} + \eta)}{dt} = (n_{ss} + \eta)f(n_{ss} + \eta) - D(n_{ss} + \eta).$$

Given that η is small, $f(n_{ss} + \eta)$ can be expanded as a Taylor series and ignoring terms in η^2 and higher powers of η to yield,

$$\frac{d\eta}{dt} = (n_{ss} + \eta)(f(n_{ss}) + \eta f'(n_{ss})) - D(n_{ss} + \eta).$$

Since at steady state $D = f(n_{ss})$,

$$\frac{d\eta}{dt} = \eta n_{ss} f'(n_{ss}). \quad (2.4)$$

For such an equilibrium to be stable any change in η must cause an opposite change in dn/dt , i.e., if η is positive dn/dt must be negative and vice versa. So in general, there can be no stability unless the growth rate decreases as the concentration of organism increases. In other words, at the equilibrium population n_{ss} , the function $f(n)$ must of necessity decrease as n increases.

The function $f(n)$ can take on many forms depending on the prevailing growth-limiting factors, which may include growth nutrient concentration, production of a toxic metabolite and direct cell—cell sensing. Below, I present mathematical descriptions for chemostats for key functions of $f(n)$.

2.5.3 Substrate-Limited Chemostat Operation

During substrate-limited chemostat operation the composition of the fresh sterile nutrient is prepared to contain all of the nutrients needed for growth of the cultured microorganism(s)—all in excess except for one, which is referred to as the growth-limiting nutrient. Let $S(t)$ denote the concentration of the culture in the growth chamber at time t . The concentration of the growth-limiting nutrient in the reservoir, denoted by $S^{(0)}$ has units of $mass/L^3$ and is kept constant throughout the experiment. Thus $VS(t)$ denotes the amount of nutrient in the growth chamber at that time. If there were no organisms to consume nutrients in the growth chamber, the rate of change of nutrient would simply be the difference between the net nutrient flux effected by dilution $(S^{(0)}w - S(t)w)$ or

$$\frac{d}{dt}[VS(t)] = S^{(0)}w - S(t)w.$$

Note that the units on each side are $mass/time$. Since V is constant, the quantity on the left can be written as $VS'(t)$ and both sides divided by V to yield the equation

$$\frac{dS(t)}{dt} = D(S^{(0)} - S(t)).$$

The presence of microorganisms consuming nutrients in the growth chamber invites an additional consumption term, which is a function of the population size n and the nutrient concentration S , expressed as $F_1(S, n)$. Thus

$$\frac{dS(t)}{dt} = D(S^{(0)} - S(t)) - F_1(S, n). \quad (2.5)$$

Concurrently, equation (2.2), corresponding to the rate of change of the number of organisms takes on the form

$$\frac{dn}{dt} = nF_2(S) - nD, \quad (2.6)$$

where $F_2(S)$ is a function describing the microbial specific growth rate, which depends on the nutrient concentration S .

Monod(18) described the relationship between the specific growth rate $F_2(S)$ and nutrient concentration as a data-fitting function

$$F_2(S) = \frac{1}{n} \frac{dn}{dt} = \mu_m \frac{S}{K_S + S}, \quad (2.7)$$

Where μ_m is the maximum specific growth rate (units are $1/t$), and K_S is the Michaelis-Menton (or half-saturation) constant, numerically equal to the limiting substrate concentration at which half of the maximum specific growth rate is reached with units of concentration. Both K_S and μ_m can be determined experimentally by measuring the growth rate as a function of nutrient concentration and fitting the data obtained to equation (2.7). The quantity $\mu_m \frac{S}{K_S + S}$ is often simply referred to as μ .

Monod also showed that the number of organisms formed is directly proportional to the nutrient uptake for a range of concentrations(18). The constant of proportionality γ is also known as the “yield” coefficient. Thus

$$(\text{number of organisms formed}) = \gamma (\text{mass of substrate used}),$$

and γ can be determined experimentally in batch culture by measuring

$$\frac{\text{number of organisms formed}}{\text{mass of substrate used}},$$

and hence has dimensions of $1/\text{mass}$. That γ is constant over the entire range of nutrient concentrations is a hypothesis, and the assumption that reproduction is proportional to nutrient uptake is a vast simplification(11). Nevertheless, the veracity of this assumption rests beyond the scope of this monograph. Mathematically,

$$\frac{dn}{dt} = -\gamma \frac{dS}{dt}. \quad (2.8)$$

Combining equations (2.7) and (2.8), we get the expression for nutrient consumption $F_1(S, n)$ term in equation (2.5).

$$F_1(S, n) = \frac{dS}{dt} = -\mu_m \frac{S}{K_S + S} \frac{n}{\gamma}. \quad (2.9)$$

The chemostat differential equations (2.5) and (2.6) for S and n then take on the forms

$$\frac{dS}{dt} = S^{(0)}D - SD - \mu_m \frac{S}{K_S + S} \frac{n}{\gamma}, \text{ and} \quad (2.10)$$

$$\frac{dn}{dt} = \mu_m \frac{Sn}{K_S + S} - Dn. \quad (2.11)$$

At steady state the time derivatives of the cell density n and substrate concentration S vanish, yielding the equilibrium expressions for the growth-limiting nutrient concentration S_{SS} and the cell density n_{SS} :

$$S_{SS} = \frac{DK_s}{\mu_m - D}, \text{ and} \quad (2.12)$$

$$n_{SS} = \gamma(S^{(0)} - S_{SS}) = \gamma S^{(0)} - \frac{\gamma DK_s}{\mu_m - D}. \quad (2.13)$$

It is worth noting that at steady state, the concentration of the limiting substrate is independent of its concentration in the reservoir, but dependent on the dilution rate (equation (2.12)). At the same time, the population density becomes a function of the concentration of the growth substrate in the reservoir and the dilution rate (equation (2.13)).

The principle of substrate-limited growth in continuous culture is experimentally easier to realize when the population density is maintained at a low value and, therefore secondary effects such as partial growth limitation by oxygen or metabolic products, are kept at bay(11). From equation (2.13), we see that the steady-state population density can be decreased by reducing the concentration of the growth-limiting factor S^0 in the incoming medium (storage reservoir). The steady-state cell density can simultaneously be suppressed by working at high dilution rates. The dilution rate must always be regulated with extreme caution because it is liable to exceed the maximum specific growth rate μ_m and result in complete washout of the cultured organism (equation (2.13)). Substrate-limited operation of the chemostat also requires that the growth limiting nutrient S^0 be

kept in such a limiting quantity that it becomes the overriding factor in setting the steady-state cell density (equation (2.13)). At the same time, the concentration of all other growth nutrients in the growth chamber remains so high that they bear no appreciable effect on the growth rate as well as the steady-state cell density of bacteria. Mathematically at a sufficiently low concentration of the growth limiting factor ($S \ll K_S$), the growth rate equation (2.7) becomes a linear function of the concentration of the growth-limiting nutrient.

$$\frac{1}{n} \frac{dn}{dt} \approx \frac{\mu_m}{K_S} S. \quad (2.14)$$

Taking the simplification of equation (2.14) into account, the governing equations of the substrate-limited chemostat become:

$$F_1(S, n) = -\frac{\mu_m}{K_S \gamma} n S, \quad (2.15)$$

$$F_2(S) = \frac{\mu_m}{K_S} S, \quad (2.16)$$

$$\frac{dn}{dt} = \frac{\mu_m}{K_S} S n - D n, \text{ and} \quad (2.17)$$

$$\frac{dS}{dt} = D(S^0 - S) - \frac{\mu_m}{K_S \gamma} S n. \quad (2.18)$$

Similarly, the steady-state expressions for the cell density n_{ss} and the growth-limiting nutrient concentration S_{ss} simplify to

$$n_{ss} = \gamma(S^0 - S_{ss}) = \gamma S^0 - \gamma \frac{K_s}{\mu_m} D. \quad (2.19)$$

$$S_{ss} = \frac{K_s}{\mu_m} D. \quad (2.20)$$

Low steady-state cell density, implicit in substrate-limited chemostat operation (equation (2.13)), makes this approach unideal for miniaturized chemostat operation as will be discussed in chapter 3.

2.5.4 Logistic Growth Chemostat Operation

Consider a population of microbes in a growth chamber of nutrients without continuous flow. While the population is small, growth-limiting factors such as nutrients, physical space, and dissolved oxygen, which foster exponential growth, abound. As the population increases, the aforementioned growth factors become scarce while the concentration of toxic metabolites increases. This argument establishes the cell-density itself as the major intraspecific force(14) (equation (2.1)) governing the growth rate. The population increases toward a stable level known as the carrying capacity which we denote as N_∞ , which represents the absolute maximum number of individual microbes based on the amount of the growth resources available. The density-dependence of

growth dynamics of a population of size (n) is captured in the canonical “Logistic Growth Equation”(14) as:

$$\frac{1}{n} \frac{dn}{dt} = \mu \left(1 - \frac{n}{N_\infty} \right), \quad (2.21)$$

where μ is the specific growth constant. As a first approximation, microbial growth in a chemostat can be considered to be growing logistically while being simultaneously washed out, which gives the differential equation

$$\frac{1}{n} \frac{dn}{dt} = \mu \left(1 - \frac{n}{N_\infty} \right) - D, \quad (2.22)$$

whose analytic solution is

$$n(t) = \frac{n_0 N_\infty (\mu - D)}{n_0 \mu + (N_\infty \mu - n_0 \mu - N_\infty D) e^{-(\mu - D)t}}, \quad (2.23)$$

where n_0 is the initial absolute population size.

The steady-state expressions for the cell density n_{SS} , obtained by setting $\left(\frac{dn}{dt} = 0\right)$ in equation (2.22), becomes

$$n_{SS} = \left(1 - \frac{D}{\mu} \right) N_\infty, \quad (2.24)$$

such that theoretically any desired population can be maintained by dialing in the appropriate dilution rate D , as long as D does not exceed the specific growth rate μ .

Chapter 3

A Microfabricated Microchemostat

“It's not the size of the dog in the fight; it's the size of the fight in the dog.”

—Mark Twain

3.1 Introduction

The area of micro total analysis (μ TAS), also called “lab on a chip” or miniaturized analysis systems, is growing rapidly(1). Miniaturization enables ultra-low consumption of biological samples and reagents allowing high-throughput research at low cost. It also facilitates automation of experimental processes, which increases speed, precision, accuracy and reproducibility relative to equivalent procedures performed by hand. A capital goal of this technological movement seeks to integrate high levels of wet laboratory procedures into a single monolithic process on a microfabricated fluidic chip(2, 3). Matter-of-factly, this compulsion has already spread to continuous culture device (chemostat) technology. The theory of miniaturization as well as the physics of fluids in small dimensions have been holistically described elsewhere (1, 3, 42). In this chapter, I present my progress in developing the microchemostat in three sections. Section 3.2 describes the fabrication and design of the microchemostat and its

experimental setup (the microchemostat reader). In section 3.3, I discuss the theoretical implications of chemostat miniaturization from the perspective of a microchemostat. In addition, the decision to adopt the logistic growth as opposed to the substrate-limited mode of operation for the microchemostat is defended. In section 3.4, the characteristic growth curves that were used to characterize the microchemostat are presented.

3.2 Fabrication and Design

The microchemostat was fabricated according to the principles of microfluidic large scale integration (MLSI) (43) (appendix B) and the plumbing structure described in section 3.2.2. Before explaining the workings of the chip, we begin by elucidating the underlying forces that motivated the microchemostat design and operation scheme.

3.2.1 Motivation of the Microchemostat Design

During chemostat operation, a major obstacle in reaching steady state stems from biofilm formation, when cultured microorganisms attach to growth chamber walls and probe surfaces(33-35) (section 2.4). Whereas wall growth effects may be ignored in macroscale reactors, the increase in surface area-to-volume ratio as the working volume is decreased aggravates these effects (37), which further complicates the challenge of engineering a miniaturized chemostat or microchemostat. We observed that *E. coli* bacterial cultures thrive while encapsulated in silicone elastomeric (General Electric RTV 615) micro-chambers, albeit with a high propensity for wall growth. Biofilm formation

typically began with wall-adhesion events involving one or more cells. Apparently, the progeny of such wall adherent cells remained sessile (as opposed to joining the planktonic population) and contributed to the formation of biofilms. Thus, upon nucleation, the size of each biofilm increased exponentially. Portions of mature biofilms routinely broke away from the parent biofilm and were carried through the medium to different sections of the reactor, where they took root, and continued to increase in size. Ultimately, biofilms always clogged entire passageways of the microsized channels, preventing the possibility of nutrient influx, culture mixing, steady state, and wash out (figure 3.1).

The original approach for control of biofilm formation in the microchemostat involved treatment of microfluidic growth chamber surfaces with non-adhesive surface coatings (such as poly (ethylene glycol) (PEG), ethylenediaminetetraacetic acid (EDTA), polyoxyethylene sorbitan monolaurate (Tween-20) and bovine serum albumin (BSA)), prior to introducing microbial cultures. Although there was significant reduction in cell wall adhesion, the inevitable mechanical action of Quake valves(44) within plumbing components such as peristaltic pumps (4) trapped and encouraged cells to stick to the walls, provoking biofilm formation. Any such adherent cells became potential nucleation sites for biofilm formation. It is also possible that continuous flow operation in the earlier designs gradually eroded the aforementioned surface coatings. The success of this approach was therefore short lived and ultimately biofilms invaded the fluidic channels within ~48 hours(45) and overthrew the continuous-flow system before steady state operation materialized.

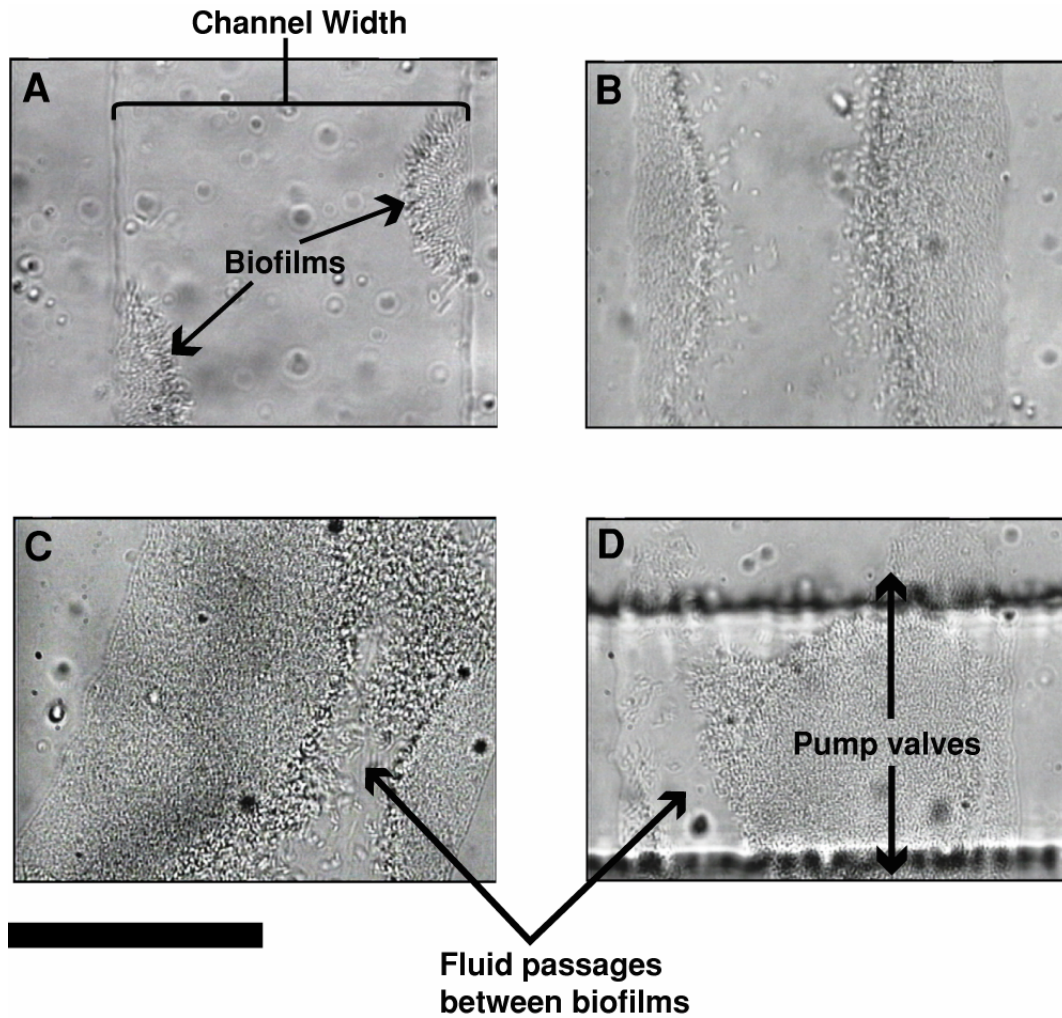


Figure 3.1. (A–C) Optical micrographs of typical scenarios in the absence of active biofilm control (section 3.2.2) depicting invading biofilms that stemmed from passive adhesion. In (C), two biofilms invading from either side of the growth chamber are about to osculate and clog the fluid channel. (D) A biofilm in between the valves of a peristaltic pump initiated by Quake valve mechanical operation. The scale bar is 100 μm long.

During standard continuous culture operation, contamination takes place when the microbial population grows into the sterile nutrient reservoir. Conventionally, this can be prevented by drop-wise introduction of the fresh nutrients, which maintains a physical space barrier between the fermenting culture and the sterile nutrient reservoir. In a monolithic microfluidic interface, such drop-wise feeding is implicitly unfeasible. In the original microchemostat designs, such a barrier was imposed using mechanical Quake valves to separate the fermenting culture from the line feed coming from the nutrient reservoir. Whenever such valves were open to infuse fresh nutrients into the growth chamber, the cultured cells were presented with an opportunity to chemotax and swim toward the nutrient reserve. Therefore, chemotaxis, the bias random walk of motile bacterial cells toward nutrients, presents another major challenge for microchemostat implementation. A single cell migrating back through the feed line to the medium reservoir would rapidly contaminate the medium and render the experiment invalid(46).

A successful microchemostat design would have to simultaneously control the formation of biofilms, prevent chemotaxisal contamination and perform cell culture dilution.

3.2.2 A Microchemostat from Soft Lithography

Using the well-documented microfluidic plumbing technology of pneumatically activated Quake valves, mixers and pumps that was developed in our group(4, 47) and a sequential lysis scheme to prevent biofilm formation, I created a miniaturized, chip-based

chemostat (figure 3.2). The chip was fabricated out of silicone elastomer polydimethylsiloxane (PDMS) (General Electric RTV 615) using microfluidics large scale integration (MLSI) (4, 43, 47) as described in appendix B.

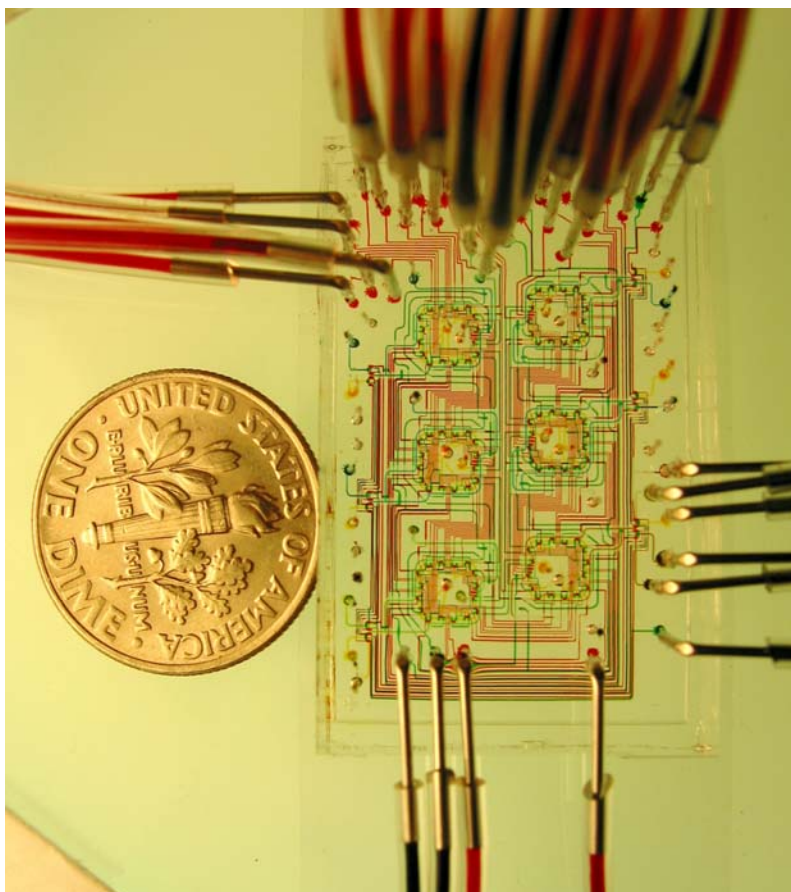


Figure 3.2. Six microchemostats that operate in parallel on a single chip. Various inputs have been loaded with food dyes to visualize channels and subelements of the microchemostats. The coin is 17.91 mm in diameter.

This device allows semicontinuous, planktonic growth in six or more independent 16-nanoliter reactors with minimal wall growth. Each culture can be monitored *in situ* by optical microscopy to provide automated, real-time, non-invasive measurement of cell density and morphology with single-cell resolution.

Each reactor, or ‘microchemostat’, consists of a growth chamber, which is a fluidic loop 10 μm high, 140 μm wide and 11.5 mm in circumference, with an integrated peristaltic pump and a series of micromechanical valves to infuse fresh medium and expel the effluent. Two input/output ports were incorporated within the growth loop perimeter for introduction of bacterial inoculum, removal of waste during the experiment, and recovery of cells if need be. (figure 3.3). The growth loop is encircled by two supply channels (feed lines), which connect to four substrate input ports on one end and an overflow waste port on the other. The growth loop is itself composed of 16 individually addressable, albeit connected segments (figure 3.4). The microchemostat operates in one of two alternating states: (a) continuous circulation and (b) cleaning and dilution. During continuous circulation, the peristaltic pump circulates the culture around the growth loop at a linear velocity of about $250 \mu\text{m s}^{-1}$ to agitate the culture and keep it well-mixed with the nutrients (figure 3.4 B).

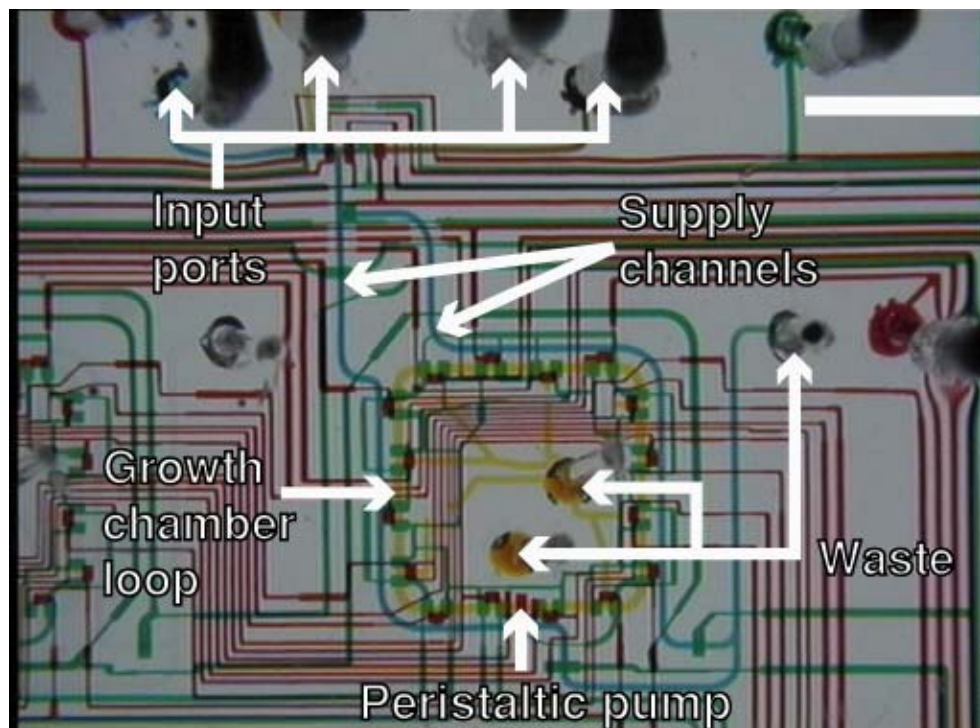


Figure 3.3. Optical micrograph showing a single microchemostat and its main components. Scale bar, 2 mm.

During cleaning and dilution (figure 3.4 A), the mixing is halted and a segment is isolated from the rest of the reactor using Quake valves. A lysis buffer coming from one of the input ports via a supply channel is flushed out through one of the output ports enclosed by the growth loop through the isolated segment for 50 seconds to expel the cells it contains, including any wall-adhering cells. Next, the segment is flushed with sterile growth medium to completely rinse out the lysis buffer. This segment, sterilized and filled with fresh medium, is then disconnected from the supply channel and the output, reunited with the rest of the growth chamber at which point continuous

circulation resumes. Repeated cyclically with controllable circulation durations, cleaning a different growth chamber segment each time, this process circumvents biofilm formation and effects pseudocontinuous operation.

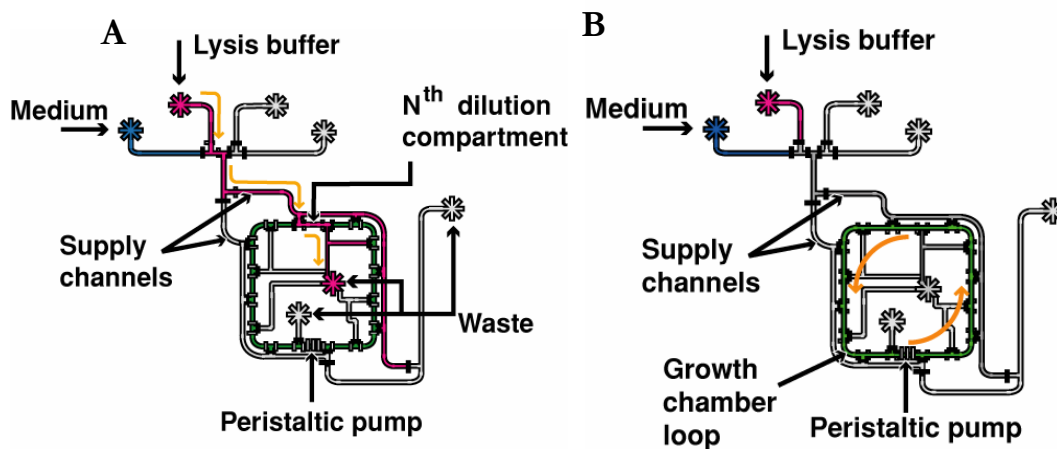


Figure 3.4. (A) Isolation of a segment from the rest of the growth chamber. Lysis buffer (indicated in red) is introduced into the chip through the “lysis buffer in” port. Integrated microvalves direct buffer through the segment, flushing out cells, including those adhering to chamber walls. (B) The segment is then rinsed with fresh sterile medium and reunited with the rest of the growth chamber.

Simultaneously, this scheme prevents chemotaxis back growth⁽⁴⁶⁾ of bacterial cells into the medium feed channel. During a dilution event, when the isolated segment being washed out is first opened to the supply channel, the cells encounter the lysis buffer,

which destroys and flushes them through the waste port. When the sterile nutrient is subsequently introduced, it finds the segment void of any cells, which removes any possibility for cells to chemotax toward the sterile nutrient reserve. Intruding cells would have to endure the lethal environment created by the lysis buffer. Even though preventing back growth was not the primary motivation of behind sequential dilution scheme, the lysis buffer approach presents an overwhelming deterrent to any cell trying to reach the nutrient reserves and thwarts contamination.

3.2.3 Optical detection and Microscopic Counting

3.2.3.1 The Microchemostat Reader

The reader (figure 3.5) consists of a Nikon TE 2000 (A. G. Heinze, Lake Forest, CA) inverted microscope furnished with a PRIOR Scientific XYZ motorized stage system (A. G. Heinze, Lake Forest, CA). Imaging is done using a Plan Fluor 40X 0.75NA ph2 DLL objective. The cells in the microchemostat could be illuminated by bright light (from microscope light bulb) or excitation light originating from the UV mercury lamp, through the appropriate filterset. Illumination in each case was synchronized to chip functions using two shutters (Uniblitz electronic shutters, A. G. Heinz, Lake Forest, CA). Fluorescent or phase-contrast digital images were captured using a cooled coupled charged device (CCD) camera (monochrome Retiga SRV 2000 RV from QImaging Corporation, Surrey, BC, Canada). We developed Lab View software to control the synchronized operation of these components and all chip operation.

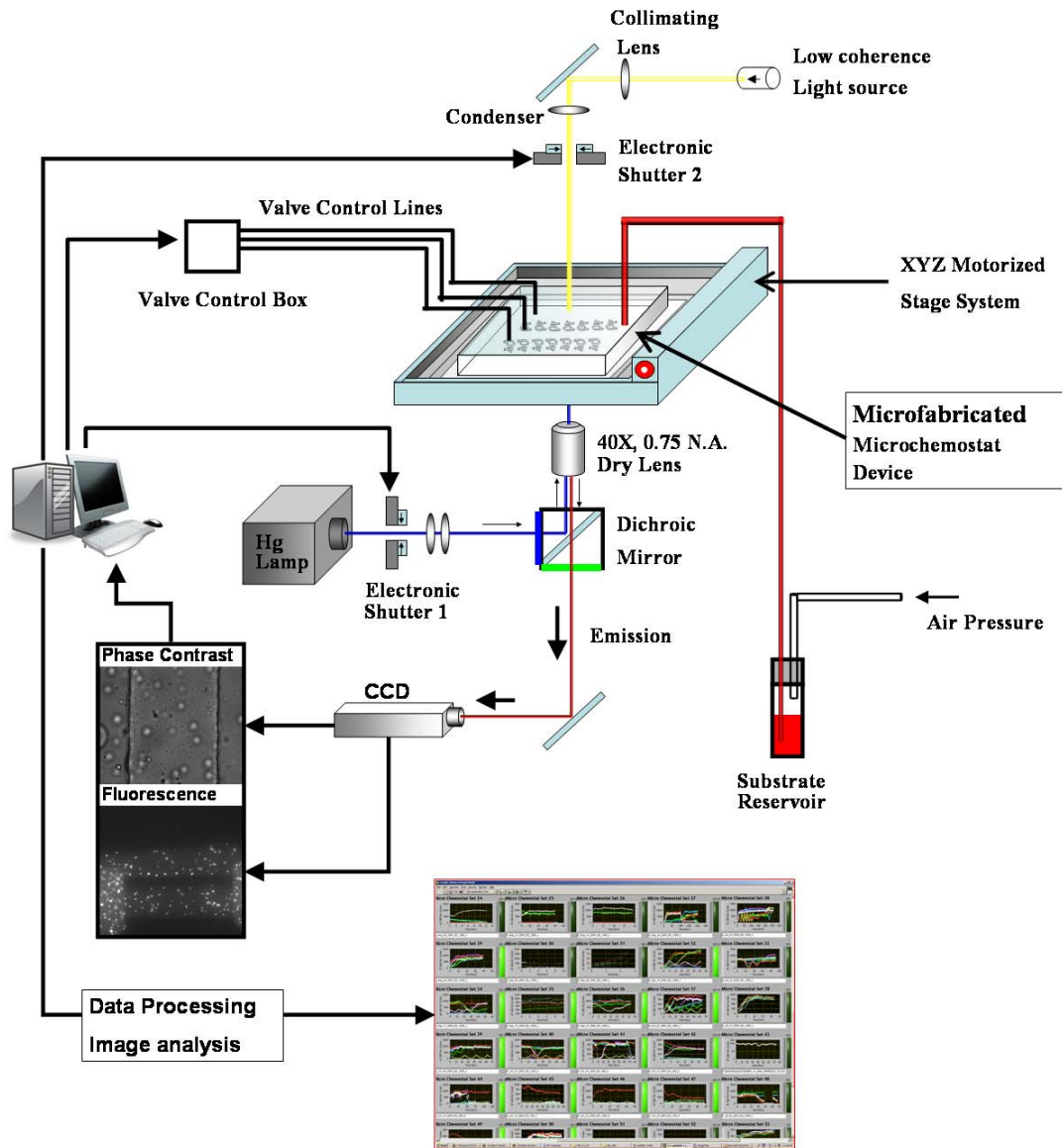


Figure 3.5. Schematic of the microchemostat reader

3.2.3.2 Microscopic Counting

The microchemostat architecture is such that all the cells dwell in a chamber 10 μm high, which is the equivalent of a single focal plane of the Plan Fluor 40X 0.75NA ph2 DLL objective. As such, the total number of cells in each continuous reactor was determined through automated microscopy by counting the number of cells present in a growth chamber section of known volume. A set of 8 still images was taken at a given location of each reactor, with rotary mixing of the culture in between consecutive snapshots. We developed image-processing algorithms in Matlab to determine the average number of cells in each picture set, from which the total cell count were determined. The motorized stage system enabled simultaneous documentation of multiple microchemostat experiments on a single chip.

3.2.3.3 Modification to Allow for Monitoring of Multi-Population Cultures

In a later chip version, the number of reactors per chip was increased from six to fourteen (figure 3.7). In addition, a thin imaging section $\sim 3 \mu\text{m}$ high (compared to $\sim 10 \mu\text{m}$ high otherwise) was incorporated along a 150 μm stretch of the growth loop to constrain the entire fluorescent signal of the cells within a single focal plane (figure 3.6).

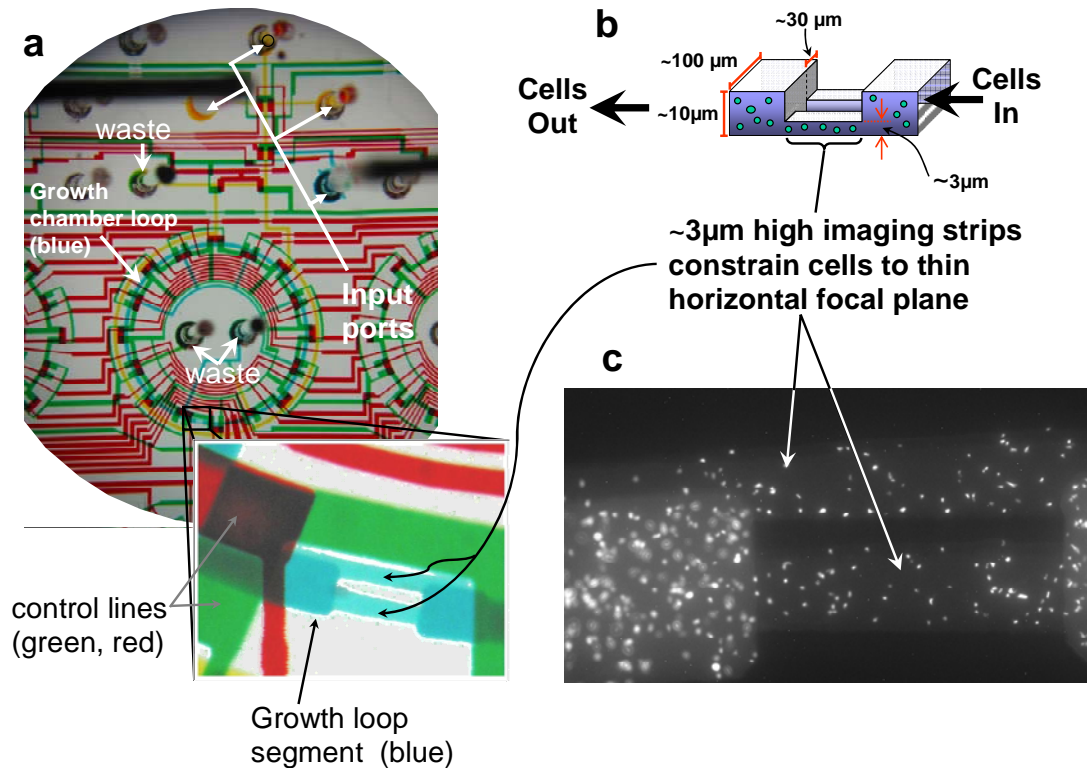


Figure 3.6. Modification of the microchemostat to allow for accurate fluorescent imaging. a) New microchemostat reactor with circular growth chamber loop. The imaging section has been enlarged to show the $\sim 3 \mu\text{m}$ high strips. b) Three-dimensional schematic of the imaging section along the growth loop. c) Sample fluorescent image, showing better resolution of cells in the $\sim 3 \mu\text{m}$ strips.

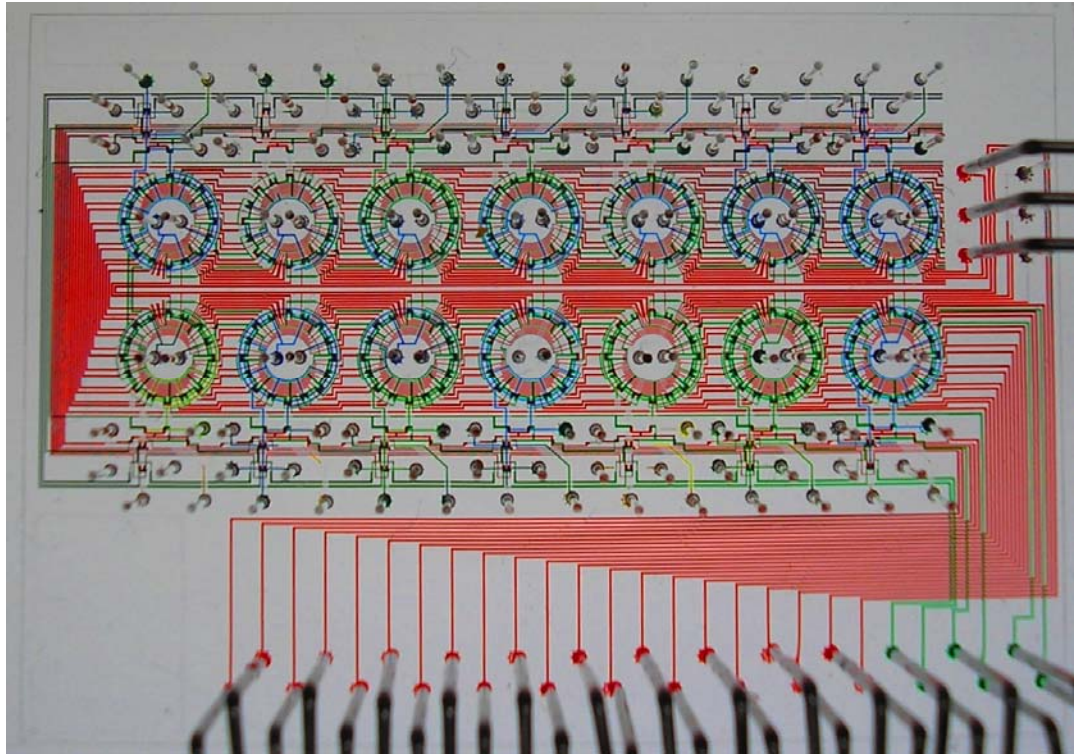


Figure 3.7. Fourteen chemostats that operate in parallel on a single chip. Various inputs have been loaded with food dyes to visualize channels and sub-elements of the microchemostats. The height of the chip is 38mm.

3.2.3.4 Microscopic counting of Mixed Populations:

The $3\mu\text{m}$ height of the imaging section (compared to the $10\mu\text{m}$ height otherwise) constrained the cells within the region of interest into a single focal plane so that they could all be in focus simultaneously, given a single Z-axis focus coordinate. It also

enhanced the single-cell resolvability by decreasing the cell-cell overlap in the horizontal plane.

The total number of cells in each continuous reactor was determined directly through automated bright-field microscopy according to the scheme described in section 3.2.3.2. The density of fluorescently labeled cells could also be determined when needed from a set of four fluorescence images taken using the appropriate filter set. This method of determining the cell density enabled us to perform experiments involving mixed bacterial populations in which each species was tagged with unique fluorescent labels. For example, during synthetic ecosystem studies discussed in chapter 5, one of the “predator-prey” pair was labeled with a fluorescence protein reporter (GFP uv). The number of fluorescent cells was ascertained directly through fluorescence microscopy. Thus, the non-fluorescent density was calculated by subtracting the fluorescent from the total count.

3.3 Theory of Chemostat Miniaturization

An implicit consequence of miniaturizing the chemostat’s active volume is a reduction in the absolute number of microbial cells that can be cultured. For a given cell density ρ (# cells per unit volume), reduction in the reactor volume V translates into a proportionate reduction in the absolute number of cells n that can be housed in accordance to the simple, albeit canonical, density equation; $\rho = n/V$.

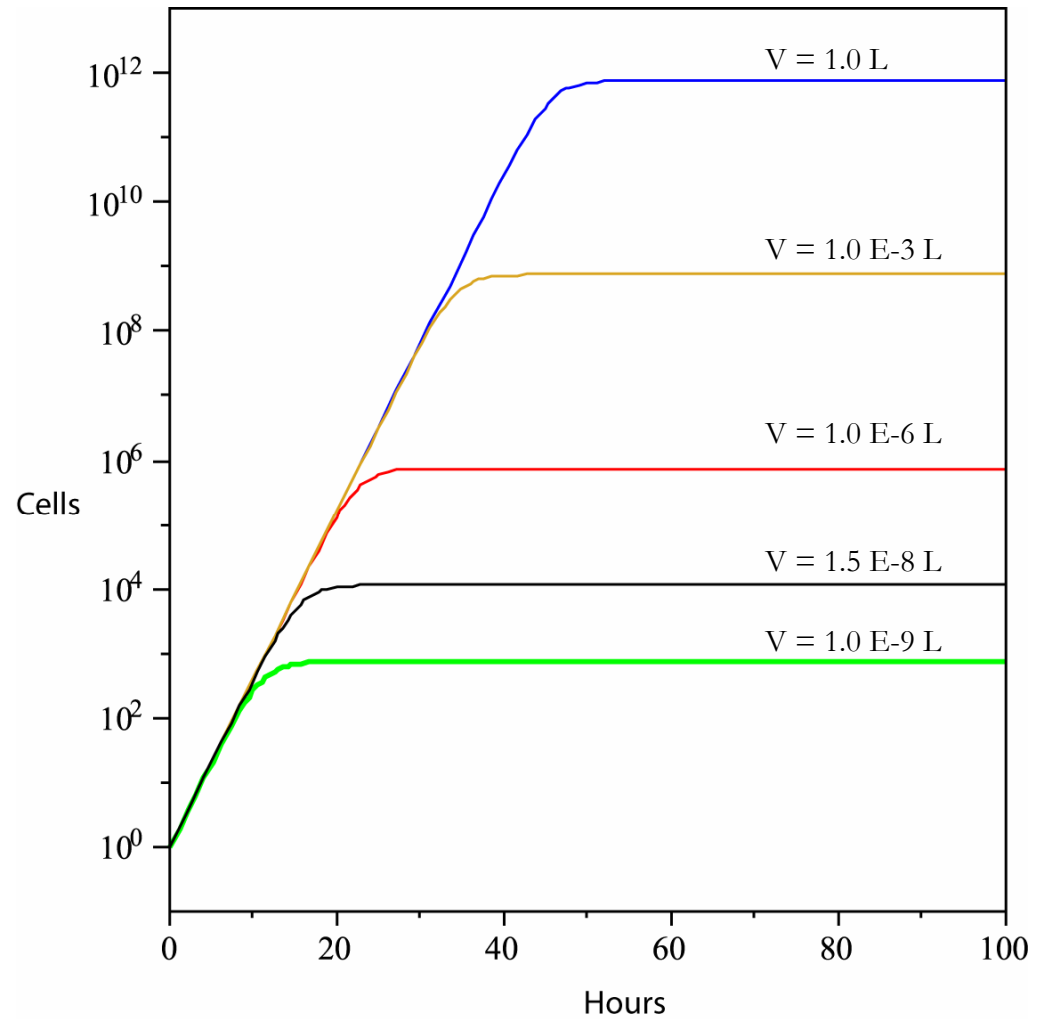


Figure 3.8. Chemostat growth ($n(t)$ Vs t) curves for various reactor volumes generated according to equation (2.23) under otherwise similar conditions ($n_0=1$, $\mu=0.8 \text{ hr}^{-1}$, $D=0.2 \text{ hr}^{-1}$, and $N_\infty=10^9 \text{ cells/mL}$).

A microchemostat with a miniaturized working volume is capable of culturing extremely small populations of bacteria ($\sim 10^4$ cells versus $\sim 10^9$ in macroscale cultures). Figure 3.8 shows theoretical chemostat graphs for various reactor volumes generated according to equation (2.23) under otherwise similar conditions ($n_0 = 1$, $\mu = 0.8 \text{ hr}^{-1}$, $D = 0.2 \text{ hr}^{-1}$, and a carrying capacity of 10^9 cells/mL). The micro-sized population reduces the number of cell-division events per unit time and hence slows down microbial evolution(10). This aspect facilitates monitoring of bacterial populations that remain genetically homogeneous over long periods of time(6). As the reactor volume shrinks, the “surface area”-to-volume ratio increases dramatically. A large “surface area”-to-volume ratio aerates the micro-culture better and theoretically increases the concentration of dissolved oxygen on one hand but aggravates the effects of biofilm formation effects (37) on the other.

On the other hand, regardless of the reactor volume, each culture theoretically attains the same steady state cell density (figure 3.9). Nevertheless, higher dissolved oxygen concentrations in smaller reactor volumes could increase the cultures carrying capacity and hence the steady state cell density attained.

For the same absolute size of inoculum, the time a population takes to arrive at steady-state scales as a logarithm of the volume. Combining equations (2.23) and (2.24), the time $T_{SS,x}$ it takes a population to arrive within $x\%$ of its steady-state can be expressed as:

$$T_{SS,x} = \frac{1}{(\mu - D)} \ln \left[\frac{V \left(1 - \frac{D}{\mu} \right) \rho_{\infty} - 1}{\frac{1}{x} - 1} \right], \quad (3.1)$$

where $\rho_{\infty} = N_{\infty}/V = \text{constant}$. The minimum attainable cell density ($\rho_{\min} = 1/V$, corresponding to 1 cell per reactor volume) increases proportionately as the working volume shrinks. This sets a lower limit to volume miniaturization, for a given cell density, below which cell culturing would result in no cells in the entire reactor. Additionally, as the reactor volume shrinks, the dynamic range of attainable cell densities decreases ($[\rho_{\infty} - \rho_{\min}(V)] = [\rho_{\infty} - 1/V]$). Therefore small bioreactors may be unsuitable for experiments requiring low cell density.

The theoretical description of continuous culture requires growth to be limited by only one factor or substrate throughout the experiment. In the case of substrate-limited operation, the growth limiting nutrient concentration needs to be present in such a limiting quantity that small variations in its concentration can cause corresponding variations in the growth rate.

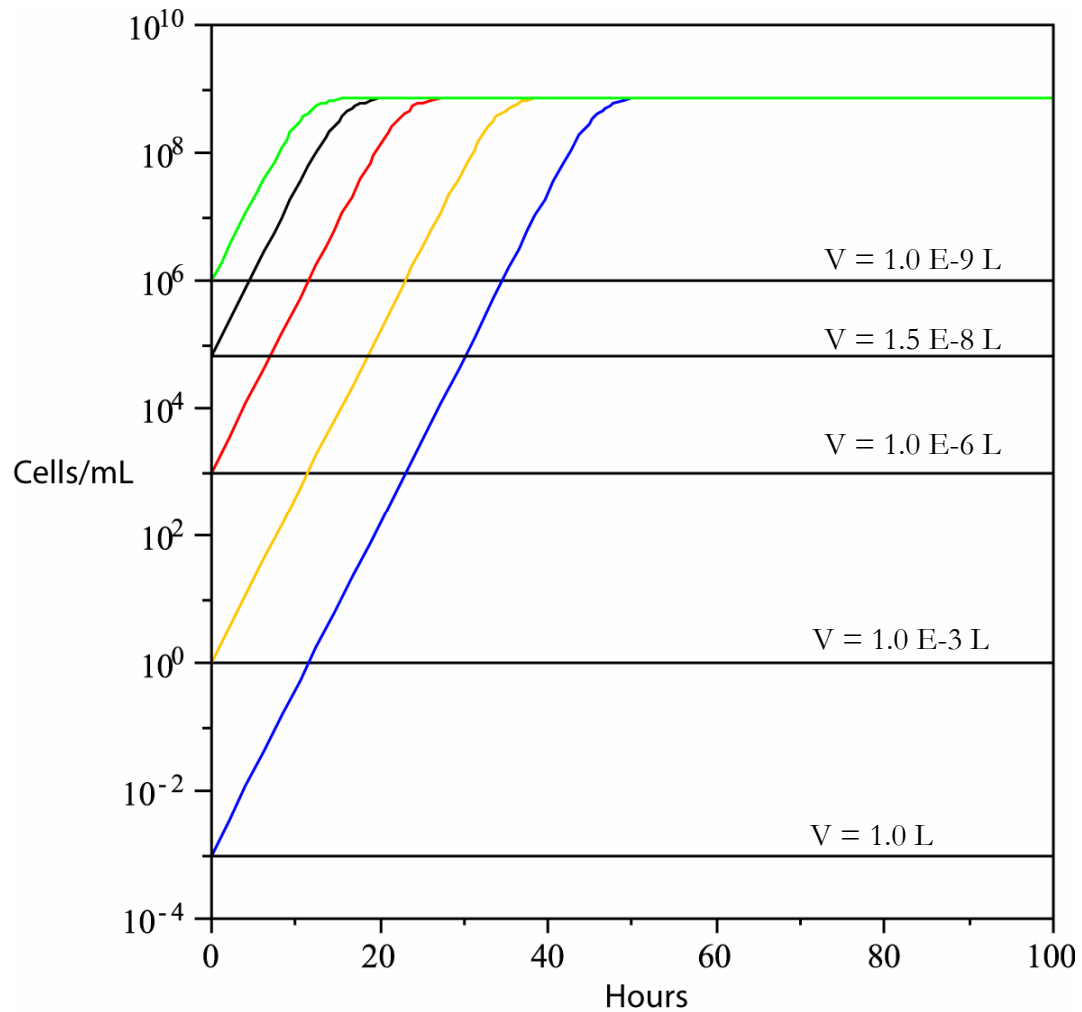


Figure 3.9. Chemostat growth ($\rho(t)$ Vs t) curves for various reactor volumes generated according to equation (2.23) under otherwise similar conditions ($n_0=1$, $\mu=0.8 \text{ hr}^{-1}$, $D=0.2 \text{ hr}^{-1}$, $N_\infty = 10^9 \text{ cells/mL}$).

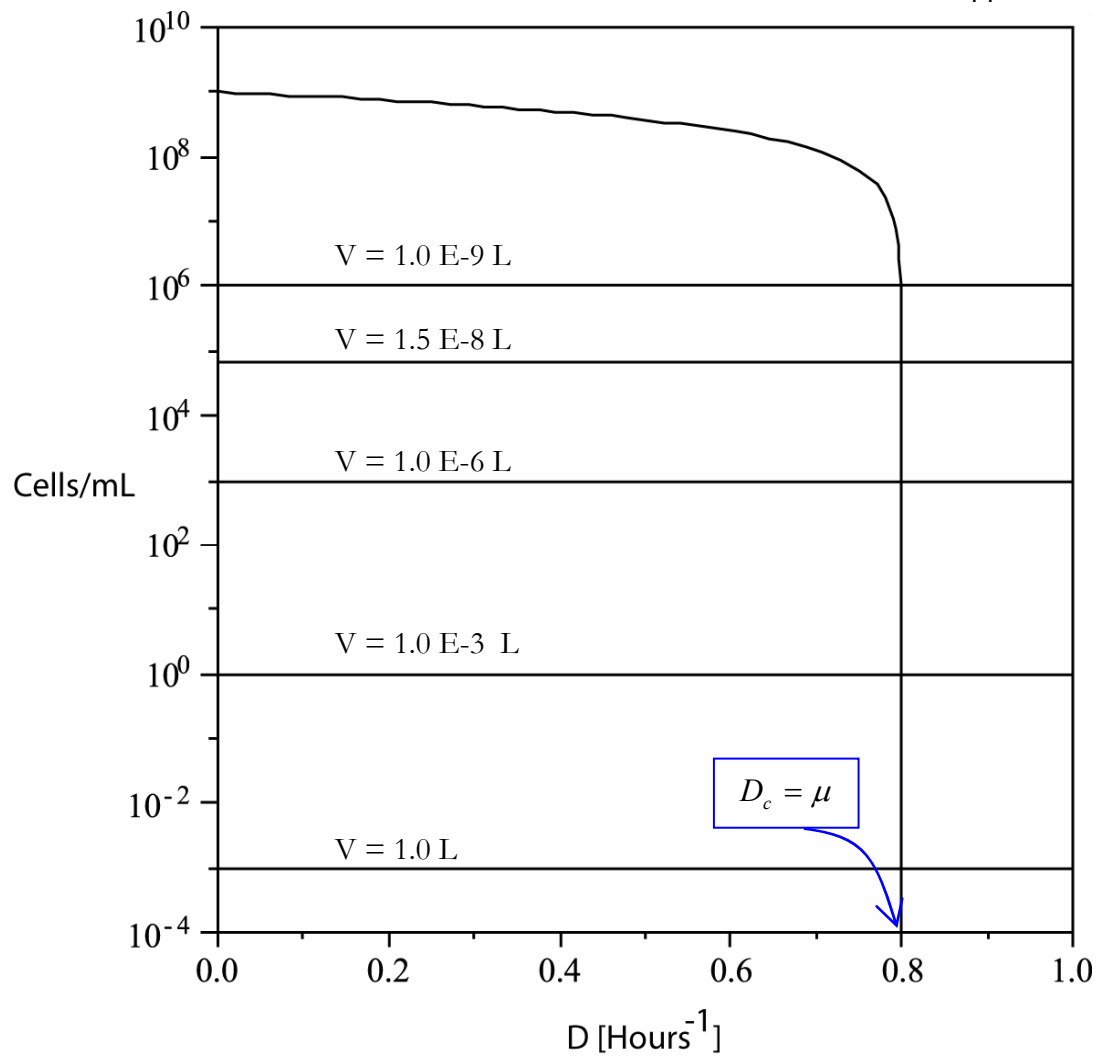


Figure 3.10. Steady state cell density (n_{ss}) as a function of the dilution rate for various reactor volumes generated according to equation (2.23) under otherwise similar conditions ($n_0 = 1$, $\mu = 0.8 \text{ hr}^{-1}$, $D = 0.2 \text{ hr}^{-1}$, and a carrying capacity of 10^9 cells/mL).

Moreover, substrate-limited growth in continuous culture is experimentally easier to realize when the population density is kept at a low value to fend off secondary effects such as partial growth limitation by oxygen or metabolic products(11, 14). However, the lower the nutrient concentration, the lower the attainable cell density, and unless the nutrient concentration is regulated with great accuracy, the cell density could fall below the minimum culturable density for a small reactor and the population would get washed out. For this reason, we used rich medium to characterize the microchemostat and adopted the “logistic growth model” (section 2.5.4) to characterize microchemostat growth.

As the dilution rate D is increased from 0 to $D_C = \mu$, the steady-state cell density n_{ss} decreases from ρ_∞ to 0 (equations (2.23) and (2.24)). Therefore, the smaller the reactor volume, the smaller the cell density at the point of wash-out (figure 3.10). The maximum dilution rate remains equal to D_C .

3.3.1 The Effect of Discontinuous Dilution

Chemostat operation described in chapter 2 is characterized by a continuous dilution rate; a relatively minuscule fraction of bacterial suspension is continuously substituted with fresh sterile medium. As a contrast to this paradigm, consider a situation where, for a given dilution rate, a bigger fraction of medium is exchanged at proportionately longer time intervals. The expression for the dilution rate ($D = w/V$) takes on the form:

$$D = \frac{F}{T}, \quad (3.2)$$

where T is the time interval between each dilution event, during which a fraction F of the culture is exchanged. The discretized mode of operation can be modeled as an initial value problem derived from the Logistic growth equation (2.21).

$$n_{x\Delta t} = n_{(x-1)\Delta t} + \Delta t \left[\frac{\Delta n}{\Delta t} \right]_{(x-1)\Delta t}, \quad (3.3)$$

$$\left[\frac{dn}{dt} \right]_{x\Delta t} = n_{x\Delta t} \mu \left(1 - \frac{n_{x\Delta t}}{N_\infty} \right) - D n_{x\Delta t} \beta(t) \quad (3.4)$$

together with a specified initial condition for n , n_0 . Here Δt is the discrete time increment of the simulation and x is the iteration count ($t/\Delta t$). I define $\beta(t)$ as a discrete unit function such that $\beta(t) = 1$ when $t/\Delta t$ is an integer, and zero otherwise. The function $\beta(t)$ could be represented as

$$\beta(t) = \left\| \left[\left(\frac{t}{T} - \left\lfloor \frac{t}{T} \right\rfloor - 1 \right) \right] \right\|, \quad (3.5)$$

where $\|h\|$, $\lfloor h \rfloor$, and $\lceil h \rceil$ represent the absolute value, floor and ceiling of a real number h respectively. For any given dilution rate, in the limit as F approaches zero, T also approaches zero and the flow becomes continuous (equation (2.22)).

The behavior of a chemostat population undergoing continuous dilution is very similar to that which is operated via discretized dilutions (figure 3.11). Figure 3.14 shows the effect of the discontinuous dilution process on microchemostat cultures under steady-state conditions during an actual experiment. The cultures do maintain stable density and

the fluctuations due to discretized dilution are often below the noise in the measured cell density.

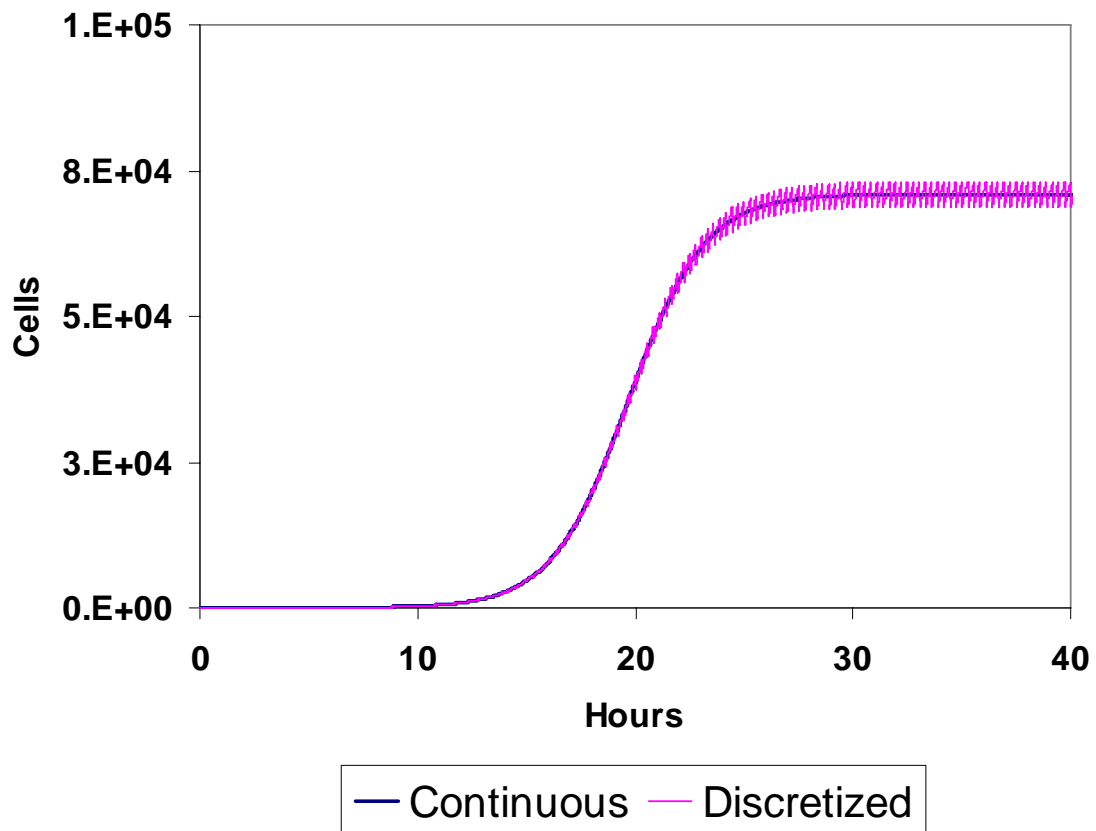


Figure 3.11. Theoretical graph of $n(t)$ with continuous and discretized dilution scheme for $\mu = 0.8 \text{ hr}^{-1}$, $D = 0.232 \text{ hr}^{-1}$, $N_\infty = 10^5$ cells, and $F = \frac{1}{16}$.

3.4 Results

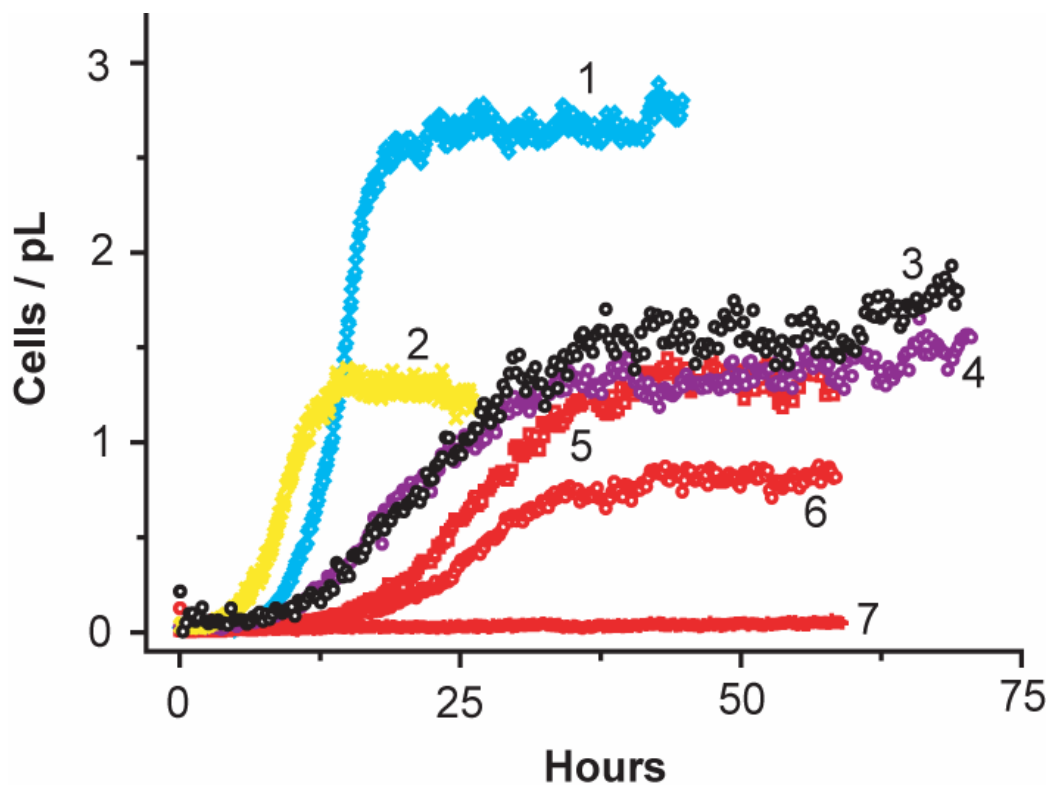


Figure 3.12. Growth curves as a function of time in various media and dilution rates (D). (1) MOPS EZ rich, 1.1 M glucose, $D = 0.34 \text{ hr}^{-1}$, $32 \text{ }^\circ\text{C}$. (2) MOPS EZ rich, 0.11 M glucose, $D = 0.30 \text{ hr}^{-1}$, $32 \text{ }^\circ\text{C}$. (3) LB, 0.5 g/L bacto-tryptone, $D = 0.24 \text{ hr}^{-1}$, $21 \text{ }^\circ\text{C}$. (4) LB, 0.5g/L bacto-tryptone, $D = 0.30 \text{ hr}^{-1}$, $21 \text{ }^\circ\text{C}$. (5) LB, 3g/L bacto-tryptone, $D = 0.37 \text{ hr}^{-1}$, $21 \text{ }^\circ\text{C}$. (6) LB, 0.5 g/L bacto-tryptone, $D = 0.37 \text{ hr}^{-1}$, $21 \text{ }^\circ\text{C}$. (7) LB, 0.1 g/L bacto-tryptone, $D = 0.37 \text{ hr}^{-1}$, $21 \text{ }^\circ\text{C}$. The red curves (5, 6, and 7) represent different concentrations of bacto-tryptone in LB at a fixed dilution rate whereas the empty circles (3, 4, and 6) depict constant influent nutrient composition at various dilution rates. Cultures 3, 4, 5, 6 and 7 were cultivated on a single chip whereas cultures 1 and 2 were each cultivated on separate chips.

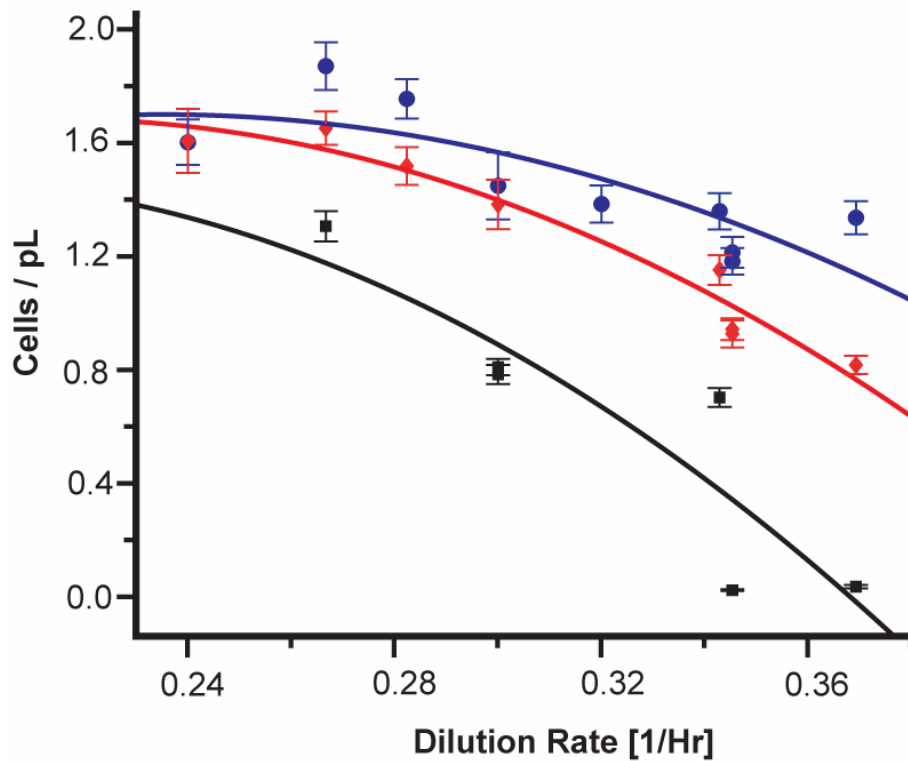


Figure 3.13. Graph showing steady state populations for various choices of dilution rate and nutrient concentrations at 21 °C. The error bars represent the variation in the measured steady-state cell density. The steady-state concentration decreases as the dilution rate increases, and increases in proportion to the influent nutrient “richness”. Black boxes = 0.1 g/L bacto-tryptone; Red diamonds = 0.5 g/L bacto-tryptone; Blue circles = 3 g/L bacto-tryptone.

To characterize the performance of the microchemostat we performed multiple microchemostat experiments using MG1655 cells in five different chips using a variety of growth media (MOPS EZ rich and LB broth with various concentrations of glucose and bacto-tryptone) at 21 °C and 32 °C. Upon inoculation, a typical culture began with a short lag period, followed by an exponential growth phase that gave way to a steady-state regime (figure 3.12). Steady-state growth was achieved over a range of dilution rates (0.072 - 0.37 hr⁻¹) as well as cell washout at high dilution rates. The steady-state concentrations scaled with dilution rate and nutrient supply, decreasing with increasing dilution rates or decreasing bacto-tryptone (growth limiting factor) concentration (figure 3.13).

It has been shown that changes in pH and oxygen levels affect microbial growth rates (48). To minimize the pH variation in microchemostat experiments, pH-buffered medium was used. Changes in oxygen concentration have been observed in other microfluidic bioreactors (48), and they may have contributed to the small variations in steady-state cell densities (figures 3.12). Nevertheless, we expect variations in oxygen levels to be minor in our device because of the high gas permeability of the PDMS, large surface area-to-volume ratio, and the continuous influx of fresh growth medium.

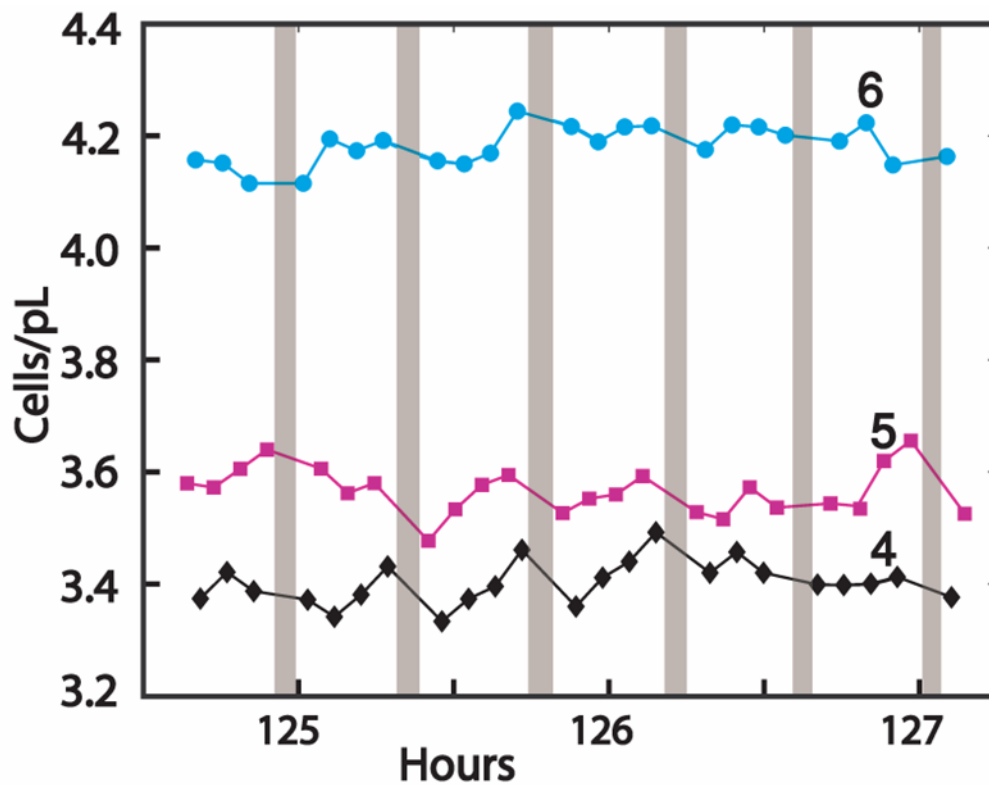


Figure 3.14. The effect of the discontinuous dilution process on strain MC4100Z1 microchemostat cultures under steady-state conditions during an actual experiment. The gray strips represent dilution intermissions.

In support of this notion, a recent study suggested that a reactor depth of $300\mu\text{m}$ (compared to a depth of $10\mu\text{m}$ of our device) would allow sufficient oxygenation to support 10^9 cells/mL (49). We routinely obtained cell densities up to 3×10^9 cells/mL, which strongly suggest oxygen was not limiting growth. Figure 3.14 illustrates the effect of the discontinuous dilution scheme on the steady-state cell densities of typical

microchemostat cultures. The cultures do exhibit stable density and the fluctuations due to discretized dilution are often below the noise in the measured cell density.

Fits to the equation $(n(t) = n_0 e^{(\mu-D)})$ during exponential rise, when the cell density is still low and before growth factors begin to limit growth, can be used to extract the growth constant during the exponential phase μ_{Rise} . Therefore, the value for the intrinsic growth rate $\mu_{Intrinsic}$ can be obtained from equation (3.6) (figure 3.15).

$$\mu_{Intrinsic} = \mu_{Rise} + D \quad (3.6)$$

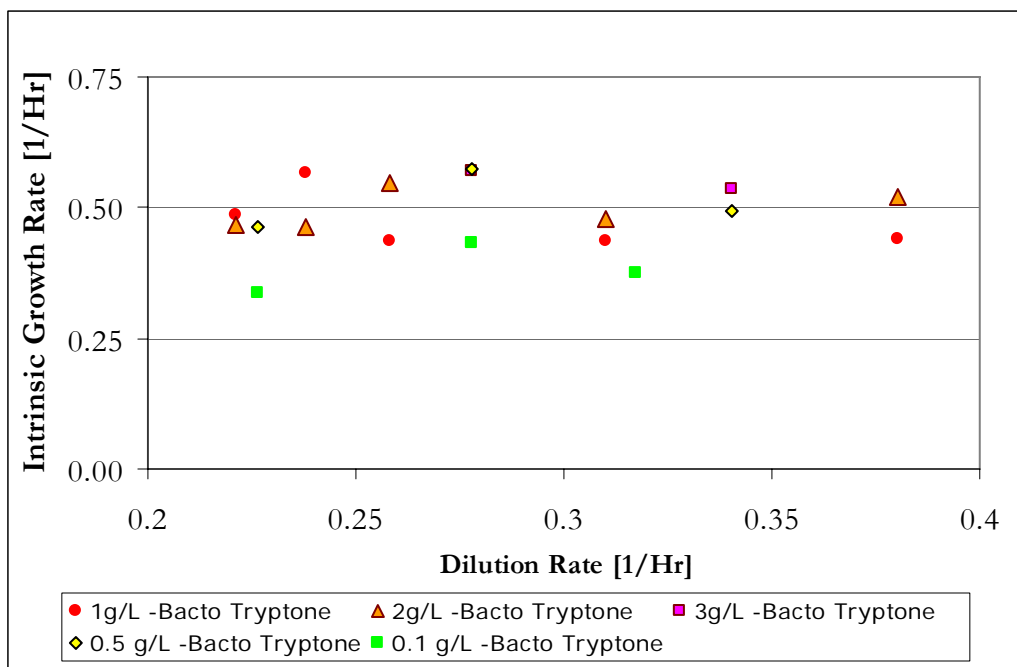


Figure 3.15. Typical values of the intrinsic growth rate at 21 °C for strain MG1655. The growth rate at 21 °C hovers around 0.5 hr⁻¹ and is independent of the dilution rate, as expected. To ascertain the legitimacy of using the “logistic growth model” (section

2.5.4) to describe microbial growth in the microchemostat, we fit the experimental microchemostat growth curves obtained to equation (2.23) (figure 3.16):

$$n(t) = \frac{n_0 N_\infty (\mu - D)}{n_0 \mu + (N_\infty \mu - n_0 \mu - N_\infty D) e^{-(\mu - D)t}}.$$

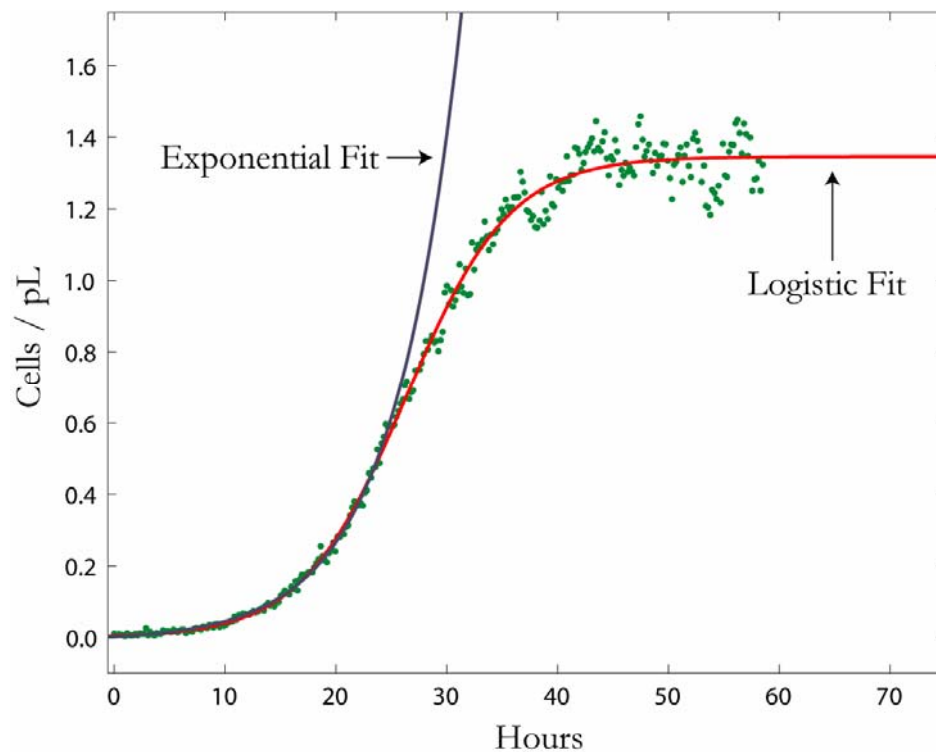


Figure 3.16. Typical microchemostat growth curve showing fits to logistic and exponential equations.

For each fit, we specify the dilution rate D , the only control parameter in the experiments, which has no bearing on the intrinsic growth rate (other control parameters include; temperature, nutrient composition, and the microbial strain) and extract the specific growth rate $\mu_{Logistic}$, the medium carrying capacity N_{∞} for each given nutrient composition. Table 3.1 shows a sample of the intrinsic growth rates obtained from both fits for typical cultures.

Table 3.1. Values for the intrinsic growth rate obtained from fits to the logistic and the exponential equations.

$\mu_{Logistic}$	$\mu_{Exponential}$
0.49	0.55
0.58	0.54
0.58	0.54
0.63	0.58

3.5 The Future of Microreactor Design

The critical mission of future micro-reactor designs will remain focused on the optimization of chip real estate, increase of throughput and, simultaneously, reduction in the amount of reagents used. An example of this notion is illustrated in figures 3.17 and 3.18, in which the circular symmetry is exploited to increase the number of reactors that occupy the same amount of chip space. Whereas each module is comprised of a lot more reactors in comparison to the designs that came before, it consumes an equal amount of substrate.

Above all thanks to its ability to slow down microbial evolution, the microchemostat could find itself integrated as an ingredient of a multi-component monolithic entity. The microchemostat would mainly be responsible for *in situ* culturing and supply of genetically homogeneous bacteria that would be used in various capacities. For example, a device in which a microchemostat would culture bacteria and periodically avail a fraction of them for chemotaxis measurements has already been envisioned (chapter 6, unpublished data).

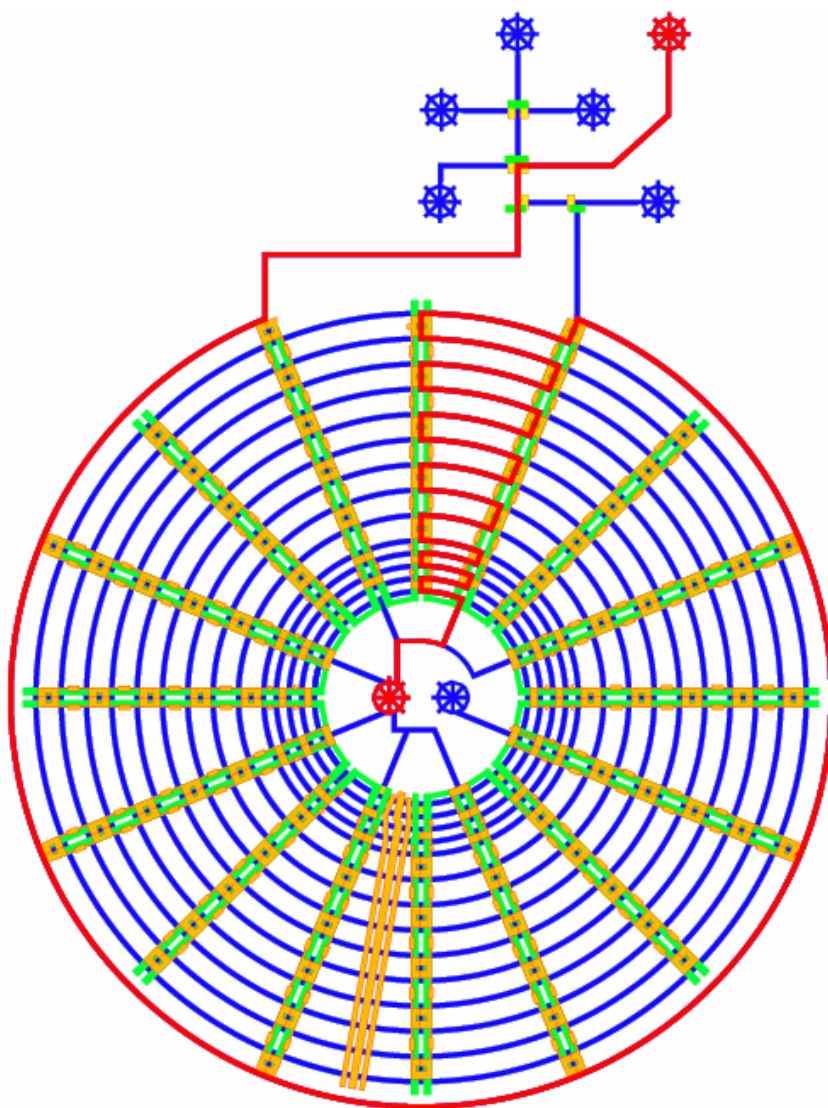


Figure 3.17. Microchemostat schematic illustrating a concentric reactor design paradigm that would optimize chip real estate and increase throughput. The reactors are represented by the blue concentric circles. Simultaneous isolation of reactor segments to perform a dilution (indicated in red). The control lines are illustrated in green and orange.

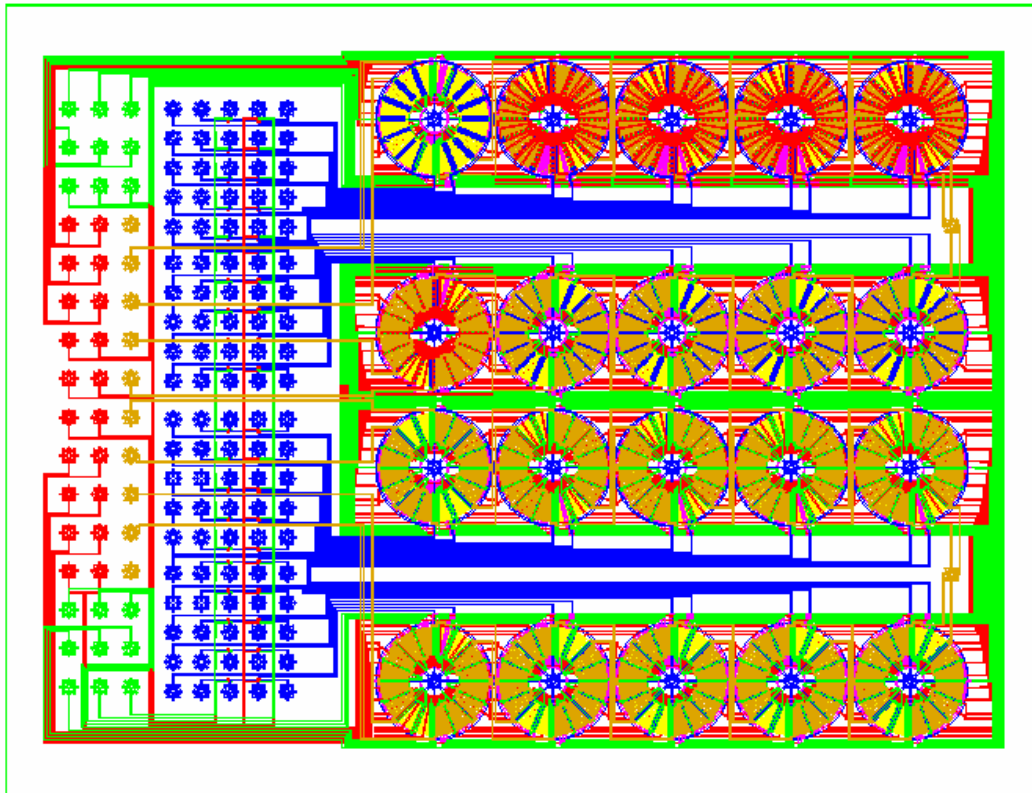


Figure 3.18. Schematic of a chip design that would exploit concentric reactor paradigm to implement 240 reactors on a single chip. Each of the 20 circular discs contains 12 concentric reactors.

Chapter 4

Quorum Sensing and Population

Control

4.1 Introduction

4.1.1 Synthetic Biology and the Microchemostat

Synthetic biology (7-9, 50) is the engineering of genetic elements or the integration of basic elements into biological circuits to implement more complex behavior. It involves the creation of biological systems for investigation of natural biological phenomena and for a variety of utilitarian purposes ranging from generation of novel proteins (such as new catalysts for synthetic chemistry reactions) to environmental waste remediation and highly specific enzymes for gene therapy or pathogen destruction (51). Synthetic networks have recently facilitated the creation of organisms endowed with sophisticated non-native behaviors such as programmed population control (6, 52) and pattern formation (53), synthetic eco-systems (54), oscillations (6, 55), proteins customized for biosensing, and optimized drug synthesis

(56). Nevertheless, the field is still in its infancy, wielding immense potential for scientific innovation, invention, funding, and commercialization.

The science of engineering biological circuits that program non-native behavior is extremely complex:

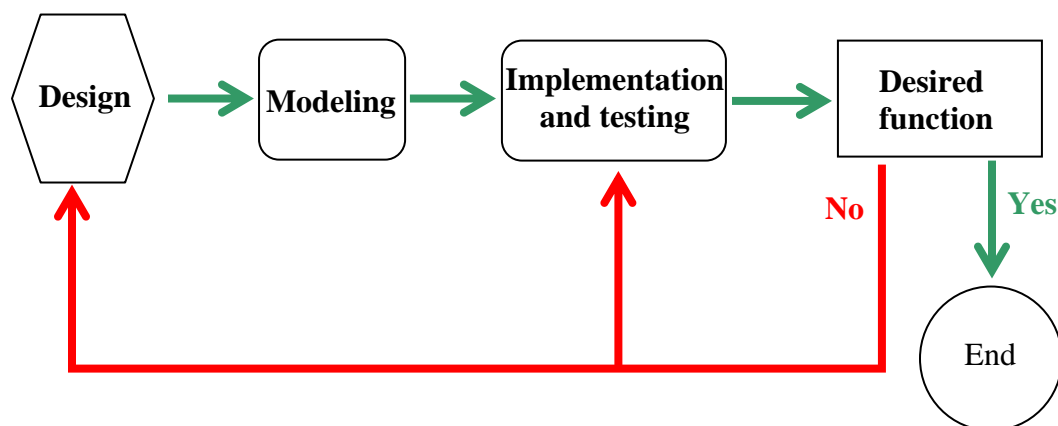


Figure 4.1. The typical process for engineering genetic circuits (modified from reference (57)).

The genetic engineering process usually involves multiple cycles of design, optimization and revision (figure 4.1). As the number of interacting parts and reactions increases, it becomes more and more difficult to intuitively predict gene circuit behavior. This has made computers models a useful design tool (58). Although the computers can generate multiple promising candidate constructs (51), they are not sufficiently advanced

to accurately predict the precise function of each newly designed biological device. Moreover such models are usually simplified out of necessity to capture only the qualitative behavior of the underlying systems due to limited quantitative characterization of circuit elements and may fail to capture richer dynamics intrinsic to a circuit. Consequently, the most practical way to implement the desired functional behavior may require one to operate and observe the dynamics of multiple candidate constructs (57).

Most of the current methods of circuit characterization employ conventional techniques such as fluorescence-activated cell sorting, counting colony forming units on petri-plates, optical density measurements, and fluorescence measurements of culture samples and colonies. Whereas these approaches yield useful and reliable information, they tend to be invasive, generally expensive, arduous, time consuming, hands-on (prone to human error) and may require large amounts of sacrificial culture.

The evolvability of genetic code may also render the programmed circuits unreliable and unpredictable by effecting premature loss of programmed function. This often happens especially when there is strong selection pressure for the programmed microbes to evade circuit function (6). It therefore becomes difficult to project or characterize long-term circuit behavior, which information may be prerequisite before the circuit can be deployed.

The microchemostat presents itself as a high throughput screening technology that could inexpensively perform rapid characterization of synthetic circuits under a matrix of conditions with unprecedented capabilities: long-term, non-invasive

measurements of microbial population properties under steady-state conditions with single cell resolving power and advanced automation. Equally important, the microchemostat's miniaturized working volume of ~ 10 nL is capable of culturing extremely small populations of bacteria ($\sim 10^2$ to $\sim 10^4$ cells versus at least $\sim 10^9$ in macroscale cultures). The microsized population reduces the number of cell-division events per unit time and hence slows down microbial evolution (10). This aspect facilitates monitoring of programmed behavior of bacterial populations for hundreds of hours despite strong selection pressure to evade population control, something that may not be achieved in macroscopic reactors (6).

4.1.2 Quorum Sensing in Bacteria

Bacteria were for a long time believed to exist as individual cells that sought primarily to find nutrients and multiply. The discovery of intercellular communication or “quorum sensing (59, 60)” among bacteria led to the realization that bacterial populations are capable of high-level coordinated behavior that was once believed to be restricted to multicellular organisms (61).

The capacity to behave collectively as a group (or population) endows bacteria with capabilities that can not be achieved in solitude. For instance, the most intensely studied quorum sensing system allows the bioluminescent marine bacterium, *Vibrio fischeri*, to harmoniously live in symbiotic association with a number of eukaryotic hosts. In each case, the host has developed a specialized light organ that is inhabited by a pure

culture of *V. fischeri* at very high cell density. In these symbiotic associations, the eukaryotic host supplies *V. fischeri* with a nutrient rich environment in which to live, while *V. fischeri* provides the host with light. Each eukaryotic host uses the light provided by the bacteria for a specific purpose. For example in the squid *Euprymna scolopes*—*V. fischeri* association, the squid has evolved an antipredation strategy in which it counter-illuminates itself using light from *V. fischeri*. Counter illumination enables the squid to avoid casting a shadow beneath it on bright clear nights when the light from the moon and stars penetrates sea water. In contrast, the fish *Monocentris japonicus* uses the light produced by *V. fischeri* to attract a mate (60). Quorum sensing relationships are not always as amicable as the ones characterized by symbiotic bacteria. On the contrary, they can take on an adversarial role, as seen with pathogenic bacteria. For example, virulent bacteria like *Pseudomonas aeruginosa* use quorum sensing to sustain their pathogenic lifestyle. Evading host defenses is a major goal of pathogens, and as such, quorum sensing is an important asset because it enables bacteria to appropriately time expression of immune-response activating products. Using quorum sensing, bacteria can innocuously grow within a host without expressing virulence determinants. Once they amass a high cell density, they become aggressive; their numbers sufficient to produce ample virulence factors to overwhelm the host defenses, launch a successful infection and form an antibiotic-resistant biofilm, leading to disease (61, 62).

Quorum sensing works by allowing bacteria to communicate and regulate their gene expression in response to fluctuations in cell-population density (60). In the past decade, quorum sensing circuits have been identified in over 25 bacterial species. In

most cases, the quorum sensing circuits identified resemble the canonical quorum sensing circuit of the symbiotic bacterium, *Vibrio fischeri* in the above example. Specifically, quorum sensing circuits contain, at a minimum, homologues of two *Vibrio fischeri* proteins called LuxI and LuxR. The LuxI-like (or 'I') proteins are responsible for the biosynthesis of a chemical signaling molecule called acyl-homoserine lactones (AHL), which is small enough to freely diffuse across the cell membrane (60, 63) into the surrounding medium and back into the cell. Accordingly, the intracellular (and extracellular) AHL concentration changes as a function of the cell density. When the AHL concentration achieves a critical threshold concentration, it becomes bound to its cognate 'R' protein (64), to form an 'R'-AHL complex, which can activate target gene expression (65-67). When only a few other bacteria of the same kind are in the vicinity, diffusion reduces the concentration of AHL in the surrounding medium to almost zero. For this reason, there is a low likelihood for a bacterium to detect its own secreted AHL. With many bacteria of the same kind, however, the concentration of AHL can reach (or exceed) the required threshold, whereupon 'R' receptor becomes activated to initiate transcription of specific genes, such as luciferase in *V. fischeri*. Using such quorum sensing mechanisms, bacteria can efficiently couple gene expression to fluctuations in cell population density.

In the natural environment, there are many different bacterial species living together, communicating via a variety of LuxI/LuxR-type circuits with their respective signaling molecules or "languages". For example the LuxI/LuxR bioluminescence system in *Vibrio fischeri*, the LasI/LasR-Rh1I/Rh1R virulence system in *Pseudomonas*

aeruginosa, the TraI/TraR virulence system in *Agrobacterium tumefaciens*, and the ExpI/ExpR-CarI/CarR virulence/antibiotic system in *Erwinia carotovora* (60). There is evidence that interspecies communication via quorum sensing or quorum sensing cross talk can occur (68, 69). Nevertheless, the languages themselves are generally mutually exclusive and, therefore, as one species employs a specific language, it does not necessarily talk to all other species.

Because many important animal and plant pathogens use quorum sensing to regulate virulence, strategies designed to interfere with these signaling systems will likely have broad applicability for biological control of disease-causing organisms (69). For example, the discovery that *P. aeruginosa* uses quorum sensing to regulate biofilm production suggests that agents capable of blocking quorum sensing may also be useful for preventing biofilm formation. The recent production of AHLs in plants represents an exciting new approach to controlling crop diseases as well as to manipulating plant-microbe interactions for improved crop production in the future (61).

The principle of quorum sensing can also be used in synthetic biology programs to control the dynamics of an entire population despite variability in the behavior of individual cells. In this chapter, we used the microchemostat to characterize a synthetic population control circuit (5), programmed to autonomously regulate the cell density of an *Escherichia coli* population using quorum sensing.

4.2 The Population Control Circuit

The “population control” circuit (5) is a synthetic program engineered by our collaborators, Ligchong You and Frances Arnold, to autonomously regulate the cell density using a quorum-sensing-based (60) negative feedback system.

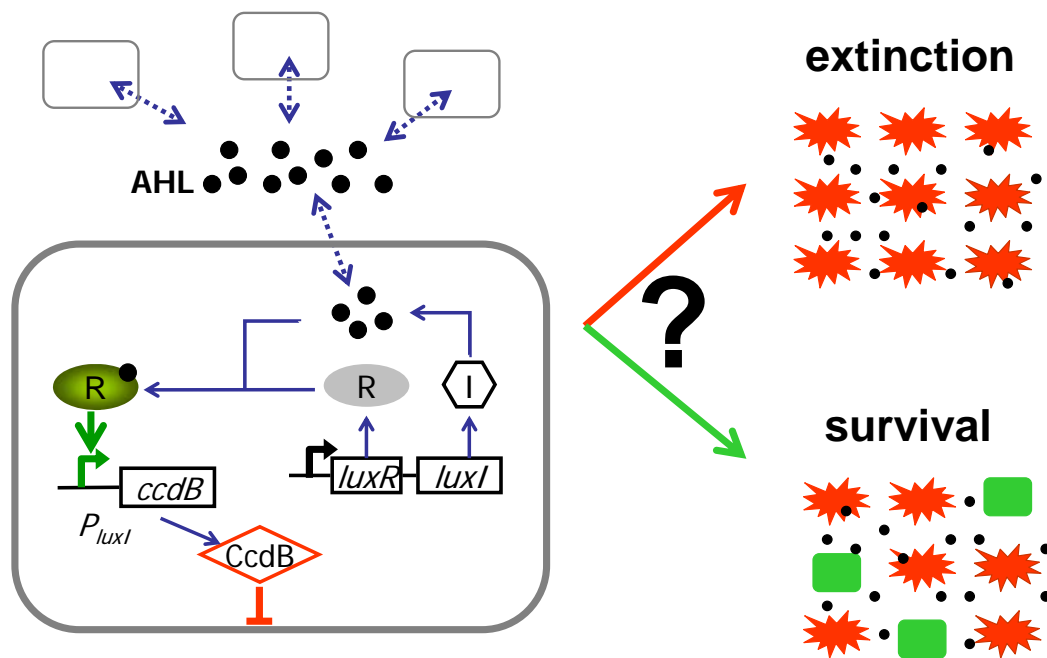


Figure 4.2. Schematic diagram for a population-control circuit, which programs population dynamics by broadcasting, sensing and regulating the cell density using cell–cell communication and negative feedback. Filled circles represent AHL.

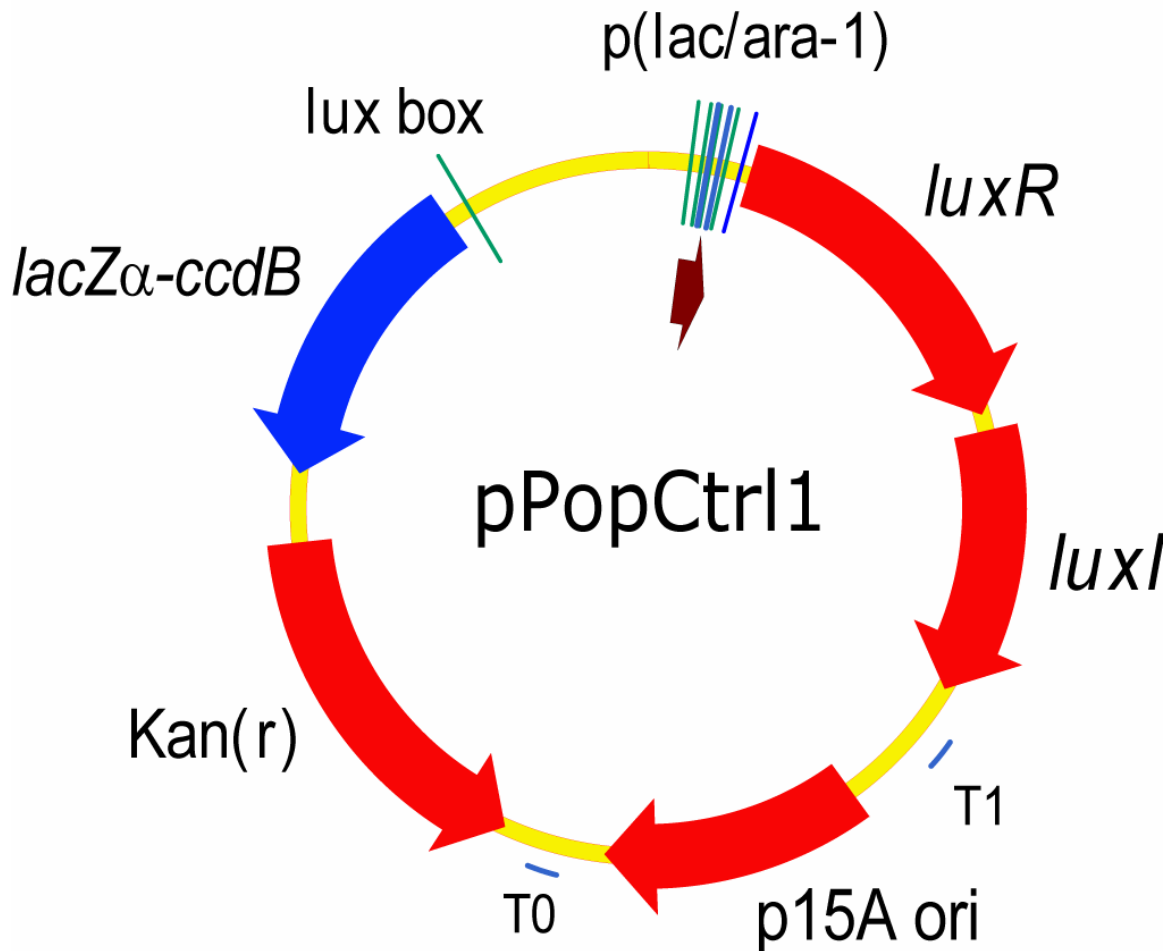


Figure 4.3. Implementation of the population control circuit (pPopCtrl1) by Lingchong You. The plasmid (p15A origin, kanamycin) was verified by sequencing. It was constructed by inserting PCR-amplified p_{luxI} -*lacZα-ccdB* (where *lacZα-ccdB* is the killer gene) from *p_{lux}CcdB3* (70) into plasmid pLuxRI between the AatII site. Plasmid pLuxRI was constructed by inserting PCR-amplified *luxI* from pSND-1 (71) into pLuxR, downstream of *luxR* (72). Note that the circuit is under control of a synthetic promoter $p_{lac/ara-1}$ (73), and is inducible with IPTG.

Specifically, the population control circuit (figure 4.2), programs a bacterial population to maintain a cell density that is lower than the limits imposed by the environment (for example, by nutrient supply). The LuxI protein of the well-characterized LuxI/LuxR system from the marine bacterium *Vibrio fischeri* (60), synthesizes the signaling molecule, AHL. At sufficiently high cell density (or high AHL concentration), AHL binds and activates the LuxR transcription regulator, which in turn induces expression of a killer gene (*lacZa-cdB*) under the control of a luxI promoter (p_{luxI}) (74). Sufficiently high levels of the killer protein cause cell death. The circuit was implemented on a plasmid (figure 4.3), where p_{LuxRI2} expresses LuxI and LuxR upon induction by isopropyl-b-D-thiogalactopyranoside (IPTG), and $p_{luxCdB3}$ responds to activated LuxR (at sufficiently high cell density) and causes cell death.

4.3 Results and Discussion

4.3.1 Population Control in the Microchemostat

We performed six population control circuit experiments simultaneously on a single microchemostat chip using *E. coli* MC4100Z1 cells and a dilution rate of 0.16 hr^{-1} (figure 4.4). Cultures in reactors 1-3 with circuit-bearing cells were induced with IPTG (circuit ON), while those in 5 and 6 were not induced (circuit OFF). Reactor 4 contained a circuit-free population with IPTG. Circuit-free and circuit OFF cultures (4, 5 and 6) grew exponentially to a steady-state density of $\sim 3.5 \text{ cells/pL}$. In contrast, circuit ON

populations (1, 2 and 3) exhibited oscillatory dynamics before reaching a lower steady-state population density after ~ 125 hr.

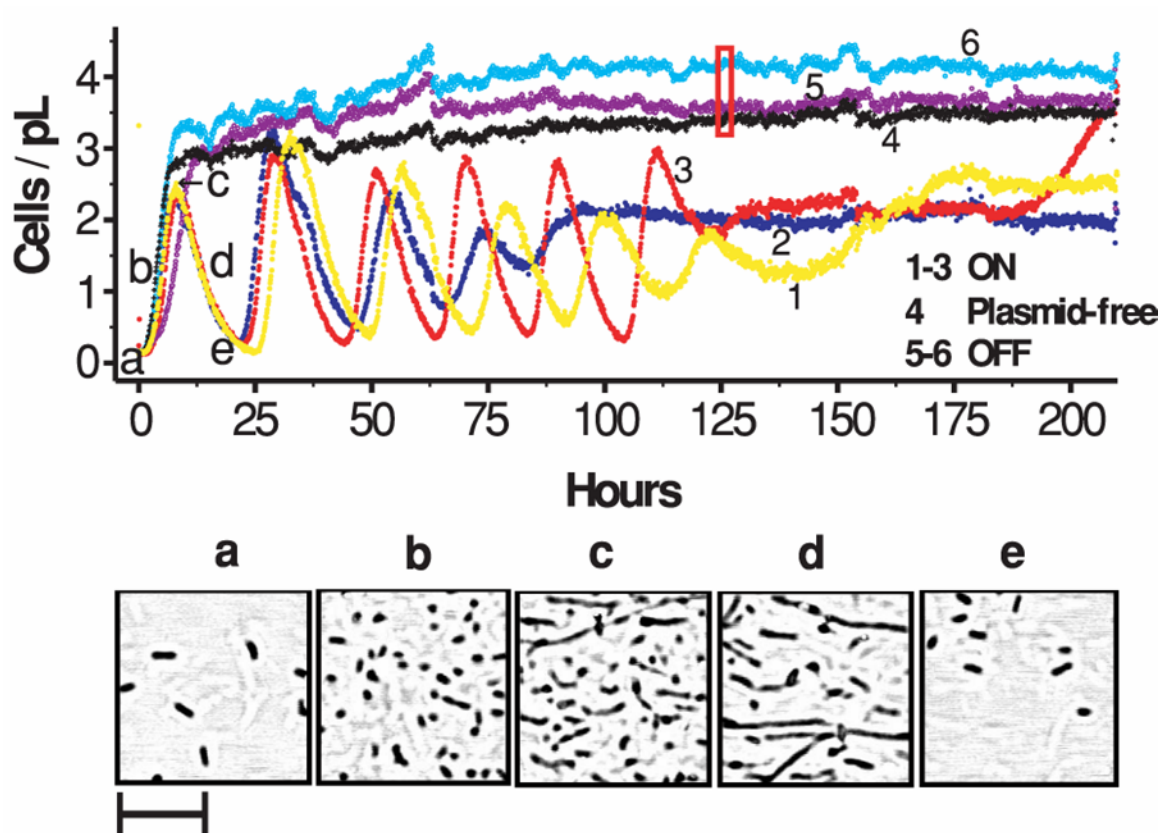


Figure 4.4. Growth of MC4100Z1 cells with the population control circuit ON (reactors 1-3), OFF (reactors 5-6), or absent (reactor 4) on a single chip. Bottom panels (a–e) show micrographs of the culture in reactor 3 at the corresponding points during the first oscillation (scale bar is $25 \mu\text{m}$). Cells were grown at $32 \text{ }^\circ\text{C}$ in LBK medium (see methods) buffered at pH 7.6 at a dilution rate of 0.16 hr^{-1} .

Using the ability to monitor the microchemostat with single cell resolution, we observed that the oscillations in cell density correlate with specific cell morphologies (figure 4.4). For example, upon inoculation, culture 3 (point *a*) was comprised of healthy (small and cylindrical) cells. With negligible expression of the killer protein (LacZ-CcdB) at such low density, the population initially enjoyed exponential growth, in tandem with the OFF cultures. The cells were generally healthy during this phase, evident in their morphology (point *b*). However, as the increased cell density led to increased AHL concentration and, consequently, increased expression of the killer protein (point *c*), the cell density began to decrease. By this time, a fraction of cells had become filamented, indicative of the deleterious effect of LacZ α -CcdB. Due to a lag in the turnover of the signal (by dilution and degradation) and that of the killer protein (by cell division and degradation), cell death intensified (point *d*), leading to a sharp decrease in the cell density. Further decreases in cell density ultimately led to a decrease in the signal concentration as well as the killer protein concentration. Eventually, when the death rate dropped below the growth rate (when the killer protein had been diluted out, at point *e*), the population recovered and entered the next cycle. Cultures 1 and 2 demonstrated similar dynamics. Culture 3 escaped circuit regulation after 186 hours. Under these conditions, the circuit drove 4-6 oscillations before approaching a steady-state concentration of ~ 2 cells/ μ L.

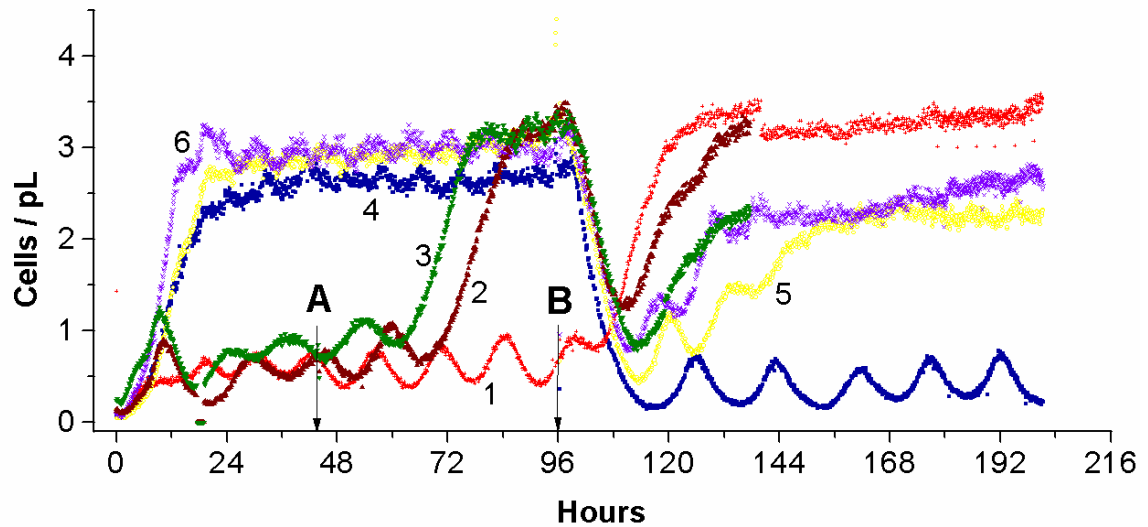


Figure 4.5. Growth of Top10F' cells with the circuit ON or OFF in the chip (ON-OFF cycles). Initially, cultures 1, 2, and 3 were ON while cultures 4, 5 and 6 were OFF. At 44 hours (point A), cultures 2 and 3 were turned OFF. At 96 hr (point B), culture 1 was turned OFF, while cultures 2-6 were turned ON. Cultures 2 and 3 were cultivated on a separate chip in a different experiment under the same conditions. When turned OFF, culture 1 (at 96 hr) and cultures 2 and 3 (at 44 hr) grew exponentially to a density of ~ 3 cells/pL. Upon circuit activation at 96 hr after an extended OFF period, culture 4 generated sustained oscillations similar to those of culture 1 between 0 and 96 hr, following a rapid decrease in cell density. In comparison, when switched ON at 96 hr, cultures 2, 3, 5 and 6 only briefly demonstrated circuit regulation (evident in the sharp decrease in cell density) before bouncing back to a high density.

When the population control circuit was transformed into a different *E. Coli* host strain, different circuit dynamics became apparent. In the *E. coli* Top10F' strain, more

complete induction of the circuit was achieved, leading to stronger growth regulation (figure 4.5). In these experiments (dilution rate = 0.16 hr^{-1}), at time zero the circuit was turned ON in cultures 1-3 but left OFF in cultures 4-6. The OFF cultures (4 – 6, 0 – 96 hr) grew to a steady-state density of $\sim 3 \text{ cells/pL}$. In contrast, the density of the ON cultures (1, 0 – 96 hr; 2 and 3, 0 – 44 hr) oscillated about $\sim 0.5 \text{ cells/pL}$, 6-fold lower than the average circuit OFF density. Since the total cell count reading included both live and dead cells, the actual circuit ON viable cell density is even lower.

Unlike MC4100Z1 cells, Top10F' cells revealed no observable morphological responses to circuit regulation: they always looked small and cylindrical, similar to circuit OFF cells. When turned OFF, culture 1 (at 96 hr) and cultures 2 and 3 (at 44 hr) grew exponentially to a density of $\sim 3 \text{ cells/pL}$. Upon circuit activation at 96 hr after an extended OFF period, culture 4 generated sustained oscillations similar to those of culture 1 between 0 and 96 hr, following a rapid decrease in cell density. In comparison, when switched ON at 96 hr, cultures 2, 3, 5 and 6 only briefly demonstrated circuit regulation (evident in the sharp decrease in cell density) before bouncing back to a high density.

In general, we found that the circuit was genetically much more stable in the microchemostats than in macro-scale batch cultures under otherwise similar growth conditions. During the macro-scale experiments with reaction volumes of 3-50 mL, mutants which escaped circuit regulation took over the population within 40 and 150

hours for MC4100Z1 and Top10F', respectively (75). The microchemostat, in contrast, maintains very small populations ($\sim 10^2$ to $\sim 10^4$ cells versus $\sim 10^9$ cells in macro-scale cultures) over 250-500 hours, a 5-fold improvement.

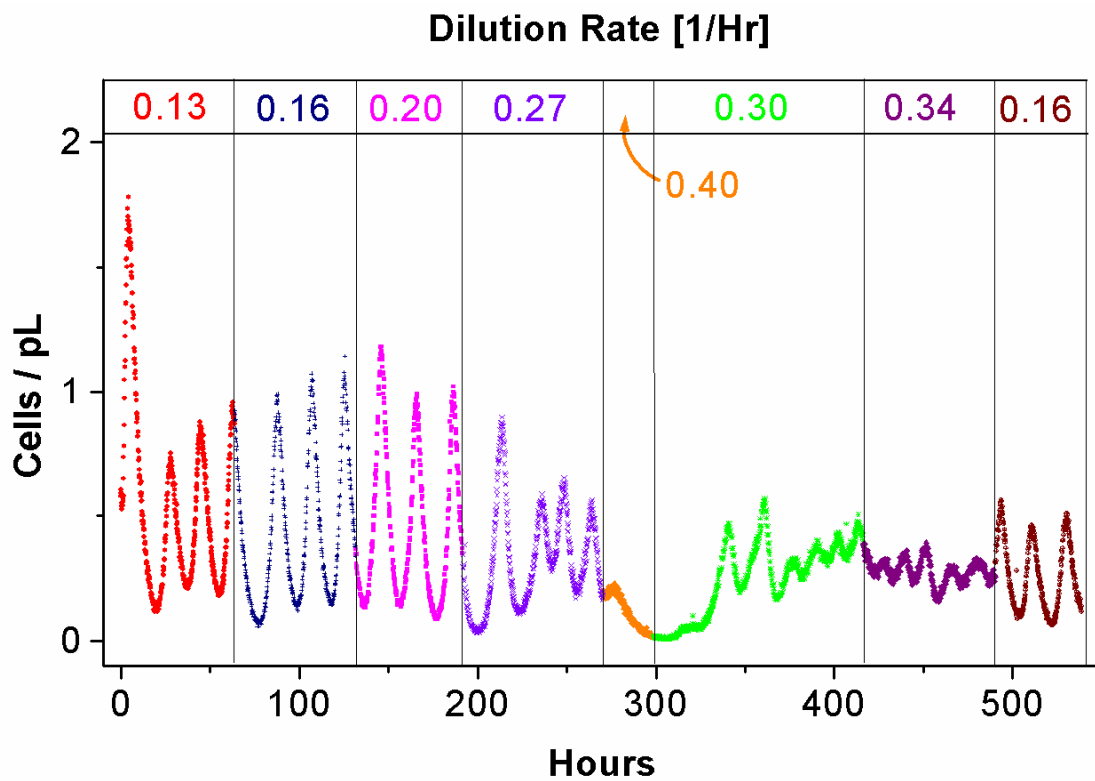


Figure 4.6. Effects of the dilution rate on population dynamics of Top10F' cell with population control circuit ON. At high dilution rates, both the amplitude and the period of oscillations diminished (0.27 , 0.30 , and 0.34hr^{-1}). The culture was approaching washout at the highest dilution rate (0.40 hr^{-1}). Large oscillations were recovered when a low dilution rate was restored toward the end of the experiment.

Figure 4.6 shows the best result to date: continuous circuit-ON behavior for more than 500 hours. The amount of variation in fitness an organism maintains increases as the logarithm of the population size and the mutation rate, which leads to a similar logarithmic increase in the speed of evolution (10). Therefore, in a microchemostat, the likelihood of occurrence for mutants that escape synthetic circuit regulation is much lower. Evidently, circuits can maintain control for significantly longer periods in the microchemostat than in the macro-scale experiments.

4.3.2 Modeling Population Control in the Microchemostat

With this circuit, the population dynamics—that is, its increase or decrease—is coupled to intracellular gene expression. The circuit acts as a negative feedback with the signaling molecule as the sole communication link.

A model developed by Lingchong You can be used to explain the observed circuit dynamics:

$$\frac{dN}{dt} = N \left(\mu - D - \frac{\mu N}{N_\infty} \right) - dEN, \quad (4.1)$$

$$\frac{dE}{dt} = k_E R - d_E E, \quad (4.2)$$

$$\frac{dR}{dt} = k_R A - d_R R, \quad (4.3)$$

$$\frac{dA}{dt} = v_A N - (d_A + D)A, \quad (4.4)$$

$$D = \frac{F}{T}, \quad (4.5)$$

where R represents the concentration of the dimerized, activated LuxR, k_R and d_R are the production and degradation rate constants of R , D is the dilution rate of microchemostat operation (equation (4.5)). T is the time interval between each dilution event, during which a fraction F of the culture is exchanged. Other variables and parameters are described previously (5). The only revision from previous version is the introduction of an intermediate reaction step: activation of LuxR, which accounts for the binding of the signal to the inactive LuxR, and dimerization of the active LuxR. Batch culture dynamics would correspond to the case where $D = 0$. If production and degradation of active LuxR are much faster than other reactions, the above model can be reduced to its previous form.

When $N \ll N_\infty$, equation (4.1) reduces to $\frac{dN}{dt} = (\mu - D - dE)N$. Then the simplified model will have two steady-state solutions: $(N_{SS} = 0, E_{SS} = 0, R_{SS} = 0, A_{SS} = 0)$ and $(N_{SS} = \frac{d_A d_E d_R \mu}{v_A k_E k_R d}, E_{SS} = \frac{\mu}{d}, R_{SS} = \frac{d_E \mu}{k_E d}, A_{SS} = \frac{d_E d_R \mu}{k_E k_R d})$. Based on linear stability analysis, the trivial steady-state is always unstable. The non-trivial steady state is stable for:

$$\begin{aligned}
& (d_A + D)d_E d_R + ((d_A + D) + d_E + d_R)^2 (\mu - D) \\
& < ((d_A + D) + d_E + d_R)(d_E d_R + (d_A + D)(d_E + d_R))
\end{aligned} \tag{4.6}$$

From this inequality, we expect the systems to oscillate when degradation rates of LuxR, the killer protein, and the AHL signal, and the microchemostat dilution rates are all small enough. Increase in any of these parameters turn to stabilize the non-trivial steady state and diminish oscillation (e.g., figure 4.7). The model could be further expanded to account for accumulation and washing out of dead cells in the reactor. Numerical simulations indicate that the total cell density will only oscillate if the viable cell density oscillates.

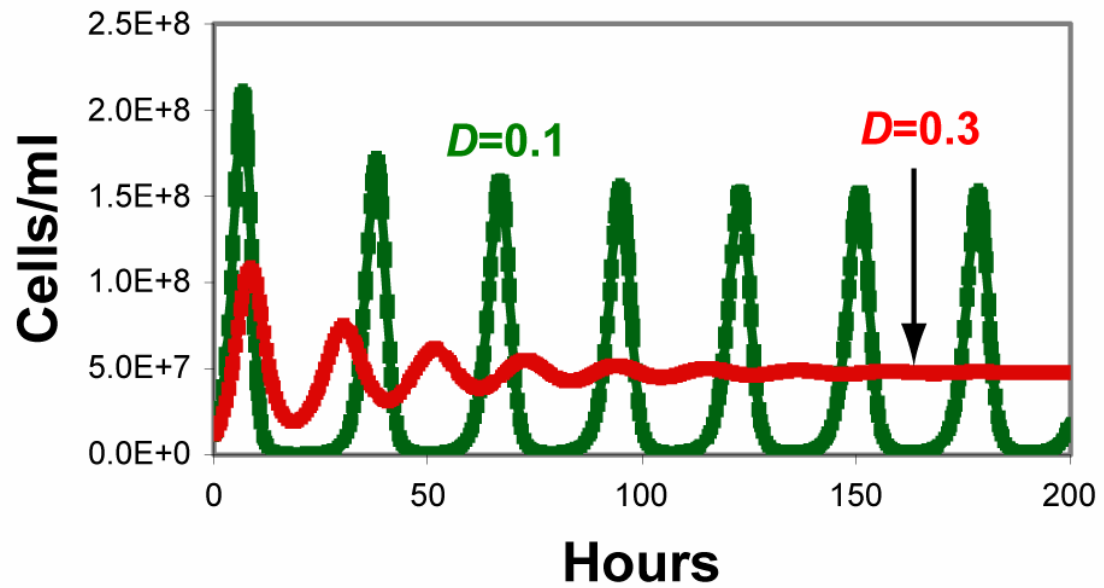


Figure 4.7. Typical simulation results for the population control dynamics inside the microchemostat. Initial conditions and parameter values are given in Tables S1 and S2 unless noted otherwise. The model generated sustained oscillations for small microchemostat dilution rate ($D = 0.1$), but damped oscillations when D is larger ($D = 0.3$). The numerical simulations were carried out using Dynetica (76).

4.4 Materials and Methods

Media, Strains, and Growth Conditions

Luria-Bertani (LB) medium contains 5g yeast extract, 10g tryptone and 10g NaCl per liter. LBK medium contains 10g tryptone, 5g yeast extract, and 7g KCl per liter, and 100mM 3-(N-morpholino) propanesulfonic acid (MOPS). MOPS EZ rich medium (TekNova, Half Moon Bay, CA) contains 100ml of 10X MOPS, 10ml of 0.132M K_2HPO_4 , and 100ml of 10X ACGU supplement and 580ml of 5X (amino acid) supplement EZ per liter. Medium pH (measured with Accumet pH Meter 925, Fischer Scientific) was adjusted by adding 5M KOH.

A revised version of the population control circuit (5) on a single plasmid (figure 4.3) was tested in MC4100Z1 cells (gift from Michael Elowitz) or 'Top10F' cells (Invitrogen). The MC4100Z1 strain was constructed by inserting a cassette containing *lacIq*, *tetR*, and *spect(R)* genes into the chromosome of the MC4100 strain (genotype: *araD139* Δ (*argF-lac*)205 *flb-5301* *pstF25* *rpsL150* *deoC1* *relA1*). We found that function of the single-plasmid version of the circuit was similar to that of the double-plasmid version. LB medium was used for cell growth to probe qualitative behavior and to prepare starter cultures for microchemostat experiments. To measure population control circuit dynamics, cells were grown in pH-buffered LBK medium. The population control circuit plasmid was maintained with 50 μ g/mL of kanamycin. When applicable, 1mM IPTG (unless otherwise stated) was used to activate the circuit. Under this condition, the circuit in MC4100Z1 is only *partially* induced due to the presence of the AraC repressor, which

binds to the araO sites in the synthetic promoter (73). However, we did not further induce the promoter using L-(+)-arabinose because it is toxic to the MC4100Z1 cells. 1mM IPTG can fully induce circuit function in 'Top10F' cells, because these cells do not produce AraC.

Precultures were prepared by inoculating a 2ml medium sample with cells from a single agar plate colony and shaking at 280 rpm for 6 hours at 37 °C. The precultures were then used to seed microchemostat reactors with ~20 cells/nL. All microchemostat media were supplemented with 5g per liter bovine serum albumin as an anti-adhesion adjuvant. During experiments, the microchemostat chip was placed on a warming stage system with a slotted opening (Brook Industries, Lake Villa, IL) to control growth temperature at an exterior temperature of 37 °C resulting interior (chip) temperature of ~32 °C. Chip temperatures were monitored using a tip-sensitive thermocouple and an i/32 Temperature monitoring system (Omega Engineering, Stamford, CT). The thermocouple was inserted into the chip through a vertical hole incorporated into the chip PDMS structure to the cover slip floor of the chip beside the microchemostat reactors.

4.5 Conclusion

Using a new approach to preventing biofilm formation, we implemented a microfluidic bioreactor that enables long-term culture and monitoring of extremely small populations of bacteria with single-cell resolution. We used this device to observe the dynamics of *Escherichia coli* carrying a synthetic “population control” circuit which autonomously regulates cell density using a quorum-sensing-based feedback mechanism. The microfluidic bioreactor enabled long-term monitoring of unnatural behavior programmed by the synthetic circuit including sustained oscillations in cell density and associated morphological changes over hundreds of hours.

Chapter 5

A Synthetic Predator-Prey Ecosystem

“You should actively engage your cat at least a couple of times a day with some predator-prey activity, such as chasing foil balls or chasing a feather lure on a stringed pole, to avoid a bored cat.”

—Elaine Weil

5.1 Introduction

Population dynamics in ecosystems, which determine extinction, survival, coexistence or oscillation of organisms, are governed by a variety of non-linear multi-species interactions (77-79). Exploration of such vital patterns compels mathematical models, which can be experimentally verified. Here, we present a synthetic ecosystem, programmed by Lingchong You, consisting of two genetically engineered *Escherichia coli* populations that communicate through “quorum sensing” and mutually regulate each other’s gene expression and survival via *de novo* engineered regulatory circuits. It resembles the canonical predator-prey system in terms of basic logic and dynamics. A mathematical model is developed by Hao Song to predict the plausible system dynamics (e.g., population densities of predator and prey) controlled by the gene circuits.

Definitive long-term experiments performed using the microchemostat microchemostat (6) validated the predator-prey behavior. The mathematical predictions of population dynamics conferred by the gene circuits and the biological measurements were in agreement. Such coherent interplay between experiments and mathematical analysis provides unique insights unavailable from other experimental approaches.

5.2 Predator-Prey Synthetic Ecosystem

The predator-prey system is one of the best-studied model systems in population biology (79-81). Although many natural ecosystems have been dissected with the predator-prey model (82, 83), the naturally occurring systems are generally difficult to examine experimentally because of long generation times, genetic heterogeneity, and fluctuations in the environment. To circumvent these limitations, aquatic microorganisms that involve predator-prey relations have been adopted as model ecosystems to examine significant theoretical predictions, such as oscillations (84, 85), chaos (86), the effect of rapid evolution on ecological dynamics (87), and the maintenance of genetic diversity (88). In such natural predator-prey systems, experimental control parameters are generally limited to the nutrient concentration and dilution rate (84-88).

Synthetic ecosystems, such as the one described in this chapter, can facilitate broader investigation of natural ecosystems. In addition to external (environmental) stimuli, synthetic ecosystems permit direct manipulation of intrinsic parameters such as

growth rate, death rate, and strength of cell-cell communication. The generic nature of the design principle in a synthetic ecosystem makes it portable (readily adaptable) to other ecological interactions including “competition” and “mutualism”. Moreover, more species could be incorporated into the system to enable exploration of complex dynamics in multi-species microbial communities. For example, gastrointestinal bacteria essentially form a microbial ecosystem that is critical for human health (89, 90). The constitution of the ecosystem remains stable throughout adulthood, and it is recognized that deregulation of the balance among the bacterial populations can cause immune disorders or cancers (89). However, the basic stability mechanism of this microbial ecosystem is poorly understood due to the difficulty in isolation and *in vitro* culturing of gut bacteria. This is because they often require growth factors supplied by others species within the community in order to grow. We expect that synthetic systems, such as the one described in this chapter, will improve the understanding and control of these natural microbial ecosystems.

5.2.1 Circuit Description

Bacteria employ a family of “quorum sensing” (QS) signals, acyl-homoserine lactones (AHLs), to accomplish cell-cell communication. AHL molecules, which are synthesized by ‘I’ proteins, can freely diffuse across the cell membrane (60, 63) and activate transcription when bound to their cognate ‘R’ transcription factors (64) (section 4.1.2).

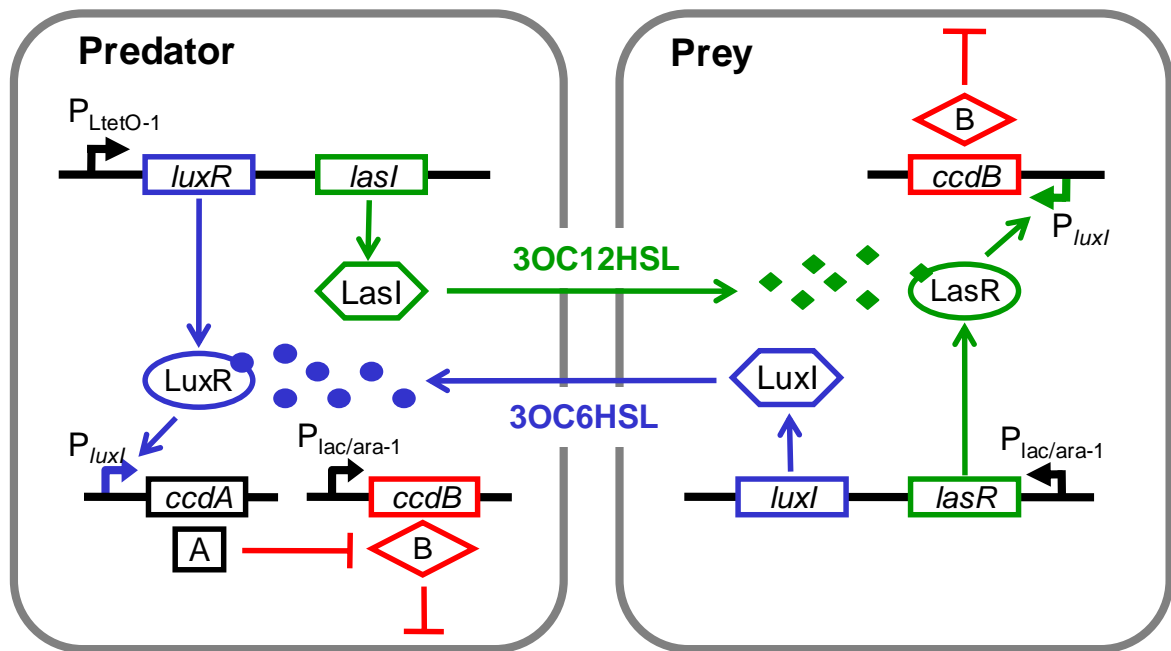


Figure 5.1. A synthetic predator-prey ecosystem consisting of two types of cells controlling each other's survival and death *via* two different QS signals. The outer boxes represent cell walls. Arrows represent activation or production; blunt arrows represent inhibition or killing. "B" is a killer protein (CcdB), under the control of $P_{lac/ara-1(91)}$ in the predator cells and $P_{luxI(92)}$ in the prey cells. "A" is an antidote (CcdA) (93) under the control of P_{luxI} . Cognate elements of each QS module are indicated in the same color: the LuxI/LuxR system is in blue and the LasI/LasR system in green (94, 95). The QS genes in the predator cells are under the control of $P_{LtetO-1(91)}$, and those in the prey are controlled by $P_{lac/ara-1}$. Filled circles represent 3OC6HSL and filled diamonds represent 3OC12HSL. The predator-prey interaction is activated by IPTG that turns $P_{lac/ara-1}$ promoter on. See main text and supplementary material for more details.

Figure 5.1 depicts two *E. coli* populations, ‘predator’ and ‘prey’, which communicate and regulate each other’s density *via* a pair of distinct QS systems(94, 95): the LuxI/LuxR system from bacterium *Vibrio fischeri* and the LasI/LasR system from bacterium *Pseudomonas aeruginosa*. When the ‘prey’ density is low, the ‘predator’ cells are killed due to constitutive expression of a suicide gene (*ccdB*) (93). The prey cells produce an AHL (3OC6HSL by LuxI), which diffuses through the medium into the predators. As the prey density increases, 3OC6HSL accumulates in the predator cells. When it reaches a sufficiently high concentration, it activates its cognate transcriptional regulator (LuxR) and induces expression of an antidote gene (*ccdA*) to rescue the predator cells.

The predator cells produce a different AHL (3OC12HSL by LasI) that diffuses into the prey cells where it binds LasR and activates expression of *ccdB*, effecting ‘predation’. This system satisfies the broader definition of predation for a two-species ecosystem, where one species (prey) suffers from the growth of the second (predator) and the second benefits from the growth of the first. However, it differs from the canonical predator-prey system in that, instead of acting as a food source for the predator, the prey provides an ‘antidote’.

5.2.2 Circuit Optimization

Using ordinary differential equations we modeled the major kinetic events during the functioning of this circuit (section 5.4.1).

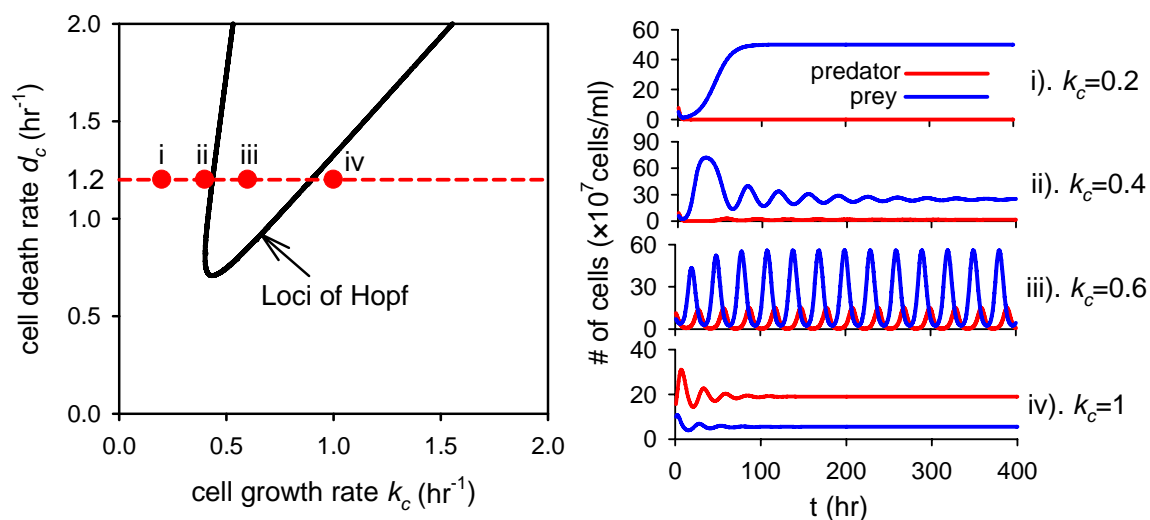


Figure 5.2. Dynamics of predator and prey's population density are elucidated by the bifurcation diagram in the parameter space of the cell growth rate $k_c (= k_{c1} = k_{c2})$ and the killing rate constant $d_c (= d_{c1} = d_{c2})$ of equations ((5.14)—(5.17)). The curve represents loci of Hopf bifurcation points. Typical time courses of population densities for specific parameter sets are illustrated. Parameter values used here in equations ((5.14)—(5.17)) are: $v_{A1} = v_{A2} = 1 \text{ nM mL hr}^{-1}$, $d_{Ae1} = d_{Ae2} = 0.7 \text{ hr}^{-1}$, $K_1 = K_2 = 10 \text{ nM}$ and $D = 0.1 \text{ hr}^{-1}$.

The model predicts extinction, coexistence, and oscillatory dynamics if the combination of cell growth, cell death controlled by AHL, as well as production and degradation of AHL reaches an appropriate balance (figure 5.2).

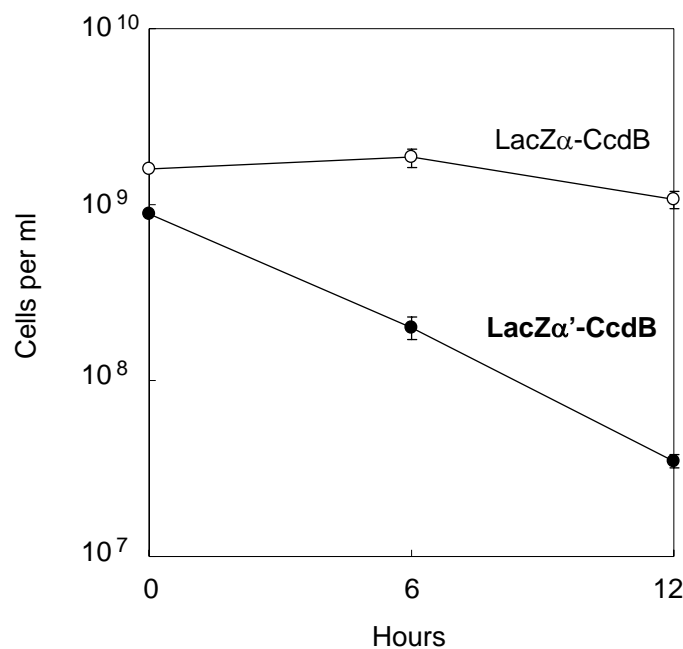


Figure 5.3. Killing dynamics by LacZ α -CcdB and LacZ α' -CcdB. In plasmids placCcdB (LacZ α -CcdB, p15A origin, Kan^R) and placCcdBs (LacZ α' -CcdB, p15A origin, Kan^R), the killer gene is under the control of P_{lac/ara-1} promoter. Each was introduced into Top10F⁺ (Invitrogen) cells. Full-grown cultures were incubated in 2 mL of LB media with 1mM IPTG at 37 °C and 250 rpm. in 12 mL test tubes. Colony forming units (CFU) were measured after IPTG induction at different time points as indicated.

Next, we experimentally implemented and optimized the circuit, guided by mathematical modeling. For instance, to facilitate generation of oscillations, bifurcation analysis requires that the killing rate constants (d_{c1} and d_{c2}) by CcdB be sufficiently greater than the growth rates (k_{c1} and k_{c2}) (figure 5.2).

Our experiments indicated that the original *LacZ α* -CcdB fusion protein, which was cloned from pZErO-2 vector (Invitrogen) and used in our population control circuit (96), would not be sufficiently lethal (data not shown). To overcome this limitation, we constructed a new *LacZ α'* -CcdB protein lacking 32 amino acids in *LacZ α* , which resulted in an 8-fold increase in potency compared with the full-length protein (figure 5.3). This shorter, more potent *LacZ α'* -CcdB fusion protein is referred to as ‘CcdB’ in this chapter. Furthermore, it was previously shown that both active LasR and active LuxR can activate gene expression *via* a *luxI* promoter (P_{luxI}) (97). We thus used P_{luxI} both to drive the *ccdA* gene in the predator cells (regulated by LuxR) and to drive the *ccdB* gene in the prey cells (regulated by LasR). Experiments also revealed that LuxI/LuxR and LasI/LasR systems had very low cross talk between their signals (figure 5.4). To achieve optimal expression levels and timing for circuit components, we tested many combinations of promoters, replication origins, and bacterial strains and decided to focus on two pairs of configurations (figure 5.5). The first pair is predator (MG1655 strain)/prey (Top10F⁺ strain) (figure 5.5A); the second pair is predator (Top10F⁺ strain)/prey (Top10F⁺ strain) (figure 5.5B). Since the MG1655 strain of *E. coli* grows faster and to a higher steady-state

population density than the Top10F⁺ strain, these two pairs represent two different scenarios of predator and prey growth and interacting dynamics.

Both synthetic ecosystems are activated by isopropyl-b-D-thiogalactopyranoside (IPTG), which induces *wdB* expression in the predators and the QS system in the prey. To minimize time delay in rescuing the predator by its survival signal (3OC6HSL), the corresponding QS system was placed under the control of P_{LtetO-1} promoter (91), which would be activated by applying anhydrotetracycline (aTc) to remove the repression of TetR repressor. Similarly, this strategy would also minimize the time delay in 3OC12HSL synthesis and thus initiation of prey killing. We found that prey cells were unable to effectively rescue the predator cells if the predator circuit was in a high-copy-number plasmid (e.g., ColE1 origin with a copy number of ~70/cell). Therefore, to moderate production rates of CcdB, we implemented the predator circuit in a low-copy-number plasmid (SC101 origin with a copy number of ~3-4/cell). Finally, a destabilized green fluorescent protein gene (*gfp_m*) was introduced into the predator (or prey, depending on the predator-prey pair used, see figure 5.5) to capture dynamic changes in cell density within mixed cultures.

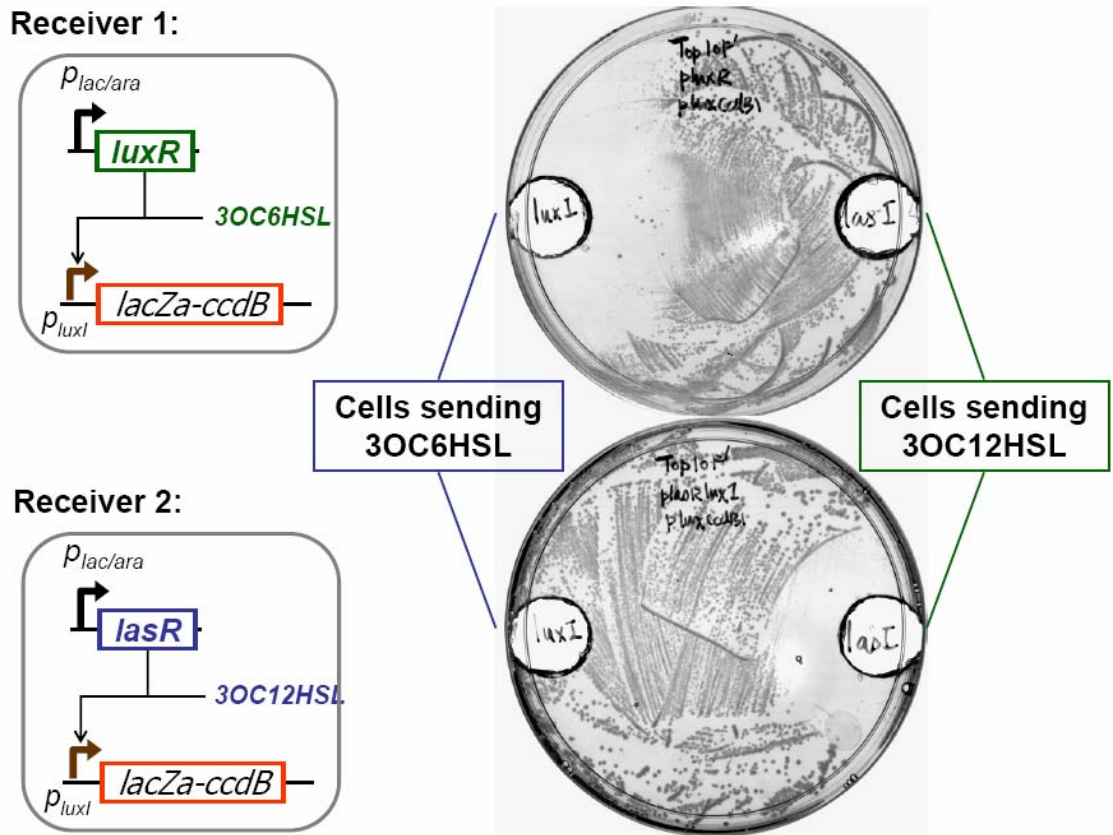


Figure 5.4. Test of communication and cross talk between LuxI/LuxR and LasI/LasR systems. Receiver cells were spread on agar plates with IPTG, which induced expression of the transcription regulators (LuxR or LasR). Receiver cells will express a killer protein (*LacZa-ccdB*) when sensing appropriate signals. Receiver 1, which encodes LuxR, responded to cells (Top10 cells containing pLuxRI) sending 3OC6HSL (as indicated by the death zone around the sender cells) but did not respond to cells (Top10 cells containing pLasRI) sending 3OC12HSL. Receiver 2, which encodes LasR, responded to cells sending 3OC12HSL but not cells sending 3OC6HSL.

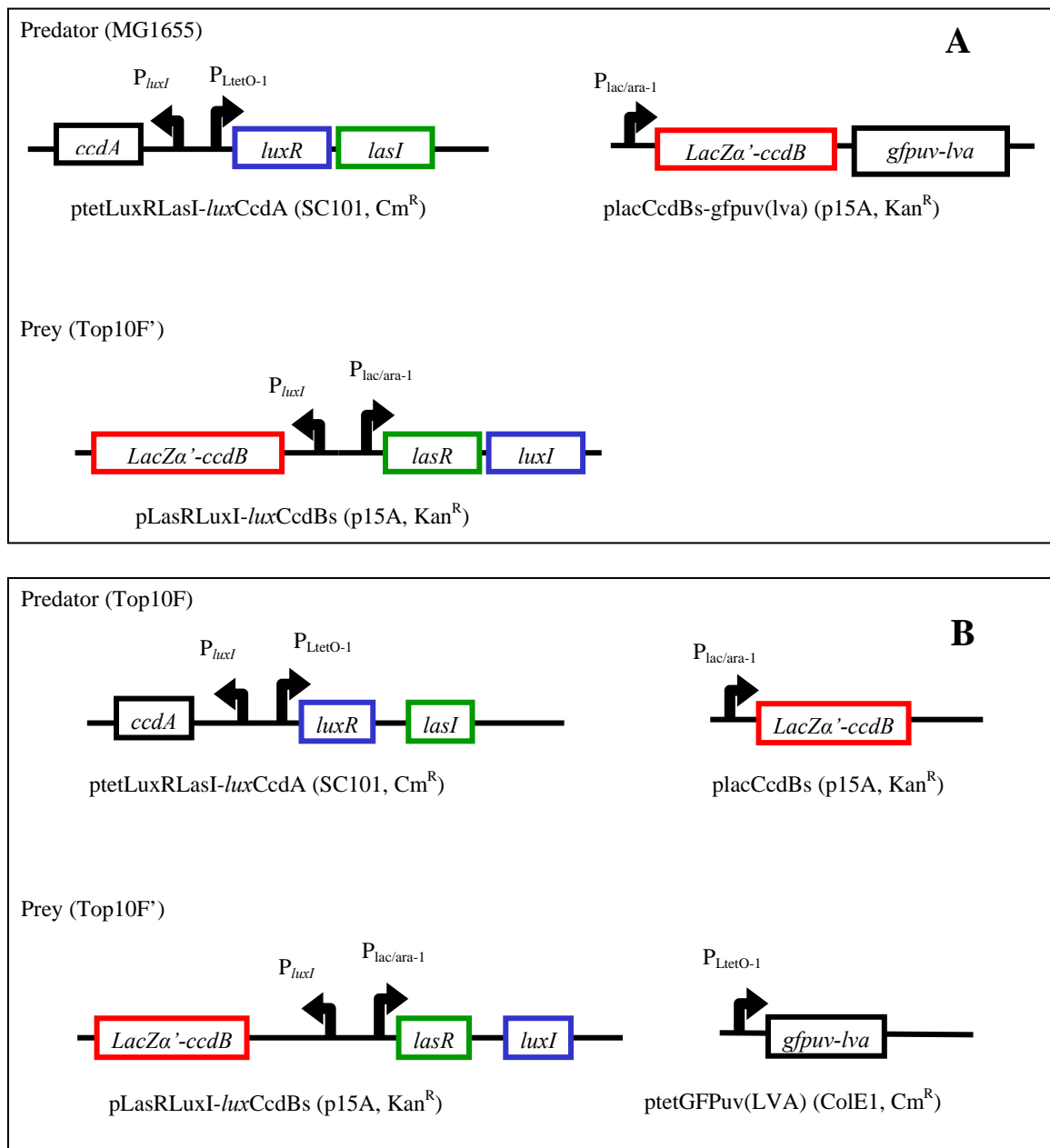


Figure 5.5. Configurations of the plasmids in two pairs of predator and prey. Each strain carries two plasmids. The parentheses after the plasmid name show (replication origin, selection marker gene). *LacZa'-ccdB* is derived from *lacZa-cddB* by deleting in frame 96 base pairs (see methods). (A) The pair of predator (MG1655) and prey (Top10F'). (B) Another pair of predator (Top10F') and prey (Top10F').

5.3 Results

5.3.1 Macroscale Experimental Verification

We verified the basic function of each population (predator or prey) independently in liquid cultures using IPTG and the corresponding AHL (supplied exogenously). Figure 5.6 illustrates the individual growth dynamics of the pair of predator (Mg1655)/prey (Top10F⁷). As shown in figure 5.6A, in the OFF cultures containing neither IPTG nor 3OC6HSL, predator cells grew to a relatively high density. Growth was inhibited in the ON cultures containing 0.1mM of IPTG, which fully induced *cdB* expression. However, predator cells induced with IPTG were rescued by 3OC6HSL (300nM), which activated antidote (*cdA*) expression. We note that the rescued predators (with IPTG and 3OC6HSL) grew slower than their OFF condition (figure 5.6A). This growth retardation could be due to the metabolic burden involved in the maintenance and functioning of the circuit.

As shown in figure 5.6B, prey cells grew in medium containing only IPTG but perished when 3OC12HSL was simultaneously present. However, the primed prey population (with IPTG only) grew slightly less in comparison that in the OFF condition with no inducers. This growth retardation could be attributed to the metabolic burden of circuit components, basal level *cdB* expression due to cross talk between 3OC6HSL and LuxR, or both.

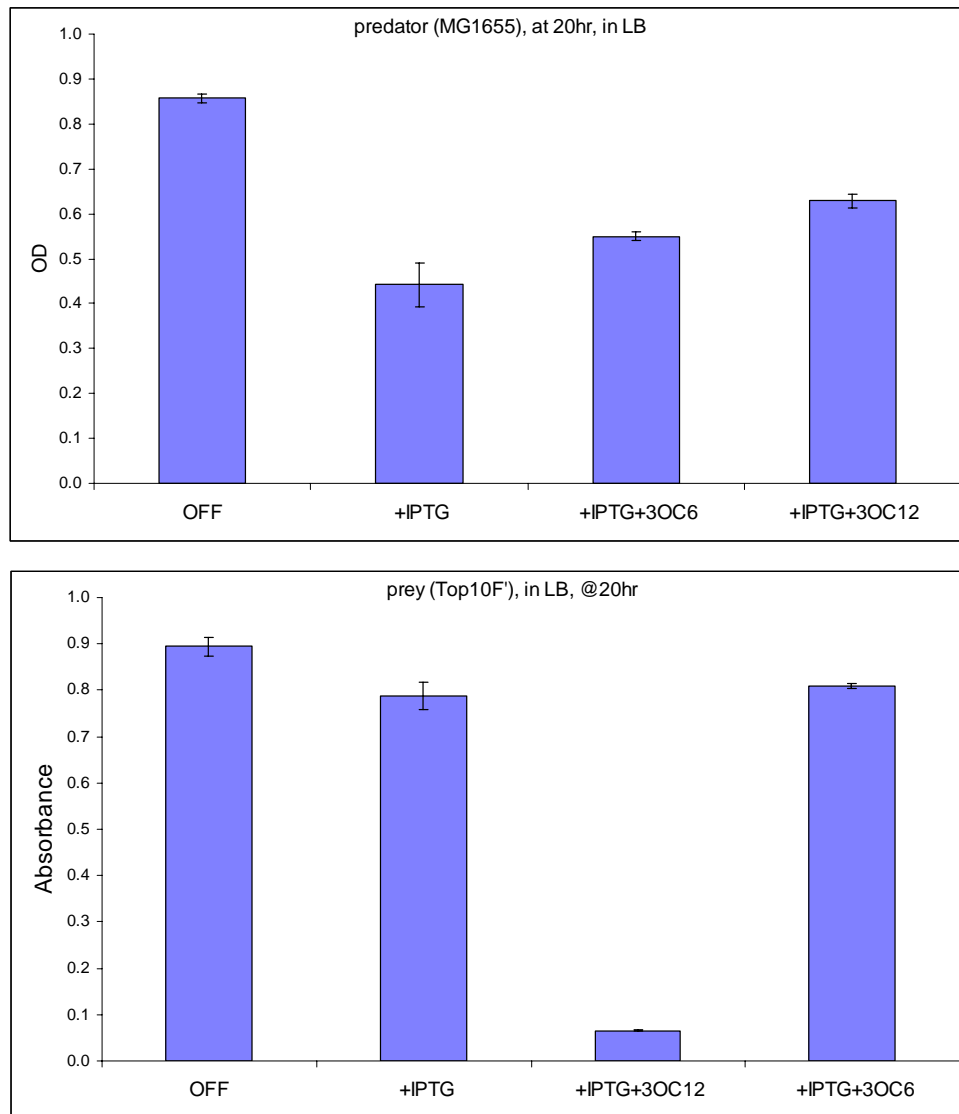


Figure 5.6. Individual behaviors (without interactions) of the predator (strain MG1655) (top) and the prey cells (strain Top10F) (bottom).

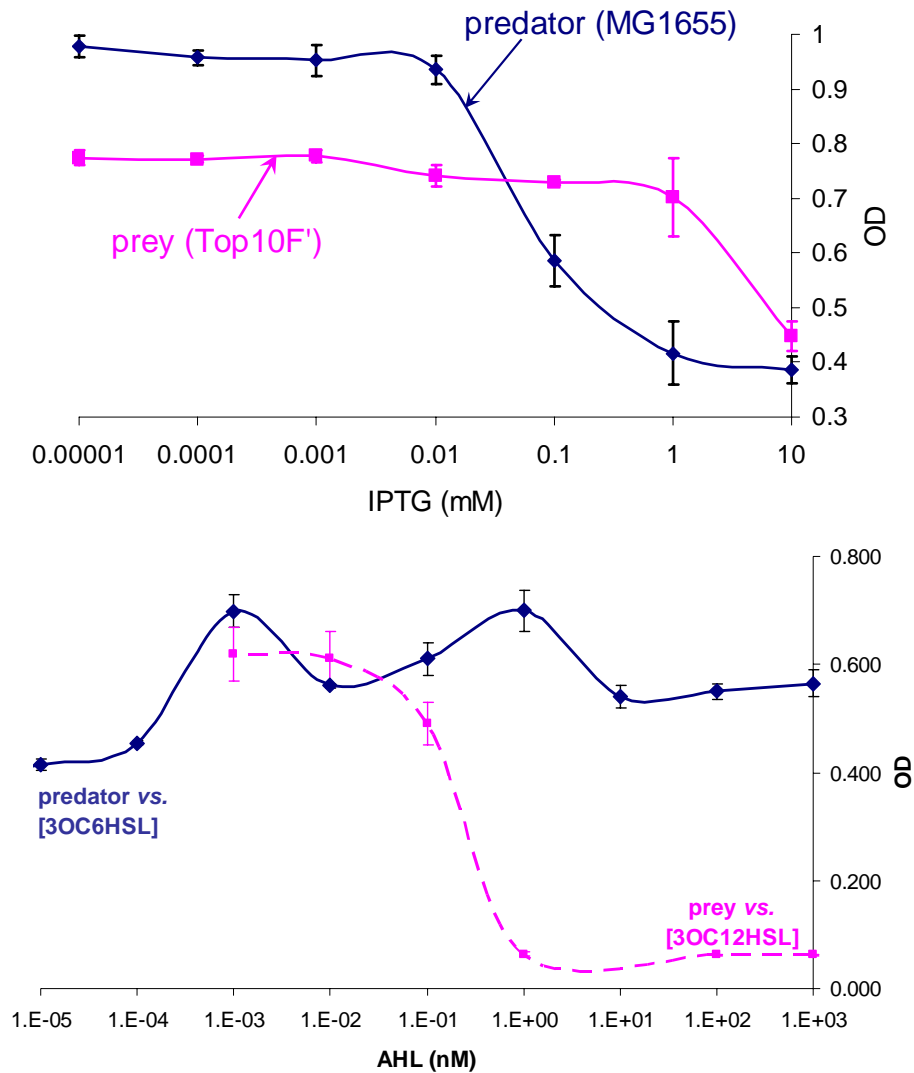


Figure 5.7. IPTG dose-response curves of the predator and prey cells. Six ml of TBK medium containing chloramphenicol and kanamycin was inoculated with a single colony and was divided into three 2ml cultures: “+IPTG” culture contains 1 mM IPTG; and “+IPTG/AHL”, 1mM IPTG/100 nM AHL, respectively. After 16 hours of incubation (bars in light gray), optical density (OD) of these cultures was measured with a microplate reader (see section materials and methods). Error bars represent standard deviation of duplicate cultures.

Dose-response curves (figure 5.7) indicate that 0.1 mM IPTG was the saturation concentration for the activation of gene circuits, whereas 10^{-4} mM IPTG had a negligible effect on the cell growth. This information beacons us toward the correct choice of experimental conditions when exploring the effect of circuit activation (i.e., IPTG activation level) on the interaction dynamics of predator-prey populations (figure 5.8).

5.3.2 Microchemostat Characterization

We further characterized the circuit dynamics using a continuously operated microchemostat (98), which provides a platform for long-term, automated measurement of programmed population dynamics with single cell resolution. Importantly, the microchemostat reduces the likelihood for mutants to evade circuit function and take over the culture, by drastically scaling down the culture volume (98). The microchemostat (figure 3.6) was redesigned to enable single-cell resolution fluorescence quantification (section 3.2.3) and to increase the number of reactors on a single chip from six to fourteen.

Figure 5.8 illustrates a typical growth dynamics of the synthetic predator-prey ecosystem (using the pair in figure 5.5A (predator (MG1655)/prey (Top10F⁺))). Initially, when the prey density was low, the predator density plummeted from ~ 2 cells/pL and fell below the detection limit of 0.03 cells/pL due to *ccdB* expression. As prey grew, they synthesized 3OC6HSL, which diffused into the predators and induced expression of an antidote gene (*ccdA*), ushering in a regime of positive growth by predators. In tandem with predator growth, the concentration of a different AHL signal (3OC12HSL

synthesized by the predators) increased and at sufficiently high density, infiltrated the prey cells and unleashed the prey killer gene. Consequently, at day 4, death ensued within the prey as the predator population further enjoyed steady increase to about 2 cells/pL. Further decreases in the prey density weakened the 3OC6HSL signal, which in turn created antidote (*cdA*) deficiencies in predator cells. In the absence of antidote, the predator population, which was no longer immune to its suicide gene, began to wane. With the consequential decreases in the 3OC12HSL signal concentration, the prey population recovered. Under these conditions the predator population suffered due to the growth of the predator yet the predator depended on the presence of the prey. The ecosystem in the bottom panel of figure 5.8 eventually oscillated for about $2\frac{1}{2}$ cycles.

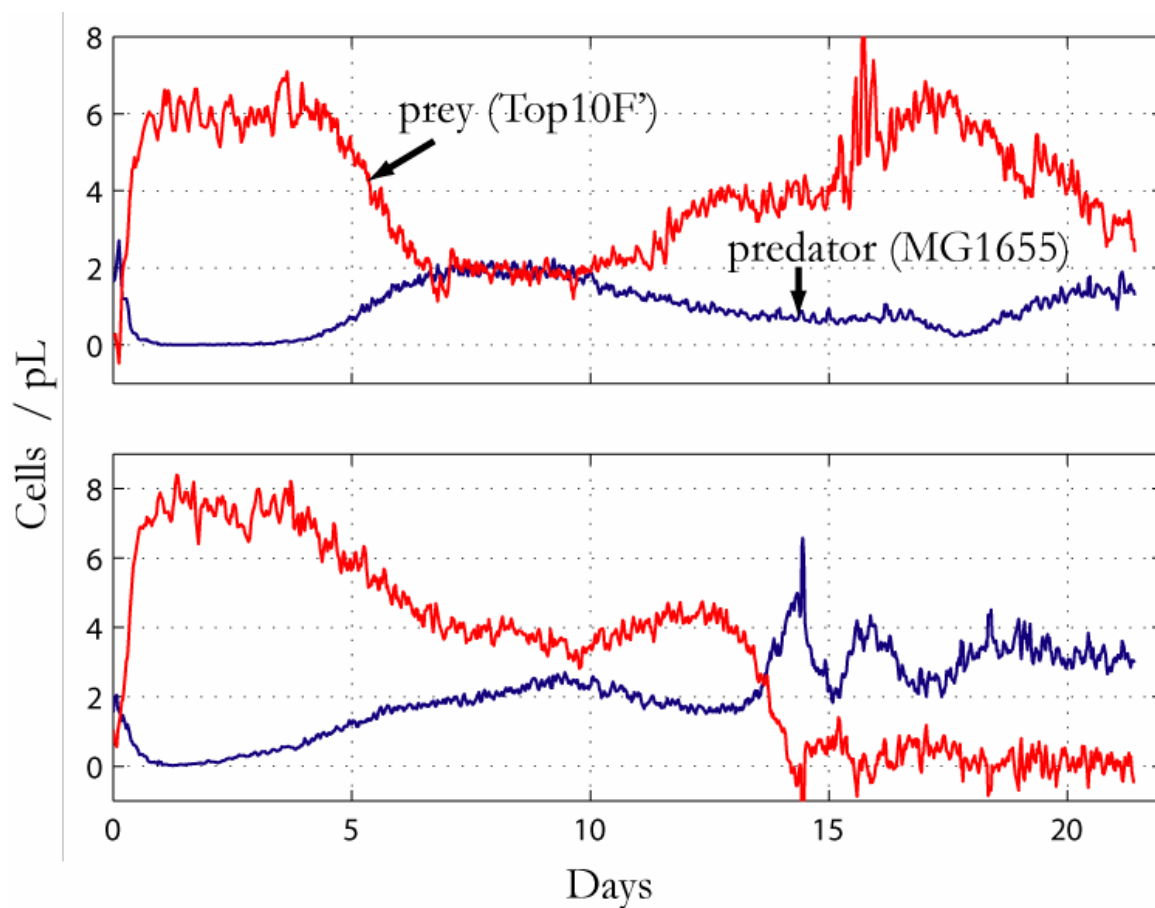


Figure 5.8. Typical growth dynamics of a synthetic predator-prey ecosystem in a microchemostat (using the pair in figure 5.5A (predator (MG1655) / prey (Top10F⁺)) on a single chip at two different IPTG induction rates (250 μM top and 50 μM bottom). Cells were grown at 37 $^{\circ}\text{C}$ in LBK medium (see section) at a dilution rate of 0.12 hr^{-1} for the first 9 $\frac{1}{2}$ days and 0.16 hr^{-1} during the rest of the experiment.

Figure 5.9 illustrates a typical set of interaction dynamics of the synthetic predator-prey ecosystem at different IPTG induction levels using the pair in figure 5.5A (predator (MG1655) / prey (Top10F³)). The behavior of the circuit depended on the IPTG induction level.

At high induction levels (0.05Mm or greater, figure 5.9 row 1) the predator-prey circuit was fully induced. In the beginning, with a low prey density, the predator density fell below the detection limit of 0.03 cells/pL due to *cdB* expression while the prey population increased ultimately to ~ 6 cells/pL. As prey density increased, it induced expression of an antidote gene (*cdA*), rescuing the predator population between 50 and 100 hr. Increase in the predator density effected a decrease in the prey density through circuit predation. The dominant outcome under these conditions was for both the predator and prey populations to ultimately arrive at a steady state of ~ 2 cells/pL. In a few instances, the predator cells did not survive their first brush with death, which allowed the prey cells to take over the reactor (figure 4, row 1, reactor 3). At these concentrations, the circuit behavior was qualitatively identical except for the fact that increase in the IPTG concentration delayed the recovery of the predator cells during the first cycle.

At moderate IPTG induction levels (0.005–0.01 mM, figure 5.9, row 2), the predator-prey system was unstable. At times, it exhibited oscillatory dynamics (figure 5.9 row 2, columns 1, 2 and 4) and at times the prey density dominated the reactor (row 2, reactor 3). Such instability could be attributed to noise in the circuit induction level at such low IPTG concentrations.

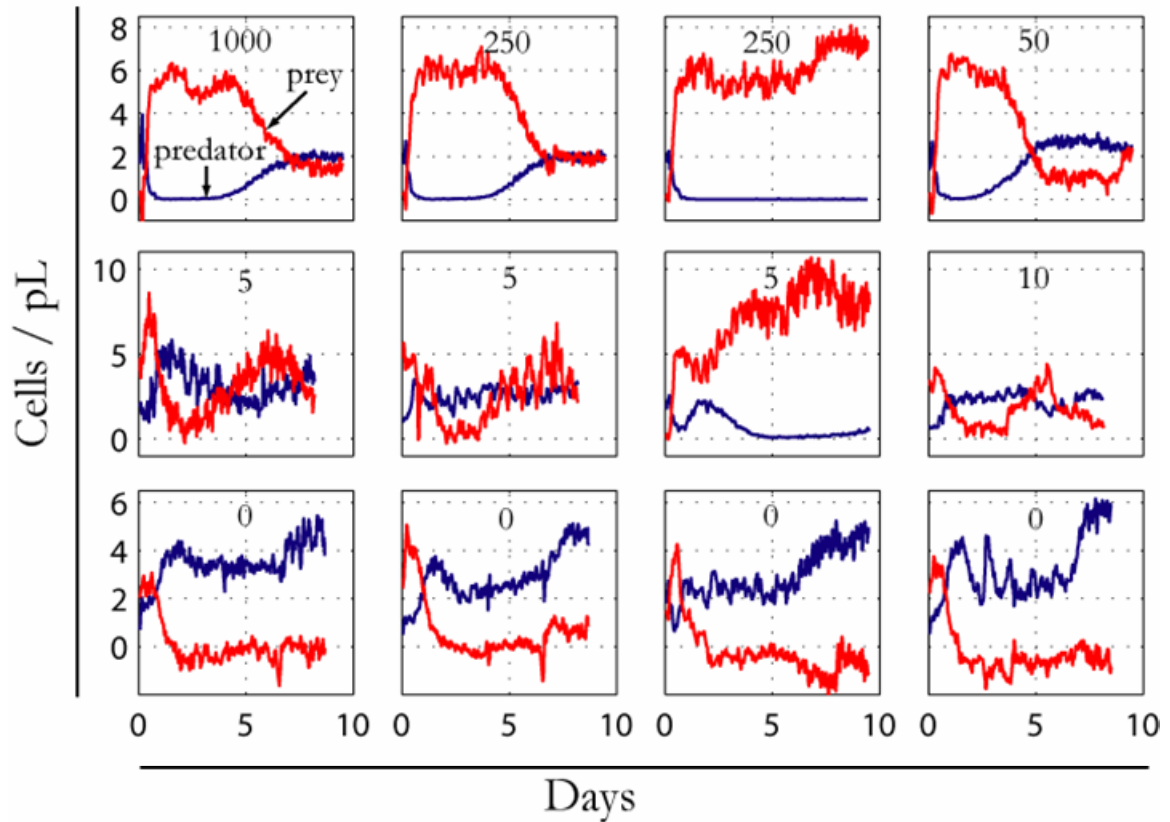


Figure 5.9. Long-term characterization of predator [strain MG1655]/prey [strain Top10F'] (figure 5.5A) dynamics with various IPTG induction levels in the microchemostats at a fixed dilution rate of 0.12 hr^{-1} . With no induction, prey cells are outcompeted and ultimately driven out of microchemostat. At increased IPTG levels (IPTG = 0.05 mM or above), oscillatory dynamics of predator and prey populations may be obtained.

Without IPTG induction (IPTG = 0, figure 5.9, row 3), predator and prey had, at most, basal level interactions through engineered communication. Consistent with competition dynamics in the chemostat (chapter 1), the predator (strain MG1655), which grows faster than the prey (strain Top10F²), eventually (after ~50hr) drove the prey population to extinction.

These results were consistent with bifurcation analysis using our simple model (figure 5.10) by accounting for the effects of IPTG on 3OC6HSL production by the prey cells, as well as CcdB expression by the predator cells. At sufficiently low IPTG levels, there was little killing of predator cells. As a result, the predator population often dominated due to its natural growth advantage, leading to the washout of prey cells. Increasing IPTG above a critical level (denoted by Hopf bifurcation point) elicits oscillation in predator and prey populations.

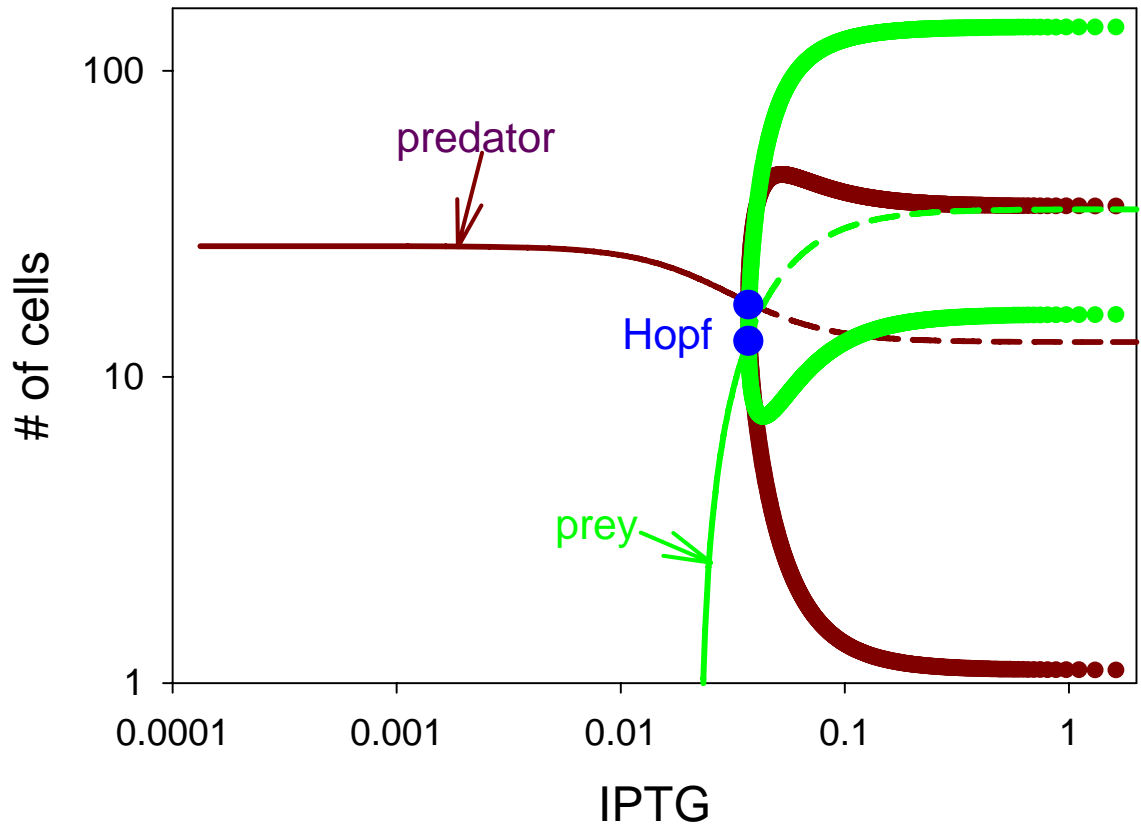


Figure 5.10. Bifurcation diagram of the number of predator cells (dark red) and prey cells (green) versus IPTG level. Solid lines depict stable steady state, dashed lines unstable steady states. Filled dots denote amplitudes of oscillations. Blue dot represents Hopf bifurcation point. The parameters values used here in the equations ((5.14)—(5.19)) are: $k_{c1} = 2 \text{ hr}^{-1}$, $k_{c2} = 1 \text{ hr}^{-1}$, $v_{A1} = 1 \text{ nM mL hr}^{-1}$, $d_{Ae1} = d_{Ae2} = 1 \text{ hr}^{-1}$, $K_1 = K_2 = 10 \text{ nM}$, $d_2 = 1.2 \text{ hr}^{-1}$ and $D = 0.12 \text{ hr}^{-1}$.

According to the theory of reactor miniaturization (section 3.3), the minimum attainable cell density ($\rho_{\min} = 1/V$, corresponding to 1 cell per reactor volume) goes up as the working volume shrinks. This sets a lower limit to volume miniaturization, for a given cell density, below which cell culturing would result in no cells in the entire reactor. Due to the extremely small volume ($\sim 10\text{nL}$) of the microchemostat reactor, the density of predator cells in each culture often fell below the minimum acceptable density during an oscillation trough leading to washout.

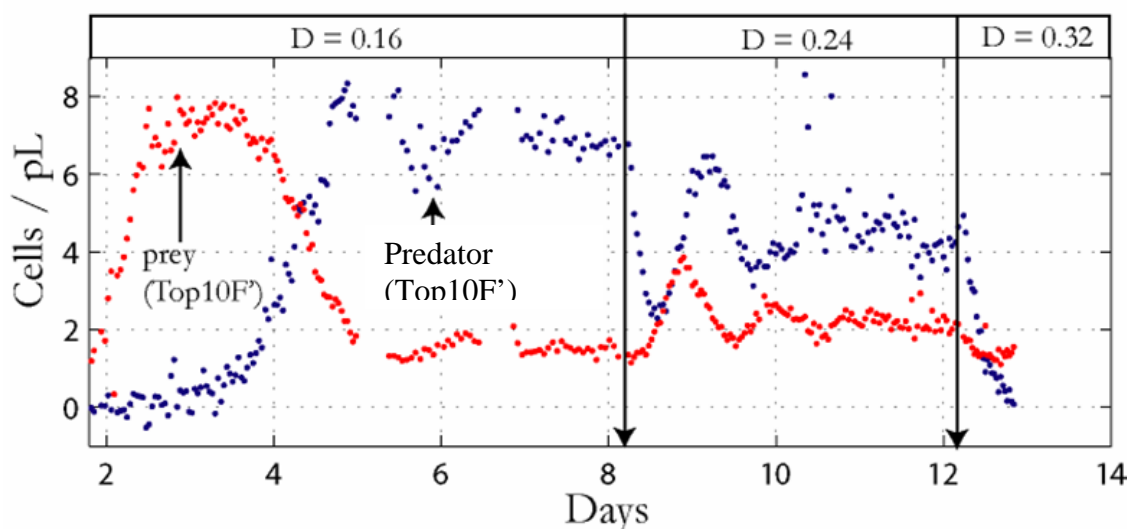


Figure 5.11. Dependence of systems (the pair of predator (Top10F⁺)/prey (Top10F⁻)) dynamics on dilution rate. Experimental dynamics of predator and prey populations at different dilution rates in microchemostat.

We further tested the effect of the dilution rate (D) on the systems dynamics of predator (Top10F⁺) / prey (Top10F⁻) ecosystem (the pair shown in figure 5.5B). Figure 5.11 experimentally illustrates a situation in which the predator and prey population coexist at $D = 0.16 \text{ hr}^{-1}$, and damped oscillatory dynamics at $D = 0.24 \text{ hr}^{-1}$, given 0.05mM IPTG induction. When the dilution rate is further increased to at $D = 0.32 \text{ hr}^{-1}$, unlike the prey, the predator gets washed out.

Simulations (figure 5.12) qualitatively account for the experimental observations (figure 5.11A).

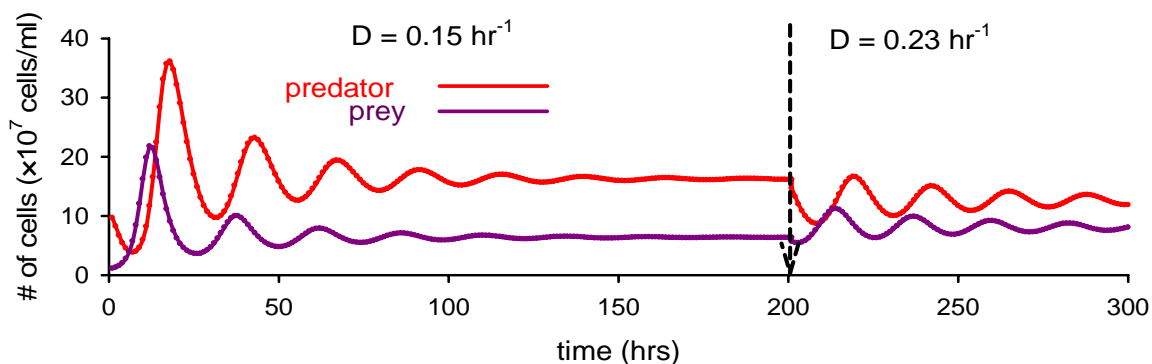


Figure 5:12. Dependence of systems (the pair of predator (Top10F⁺)/prey (Top10F⁻)) dynamics on dilution rate. Temporal dynamics by modeling. The parameter values used here in equations ((5.14)—(5.17)) are: $k_{e1} = k_{e2} = 1 \text{ hr}^{-1}$, $d_{e1} = d_{e2} = 1.2 \text{ hr}^{-1}$, $v_{A1} = v_{A2} = 1 \text{ nM mL hr}^{-1}$, $d_{Ae1} = d_{Ae2} = 0.7 \text{ hr}^{-1}$, and $K_1 = K_2 = 10 \text{ nM}$.

In writing down the kinetic rate expressions for these reactions, we make the following assumptions:

- (1) Cell growth follows logistic kinetics (section 2.5.4) with a specific growth rate of k_{ci} (min^{-1} ; $i = 1$ (predator) or 2 (prey); this convention is used throughout the text unless otherwise noted) and a carrying capacity of c_{max} for the predator and prey mixture. Numerical analysis shows that minimizing competition facilitates oscillatory behavior by preventing the total domination by one species. We further assume that the cell death rate is proportional to the concentration of the lysis protein in the cell, with a rate constant of d_i (nM min^{-1})
- (2) All components other than the cells are assumed to decay with first-order kinetics.
- (3) For constitutively expressed genes, the mRNA production rate is assumed to be constant. The synthesis rate of a protein is assumed to be proportional to the concentration of the corresponding mRNA.
- (4) The synthesis of AHLs occurs at a constant rate. This is equivalent to assuming that (a) the substrates for the synthesis reaction are in excess or sustained at a constant concentration and that (b) the corresponding AHL synthases (LuxI or RhII) each have a constant intracellular concentration, which in turn can be achieved by expressing these enzymes constitutively.
- (5) The cognate transcriptional regulators (LuxR or RhIR) for AHLs are constitutively expressed.

- (6) Regulation of lysis gene expression follows Michaelis-Menten-type kinetics. This is equivalent to assuming that (a) binding of a regulator to the promoter is fast and that (b) the rate of transcription is proportional to the concentration of active promoter—i.e., the concentration of the bound DNA if the promoter is to be activated, or that of the free DNA if the promoter is to be repressed. Note that synthesis of the lysis mRNA is activated by the active RhlR in the prey, but repressed using an engineered promoter (99) by the active LuxR in the predator. This assumption implies that there is no basal level of gene expression for uninduced or fully repressed promoters. We find that assuming small basal level of gene expression in these cases does not change the overall dynamics.
- (7) Each AHL has uniform concentrations in a cell and in the well-mixed medium, and the only barrier for AHL transport is the cell membrane. The flux of AHL across the cell membrane is proportional to the concentration difference between the intracellular and extracellular space.
- (8) The binding of an AHL to its cognate regulator, the dissociation of the active regulator, and the dimerization of the active regulator follow mass action kinetics.
- (9) There is no crosstalk between different AHL signals.

The state variables and parameters are described in detail in Tables 5.2 and 5.3. Based on the listed reactions, we write a system of coupled ordinary differential equations (ODEs) to describe the interacting species.

Cell (predator- c_1 , prey- c_2) growth and death

$$\frac{dc_1}{dt} = k_{c_1}c_1\left(1 - \frac{c_1}{c_{\max}}\right) - \frac{d_1E_1c_1}{1 + \alpha_A A} - Dc_1, \quad (5.1)$$

$$\frac{dc_2}{dt} = k_{c_2}c_2\left(1 - \frac{c_2}{c_{\max}}\right) - d_2E_2c_2 - Dc_2, \quad (5.2)$$

Expression of regulator genes ($luxR$ for predator; $lasR$ for prey, denoted by M_{Ri}) and decay of products

(R_i)

$$\frac{dM_{Ri}}{dt} = v_{MRi} - d_{MRi}M_{Ri}, \quad (5.3)$$

$$\frac{dR_i}{dt} = k_{Ri}M_{Ri} - d_{Ri}R_i - k_{Pi}A_{ij}R_i + d_{Pi}P_i, \quad (5.4)$$

Activation of regulator-inducer complex ($R_1-A_{i2} = P_1$, and $R_2-A_{i1} = P_2$)

$$\frac{dP_i}{dt} = k_{Pi}A_{ij}R_i - d_{Pi}P_i, \quad (5.5)$$

Expression of antidote gene ($ccdA$, denoted by M_A here) and protein (A) in predator

$$\frac{dM_A}{dt} = \frac{k_{MA}\alpha_{MA}P_1^\beta}{1 + \alpha_{MA}P_1^\beta} - d_{MA}M_A, \quad (5.6)$$

$$\frac{dA}{dt} = k_A M_A - d_A A, \quad (5.7)$$

Expression of lysis (or killer) genes (M_{E1} , M_{E2}) and decay of products (E_1 , E_2)

$$\frac{dM_{E1}}{dt} = \alpha_{ME1} - d_{ME1}M_{E1}, \quad (5.8)$$

$$\frac{dM_{E2}}{dt} = \frac{k_{ME2}\alpha_{ME2}P_2^\beta}{1 + \alpha_{ME2}P_2^\beta} - d_{ME2}M_{E2}, \quad (5.9)$$

$$\frac{dE_i}{dt} = k_{Ei}M_{Ei} - d_{Ei}E_i, \quad (5.10)$$

where β (approximately 1.2) represents the cooperation Hill coefficient of gene expression.

Product, diffusion and decay of AHLs (A_i : 3OC12HSL from predator; A_2 : 3OC6HSL from prey)

$$\frac{dA_i}{dt} = v_{Ai} - \eta_i(A_i - A_{ei}) - d_{Ai}A_i$$

$$(5.11)$$

$$\frac{dA_{ei}}{dt} = \eta_i \frac{c_i}{1 - c_1 - c_2} (A_i - A_{ei}) - \eta_i \frac{c_j}{1 - c_1 - c_2} (A_{ei} - A_{ai}) - d_{Aei}A_{ei} - DA_{ei}$$

$$(5.12)$$

$$\frac{dA_{ai}}{dt} = \eta_i(A_{ei} - A_{ai}) - d_{Aai}A_{ai} - k_{Pj}A_{ai}R_j + d_{Pj}P_j$$

$$(5.13)$$

These equations highlight the overall symmetric structure of the model: the same form of kinetics is followed by the corresponding components in the two cell types, except for the transcription of lysis genes, which are regulated differently in the two cell

types. In equation (5.12), the rate of AHL diffusion must be scaled for the extracellular AHL concentrations by the ratio of the intracellular volume to the extracellular volume, since the AHLs will be diluted in the extracellular space. In the same equation, the index j represents the source cell for the production of AHL i .

5.4.1 Simplification of the Model

To simplify the model, we assume that several components are at a quasi-steady state. These components include all mRNAs, transcriptional regulators, killer proteins. This is equivalent to assuming that processes leading to changes in these species are at a much faster timescale than the rest of the processes. We find that these simplifying assumptions will not significantly change the qualitative nature of the system dynamics.

By solving for the steady state levels of these variables and substituting them into the remaining equations, we reduce the full model into 4 ODEs: two equations describing the cell populations, two describing the levels of the AHLs in the medium. The major difference occurs in the equations describing the different effects of the two AHLs in the death of predator and prey cells.

$$\frac{dc_1}{dt} = k_{c1}c_1\left(1 - \frac{c_1}{c_{\max}}\right) - d_{c1}c_1 \frac{K_1}{K_1 + A_{e2}^\beta} - Dc_1, \quad (5.14)$$

$$\frac{dc_2}{dt} = k_{c2}c_2\left(1 - \frac{c_2}{c_{\max}}\right) - d_{c2}c_2 \frac{A_{e1}^\beta}{K_2 + A_{e1}^\beta} - Dc_2, \quad (5.15)$$

$$\frac{dA_{e1}}{dt} = k_{A1}c_1 - (d_{Ae1} + D)A_{e1}, \quad (5.16)$$

$$\frac{dA_{e2}}{dt} = k_{A2}c_2 - (d_{Ae2} + D)A_{e2}, \quad (5.17)$$

where c_i is the predator population (per 10^7 cells mL^{-1}), c_2 the prey population (per 10^7 cells mL^{-1}), A_{e1} the 3OC12HSL concentration (nM), and A_{e2} the 3OC6HSL concentration (nM). The parameters are defined as follows;

$$K_1 = \frac{1}{\left(\alpha_A \frac{k_A}{d_A} \frac{k_{MA}}{d_{MA}} + 1\right) \alpha_{MA} \left(\frac{k_{p1}}{d_{p1}} \frac{k_{R1}}{d_{R1}} \frac{v_{MR1}}{d_{MR1}}\right)^\beta}, \quad K_2 = \frac{1}{\alpha_{ME2} a_2^\beta}, \quad d_{c1} = d_1 \frac{k_{E1}}{d_{E1}} \frac{\alpha_{ME1}}{d_{ME1}},$$

$d_{c2} = d_2 \frac{k_{E2}}{d_{E2}} \frac{k_{ME2}}{d_{ME2}}$. These parameters lump effects of regulator synthesis, binding of

AHL to its cognate regulator, and dimerization of the active regulator.

The model indicates a cooperativity of 2 for the regulation of lysis gene synthesis. This value results from the dimerization of active regulators. However, the actual cooperativity is usually smaller than 2 (100), also see reference (101). This should come as no surprise. In simplifying the full model, we have assumed that reactions leading to expression of a lysis gene, which include binding of an AHL to its cognate regulator, dimerization of the active regulator, and binding of the active regulator dimer to DNA, are very fast. In reality, these assumptions will not hold strictly. To account for more general cases, we introduce a new parameter, β , to indicate the cooperativity of AHL regulation. As a result, regulation of lysis gene expression by an AHL takes the general form of Hill kinetics.

From these equations, the basic logic of the circuit is evident: an increase in c_2 (the prey density) will result in a decrease in A_{e2} , thus a reduced death rate for c_1 (the predator density). The increase in c_1 , however, will lead to an increase in A_{e1} , which in turn will lead to a larger death rate for the prey.

It is worth noting that further reduction of the model, for example by assuming the autoinducers (AHLs) to be at a quasi-steady state, will drastically change the qualitative behavior of the system (results not shown). In particular, the oversimplified system will fail to oscillate for all parameter settings. This additional analysis indicates that gene regulation needs to be at a similar time scale as the population dynamics in order to generate stable oscillations. It also highlights a key difference between this system and conventional two-species predator-prey systems, where two equations are sufficient to generate oscillations (102).

5.4.2 Parameter Values

The base parameter setting of the model is listed in table 5.4. Several parameter values are directly taken from the literature or are derived from literature data. For other parameters where we lack quantitative information (for example, those governing gene expression process), we use educated guesses that are biologically feasible.

The following parameter values are adopted from literatures¹² and are properly modified in biologically plausible region to simulate our experimental findings: growth rate of the cells (k_{c1} and k_{c2} , 0.4 hr⁻¹ (Top10F' strain) and 0.8 hr⁻¹ (MG1655 strain)), synthesis rate of AHL (k_{A1} , 0.1–0.6 nM mL hr⁻¹), degradation rate of AHL¹⁰ (d_{Ae} , 0.017 hr⁻¹ (3OC12HSL), 0.11 hr⁻¹ (3OC6HSL) at pH 7.0), a carrying capacity (C_m , 2*10⁹ cells mL⁻¹), and the concentration of AHL necessary to half-maximally activate p_{lacI} promoter (K_1 and K_2 , 10 nM) (103). The value of β is assumed to be 1.2 in this analysis. Death rates (d_{c1} and d_{c2} , 0.6 – 0.9 hr⁻¹) were determined from a decay curve of the number of live cells after induction of the killer gene (data not shown). “ D ” (hr⁻¹) is a dilution rate and

calculated with the relation $D = \frac{F}{T}$ where F is a fraction of dilution and T the time interval between each dilution event: for example, $D = 0.2$ for 25% discrete dilution ($F = 1/4$) every hour (T) (98). The bifurcation analyses were performed using XPPAUT (<http://www.math.pitt.edu/~bard/xpp/xpp.html>).

In the circuit diagram (figure 5.4), the $p_{lac-ara-1}$ promoter is activated upon exposure to IPTG. Subsequently, the predator killing rate (d_{c1}) is increased by increased ccdB expression, and the 3OC6HSL synthesis rate (k_{A2}) by prey is increased. To model the impact of IPTG on the circuit activation, we introduce the following functional expressions:

$$d_{c1} = 1.2 + 10 \times \frac{[\text{IPTG}]^2}{0.1^2 + [\text{IPTG}]^2}, \quad (5.18)$$

$$k_{A2} = 0.2 + 2 \times \frac{[\text{IPTG}]^2}{0.1^2 + [\text{IPTG}]^2}. \quad (5.19)$$

Table 5.1. Reactions described in the full model (1=predator and 2 = prey; the same form of kinetics is assumed for both the predator and the prey unless noted otherwise)

Reaction	Rate	Description
Population dynamics		
$\rightarrow c_i^a$	$k_i(c_{\max i} - c_i)/c_{\max i}$	Cell growth
$c_i \rightarrow$	$d_i E_i c_i$	Cell death
Expression of lysis genes and decay of products		
$\rightarrow E_i$	$k_{Ei} M_{Ei}$	Lysis protein production
$E_i \rightarrow$	$d_{Ei} E_i$	Lysis protein decay
$\rightarrow M_{E1}$	$\frac{k_{ME1}}{1 + \alpha_{ME1} Q_1}$	Transcription of lysis gene in the predator
$\rightarrow M_{E2}$	$\frac{k_{ME2} \alpha_{ME2} Q_2}{1 + \alpha_{ME2} Q_2}$	Transcription of lysis gene in the prey
$M_{Ei} \rightarrow$	$d_{MEi} M_{Ei}$	Lysis mRNA decay
Production, diffusion, and decay of AHLs		
$\rightarrow A_i^b$	v_{Ai}	Synthesis of AHL
$A_i \rightarrow$	$d_{Ai} A_{ai}$	Decay of AHL in its source cell
$A_i \rightarrow A_{ei}$	$\eta_i (A_i - A_{ei})$	Diffusion of AHL from its source cell
$A_{ei} \rightarrow$	$d_{Aei} A_{ei}$	Decay of AHL in the medium
$A_{ei} \rightarrow A_{ai}$	$\eta_i (A_{ei} - A_{ai})$	Diffusion of AHL to its target cell
$A_{ai} \rightarrow$	$d_{Ai} A_i$	Decay of AHL in its target cell
Production and decay of transcriptional regulators		
$\rightarrow R_i$	$k_{Ri} M_{Ri}$	Production of regulator
$R_i \rightarrow$	$d_{Ri} R_i$	Decay of regulator
$\rightarrow M_{Ri}$	v_{MRi}	Production of regulator mRNA
$M_{Ri} \rightarrow$	$d_{MRi} M_{Ri}$	Decay of regulator mRNA

Activation of transcriptional regulators by AHLs		
$R_i + A_{ai} \rightarrow P_i$	$k_{P_i} A_{ai} R_i$	Binding of AHL to its cognate regulator
$P_i \rightarrow R_i + A_{ai}$	$d_{P_i} P_i$	Dissociation of AHL-regulator complex
$2P_i \rightarrow Q_i$	$k_{Q_i} P_i^2$	Dimerization of AHL-regulator complex
$Q_i \rightarrow 2P_i$	$d_{Q_i} Q_i$	Dissociation of AHL-regulator complex dimer

^a Reactants for this reaction are not specified. Similarly, when the right-hand-side of a reaction is empty (for example for all the decay reactions), products of the reaction are not specified.

^b AHLs are indexed based on the their target cells: AHL1 is produced in the prey while AHL2 is produced in the predator.

Table 5.2. State variables of the full model

Variable	Description
c_i	Cell density ^a
E_i	[lysis-protein] ^b
M_{Ei}	[lysis-mRNA]
A_i	[AHL] in the source cell
A_{ei}	[AHL] in the medium
A_{ti}	[AHL] in the target cell
R_i	[regulator]
M_{Ri}	[regulator mRNA]
P_i	[AHL-regulator complex]
Q_i	[(AHL-regulator complex) ₂]

^a Cell density is measured as number of cells per mL.

^b The notation [X] represents the concentration of component X.

Table 5.3. Kinetic parameters of the full model

Parameter	Description	Unit
k_i	Specific cell growth rate constant	min^{-1}
$c_{\max i}$	Carrying capacity for cell growth	ml^{-1}
d_i	Cell death rate constant	$\text{nM}^{-1}\text{min}^{-1}$
k_{Ei}	Lysis protein synthesis rate constant	min^{-1}
d_{Ei}	Lysis protein decay rate constant	min^{-1}
k_{MEi}	Maximal rate of lysis gene transcription	nM min^{-1}
α_{MEi}	Sensitivity of lysis gene transcription to AHL	nM^{-1}
d_{MEi}	Lysis mRNA decay rate constant	min^{-1}
v_{MRi}	Transcription rate for a regulator	nM min^{-1}
d_{MRi}	Regulator mRNA decay rate constant	min^{-1}
k_{Ri}	Regulator synthesis rate constant	min^{-1}
d_{Ri}	Regulator decay rate constant	min^{-1}
v_{Ai}	AHL synthesis rate constant	nM min^{-1}
η_i	AHL diffusion rate constant across the cell membrane	min^{-1}
d_{Ai}	AHL intracellular decay rate constant	min^{-1}
d_{Aei}	AHL extracellular decay rate constant	min^{-1}
k_{Pi}	AHL/regulator binding rate constant	$\text{nM}^{-1}\text{min}^{-1}$
d_{Pi}	AHL/regulator dissociation rate constant	min^{-1}
k_{Qi}	AHL-regulator complex dimerization rate constant	$\text{nM}^{-1}\text{min}^{-1}$
d_{Qi}	(AHL-regulator) ₂ unbinding rate constant	min^{-1}

Table 5.4. Base values for the key parameters

Parameter	Description	Base value
k_i	Specific cell growth rate constant	0.02 min^{-1a}
$c_{\text{max}i}$	Carrying capacity for cell growth	0.05^b
β	Cooperativity of AHL effect	1.2 (101)
d_i	Cell death rate constant	$4 \times 10^{-5} \text{ (nM}^{-1} \text{ min}^{-1})$ (104) c
$k_{Ei}k_{MEi}/d_{MEi}$	Collective synthesis rate constant for a lysis protein	$20 \text{ (nM min}^{-1})^d$
d_{Ei}	Decay rate constant of a lysis protein	$0.02 \text{ (min}^{-1})^e$
η_i	Diffusion constant of AHLs	$0.5 \text{ (min}^{-1})$ (105) c
v_{Ai}	Synthesis rate constant of AHL	$50 \text{ (nM min}^{-1})^f$
α_{Ei}	Effecting factor for AHL	$0.068 \text{ (nM}^{-\beta})^g$
d_{Ai}	Decay rate constant of AHL in the cell	$0.02 \text{ (min}^{-1})^e$
d_{Aei}	Decay rate constant of AHL in the medium	$0.03 \text{ (min}^{-1})^h$

^a Approximately 1.5 doublings per hour.

^b The volume fraction of spheres tightly packed into a cubic space is about 0.5. In a liquid culture, a cell density of 10^{10} /mL corresponds to a volume fraction of about 0.01, assuming a cell size of 10^{-15} L.

^c Estimated based on the data from literature data.

^d This value corresponds to about 20 molecules/min; it is selected so that the dimensionless parameter $\kappa_{Ei} = 2$.

^e The degradation of AHLs and proteins inside the cell is assumed to be primarily due to dilution by cell growth. Actual degradation rate constants for proteins may be slightly larger due to proteolysis. A small increase in these parameters will have only minor effects on the system dynamics.

^f The value is based on a VAI synthesis rate constant of approximately 1 nM min^{-1} per nM of LuxI (106), and the assumption that the intracellular concentration of an AHL synthase is 50 nM.

^g This value is chosen so that the dimensionless parameter $\alpha_i = 500$.

^h This can be modulated by varying the medium Ph (107) or by applying enzymes (acylase or lactonase) that can degrade AHL (108, 109).

5.5 Materials and Methods

5.5.1 Plasmids

Plasmids used for this study are shown in figure 5.4. To construct placCcdBs (p15A origin, Kan^R), 96 base pairs between two *NstI* sites in the coding region of LacZ α -CcdB (pZErO-2) were deleted, and the resulting gene *lacZ α '-ccdB*, along with its upstream lac promoter, was cloned into pPROLar.A122 (BD Biosciences Clontech). p_{tet}LuxRLasI-

luxCcdA (SC101 origin, Cm^R) was constructed in several steps. First, the *lasI* gene along with its ribosome binding site was cloned from the *Pseudomonas aeruginosa* (PAO1) chromosome into plasmid pLuxR (110), where it was placed downstream of the *luxR* gene. Secondly, the *luxR-lasI* cassette was cloned into plasmid pPROTet.E132 (Clontech) to generate ptetLuxRLasI, where the cassette is under control of a P_{LtetO-1} promoter (91). Next, the *ccdA* gene was cloned from the F plasmid, PCR-fused with a P_{luxI} promoter from pluxGFPuv (110), and inserted into ptetLuxRLasI, in opposite direction from the P_{LtetO-1-lasR-lasI} cassette. Finally, the ColE1 replication origin of this plasmid was replaced with the SC101 origin, which was cloned from the repressilator plasmid (111). pLasRLuxI-*luxCcdBs* (p15A origin, Kan^R) was also constructed in several steps. First, the *lasR* gene was cloned from the *P. aeruginosa* (PAO1) chromosome into pPROLar.A122 (Clontech) placing it under control of the P_{lac/ara-1} promoter, to generate pLasR. Second, the *luxI* gene was cloned from plasmid pSND-1 (112) into pLasR where it was positioned directly downstream of the *lasR* gene, generating pLasRLuxI. Third, a pluxI-*lacZα'-ccdB* cassette was cloned from plasmid pluxCcdBs, which was derived from pluxCcdB (96) by removing 96 base pairs between two *NstI* sites (see above).

Plasmid ptetGFPuv(LVA) (ColE1 origin, Cm^R) was constructed by inserting an N-terminal portion of GFPuv amplified by polymerase chain reaction (PCR) with a primer including a *KpnI* site upstream of the start codon and a primer annealing to the internal *AvaII* site, and a C-terminal portion of GFP(LVA) amplified by PCR from pINV-4 (113) with a primer annealing to the internal *AvaII* site and a primer including

*Bam*HI downstream of the LVA tag into *Kpn*I and *Bam*HI digested pPROTet.E132 (BD Biosciences Clontech).

5.5.2 Strains, Growth conditions and Macroscale Data Acquisition

Top10F⁷ cells (Invitrogen) were used unless otherwise noted. For IPTG/AHL response tests in figure 5.2, we used 3OC6HSL (Sigma Aldrich) and 3OC12HSL synthesized by E. Toone (Department of Chemistry, Duke University), which were prepared and stored as Collins et al (110).

For the long-term cultures, pH-buffered TBK media (10 g tryptone and 7 g KCl per liter) were used. The media were buffered with 100 mM weak acids (PIPES was used for pH 6.2 and 6.6, and MOPS for pH 7.0), and pH was adjusted by adding 5 M KOH. Antibiotics (50 $\mu\text{g mL}^{-1}$ chloramphenicol and 50 $\mu\text{g mL}^{-1}$ kanamycin) and anhydrotetracycline were added. One-millimolar IPTG plus 0.05% Arabinoe was used to activate the circuit. Cultures were shaken in a 12 mL culture tube at 37 °C and 250 rpm. A starter culture of the predator cells or the prey cells was inoculated from a single colony and grown separately for at least 10 hours, and then diluted 1,000-fold into 4 mL of fresh medium. Measurement and dilution were done every eight or twelve hours. At the time points, 200 μl of the culture was transferred into a 96-well black clear bottom microplate and measured with a PerkinElmer VICTOR³ microplate reader (at 600 nm for absorbance, 405 nm excitation filter and 535 nm emission filter for fluorescence).

Then, after transferring the culture back from the microplate to the culture tube, a certain amount of the culture was substituted with an equal volume of the fresh sterile medium: 1 mL for 25% dilution, 2 mL for 50% dilution, and 3 mL for 75% dilution, respectively.

Genetic stability of the circuit after the long-term culture was examined by using the IPTG/AHL response tests as shown in figure 5.7. Predator and the prey cells were isolated from mixed cultures by selective plating: Top10F' (F' $\{lacI^q, Tn10(Tet^R)\}$, (ara-leu) 7697) can grow on an LB agar plate containing tetracycline, but not on an M9 minimal medium plate; in contrast, BW25113 can grow on the M9 plate, but not the LB-tetracycline agar plate.

5.5.3 Microchemostat Medium, Preculture Preparation and Growth Conditions

LBK medium contains 10g tryptone, 5g yeast extract, and 7g KCl per liter, and 100mM 3-(N-morpholino) propanesulfonic acid (MOPS). Medium pH (measured with Accumet pH Meter 925, Fischer Scientific) was adjusted by adding 5M KOH. LBK medium was used in all microchemostat experiments unless otherwise stated. Predator and prey populations were independently tested for circuit function according to the procedure mentioned above. 30 μ L glycerol stock solutions were created using the tested predator and prey cultures and were placed in a -80 °C freezer for long-term storage.

These ministocks were used to prepare precultures for subsequent microchemostat experiments.

Precultures were prepared by inoculating a 2ml sterile medium sample with 10 μ L of previously prepared mini-glycerol stock cell solution and shaking at 280rpm for \sim 9 hours at 37 °C (VWR bench top incubator, model 1575R). The precultures were then used to seed microchemostat reactors with \sim 20 cells/nL. To measure predator-prey circuit dynamics in the microchemostat, cells were grown in pH 7.0—buffered LBK medium. All microchemostat media were supplemented with 5g per liter bovine serum albumin as an antiadhesion adjuvant. The predator-prey circuit plasmids were maintained with 50 μ g/mL of kanamycin and 15 μ g/mL chloramphenicol. All experiments were performed within a microscope plexiglas incubator to control growth temperature at 37 °C.

5.6 Acknowledgements

We thank M. Elowitz for the repressilator plasmid, J. Leadbetter for *P. aeruginosa* chromosomal DNA, R. Weiss for plasmid pSND-1, R. S. Cox III and C. Ward for preliminary study and technical assistance, E. Toone and X. Chen for synthesizing 3OC12HSL. This work was supported by the Defense Advanced Research Projects Agency (DARPA), NIH, Packard Foundation, and the Howard Hughes Medical Institute.

Chapter 6

Bacterial Chemotaxis Chip

6.1 Introduction

6.1.1 Bacterial Chemotaxis

Bacterial chemotaxis is the directed movement of an organism toward environmental conditions it deems attractive and away from surroundings it finds repellent (114, 115). For bacteria, chemotaxis represents the most basic sensory organ that helps them find food (e.g. glucose) by swimming toward the highest concentration of food molecules or to flee from poisons (for example, phenol). The process of bacterial chemotaxis for model organisms such as *E. coli* is well understood.

Movement of flagellated bacteria such as *E. coli* can be characterized as a sequence of relatively straight smooth-swimming runs punctuated by intermittent tumbles that reorient the bacterium. When the cell's five to eight helical flagella rotate counterclockwise, they bundle together and propel the cell forward, effecting a run. Switching the rotational direction of some flagellar motors to clockwise disrupts the bundle and causes the cell to tumble. The length of each run varies from a fraction of a

second to minutes. Tumbles, on the other hand, only last for a fraction of a second albeit long enough to randomize the direction of the next run (114, 116).

Being only a few microns long, *E. coli* cells behave essentially as point sensors, unable to measure gradients by comparing head-to-tail concentration differences. Instead they possess a kind of memory that allows them to compare current and past chemical environments (117). The probability that a smooth-swimming cell will stop its run and tumble is dictated by the chemistry of its immediate surroundings compared to the chemistry it encountered a few seconds previously. The tendency to tumble is enhanced when the bacterium perceives conditions to be worsening; when the attractant concentrations decrease or repellent concentrations increase. Conversely, tumbling is suppressed and cells run longer when they detect that conditions are improving. Thus when a bacterium runs up a gradient of attractants or down a gradient of repellents, it tends to continue on its course (114).

Like quorum sensing, two families of proteins work in pair-wise fashion to mediate chemotaxis in *E. coli*. The first one, CheA, is a conglomeration of five different transmembrane receptors, which consist of an external sensing domain connected by hydrophobic spanning sequences to an autophosphorylating kinase domain in the cell's cytoplasm. Each receptor functions to detect a different class of attractant molecules: Tar detects aspartate, glutamate and maltose; Tsr detects serine; Trg detects ribose and galactose; Tap responds to dipeptides; and Aer is sensitive to oxygen (114, 118). The first

four receptors are collectively referred to as “methyl-accepting chemotaxis proteins” or MCPs (119).

The second of the two-component chemotaxis proteins, CheY, consists of response regulator proteins, and is activated by the transfer of phosphoryl groups from the kinase phosphohistidines to its own aspartic acid residues.

When stimulatory ligands interact with the external sensing domain of CheA (in the absence of repellents or presence of attractants), its receptors transmit a signal that increases CheA autophosphorelation. Increased CheA phosphorylation leads to an increase in the level of phosphorylated CheY. Phospho-CheY diffuses freely through the cell and when it encounters a flagellar motor, it binds to a flagellar protein called FliM. Phospho-CheY bound to FliM causes a change in the sense of flagellar rotation from counterclockwise to clockwise, throwing the flagellar bundle into disarray, which effects a tumbling event.

Chemotaxis is an important physiological mechanism that could be responsible for assigning commensal bacteria to their respective environments during host-specific associations (120-124). For example, the pathogen *Vibrio cholerae* depends on its chemotaxis to colonize intestinal tissues (125, 126) whereas strains of *Escherichia coli* that engender urinary tract infections exhibit defective chemotaxis (127). Although the mechanisms regulate chemotaxis have been studied to great molecular detail in model organisms such as *E. coli* (119, 128-133), relatively little is known concerning their physiological regulation in the life of an organism, and differences in the chemotactic systems among strains associated from different hosts. The ecological and clinical

significance of bacterial chemotaxis compels us to understand its physiological and genetic regulation.

6.1.2 Conventional Quantification of Bacterial Chemotaxis

Conventional methods employed to study bacterial chemotaxis include the capillary method, swarm plates, and photomicrography. In the capillary method (115, 134), a capillary containing an attractant is immersed in a bacterial culture.

After a fixed period (usually 45 to 90 minutes) it is carefully retrieved and the number of bacteria that have migrated into the capillary are quantified using various microbiological techniques, key among them, serial dilution, plating, followed by counting on agar plates.

A convenient design for this approach involves a Palleroni chamber (134) (figure 6.1).

Whereas multiple capillaries could be run in parallel and collected at different time points using a Palleroni chamber, the time resolution is on the order of tens of minutes, and data acquisition is at best a long, hands-on, tedious process.

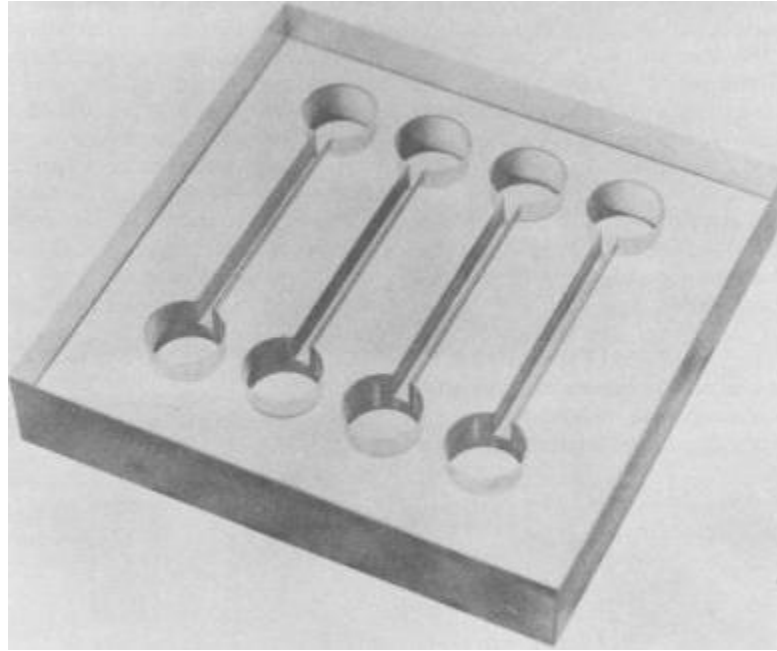


Figure 6.1. The Palleroni Chamber: four chambers are excavated in a square Lucite plate measuring 5.5 cm per side and 1 cm in thickness. Each of the chambers consists of two cylindrical compartments measuring 7 mm in diameter and 5 mm in height, linked by a channel 24 mm long, 2 mm wide and 2 mm deep. After appropriate sterilization, a suspension of motile cells is pipetted to fill the compartments and the channel of each chamber. To quantify chemotaxis, a capillary full of attractant is placed into the channel of a bacteria-laden chamber (134).

A simpler alternative indicator of chemotaxis involves the use of swarm plates (135-137). Bacteria are plated at the center of a low density (25%) agar plate containing a metabolizable attractant. They migrate outward from the central inoculation point in response to a gradient in attractant concentration set up by the bacteria themselves as they consume the attractant, forming concentric ring pattern. The size (diameter) of the observed ring is used to gauge the extent of chemotaxis. While the swarm plate permits a continuous observation of the chemotactic response, it is generally considered only a qualitative measure of chemotaxis. It is also limited in the fact that the response depends not only on chemotaxis but also metabolism of the attractant.

Micrographic methods represent a different approach to analyzing bacterial chemotaxis by for instance facilitating tracking of the chemotactic behavior of single free-swimming cells (138) and quantifying changes in run/tumble behaviors or direction of flagella rotation in attractant solutions of various concentrations (139). Microfluidic schemes have also been used to create chemical gradients (140, 141) for chemotaxis studies, measuring the overall numbers of cells without characterizing the behavior of individual cells.

The chemotaxis machinery can be probed genetically by taking it apart (e.g., deletion of receptors) and observing the effect on the run and tumble behavior or rotation of flagella. Nevertheless, corresponding physiological analysis (e.g., effects of nutrients known to upregulate or downregulate the components of the chemotactic machinery) is relatively lacking, in part because measurements from current methods are either too

short in duration (in the case of most micrographic or microfluidic methods) or last too long (swarm plate experiments), due to difficulties in manipulating or controlling the culture conditions or nutrient state of the bacteria.

The microchemostat (chapter 3), a device which allows long-term (several weeks) micrographic, non-invasive observation, maintenance, and manipulation of *E. coli* bacteria under a matrix of culture conditions, will allow detailed analysis of the physiological regulation of chemotactic behavior. This device may also be suitable for rapid analysis of chemotactic behavior. This chapter, which is coauthored by Jeffrey Ram, describes how the microchemostat could be modified to perform *de novo* studies of chemotaxis with unprecedented resolution and accuracy.

6.2 Microfluidic Quantification of Chemotaxis

6.2.1 Microfluidic Chemotaxis Interface Chip

The chemotaxis quantification interface chip examines the chemotactic response of different strains of *E. coli* to various attractants.

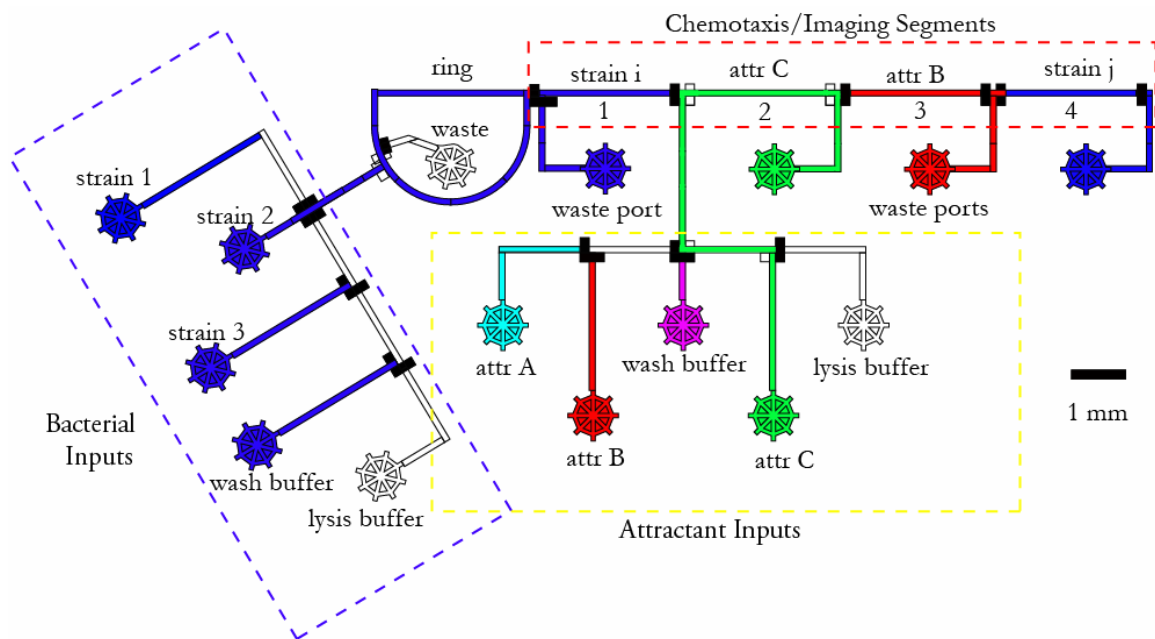


Figure 6.2. Schematic diagram showing the main components of the chemotaxis interface module. The ‘wheel’-shaped structures represent input/output ports for loading or draining cells and solutions. The segments have rectangular cross-sections with a width of 100 μm and height of 10 μm . The blue dashed rectangular boundary on the left encloses one lysis buffer, one wash buffer, and three bacteria culture input ports. The yellow dashed boundary at the bottom encloses one lysis buffer, one wash buffer and three attractant input ports. The semicircular blue ring is a temporary storage of bacterial cells. The red dashed boundary at the top encloses four individually addressable chemotaxis/imaging segments. For example, segment two is shown being flushed by attractant C from port (attr C).

The blue dashed rectangular boundary on the left encloses five input ports for lysis buffer, wash buffer, and up to three different bacteria cultures. The five ports within the adjacent yellow dashed boundary at the bottom are for input of a lysis buffer, a wash buffer and three attractant solutions.

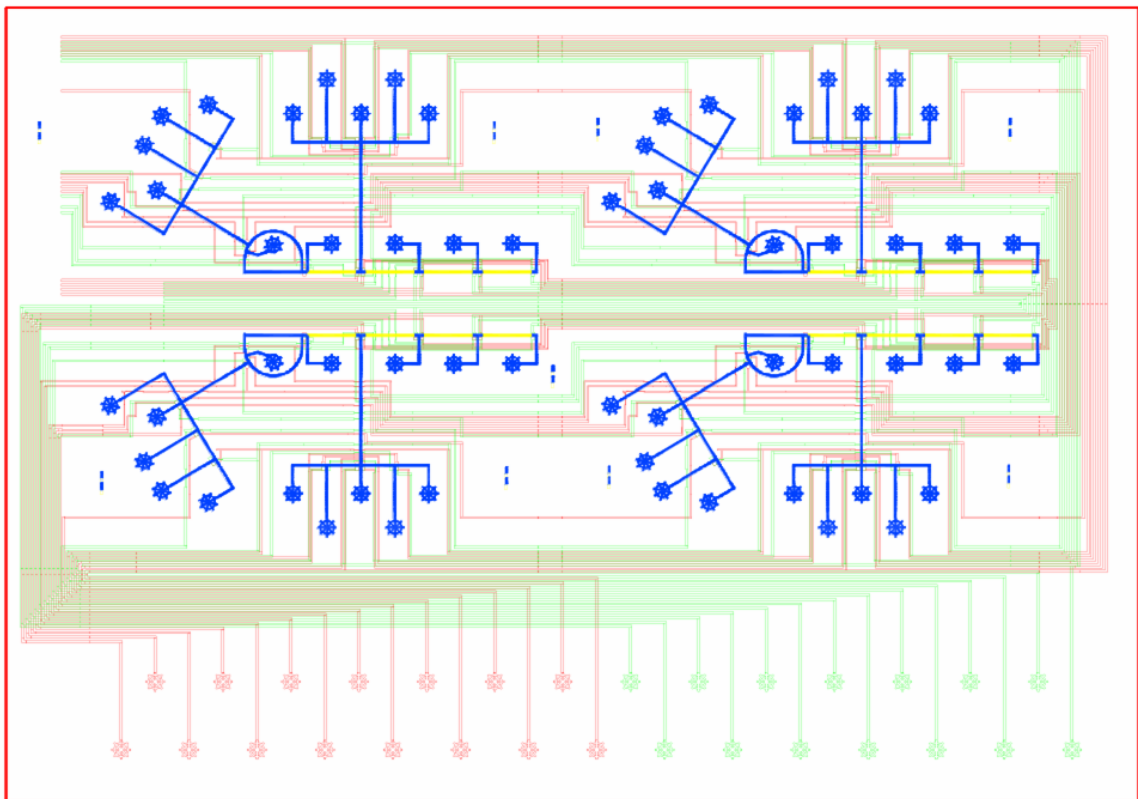


Figure 6.3. Schematic of the entire chemotaxis chip with four chemotaxis modules (blue and yellow segments) as well as the corresponding control lines (green and red). The width of the chip is 5 cm.

Specific bacterial culture or attractant solutions from any of these input ports can be loaded into any of the four segments enclosed by the red dashed rectangular boundary in a mutually exclusive fashion. In addition bacterial culture can be loaded into the ring section. Usually, prior to loading cells or attractant, the respective section (ring or segment) can be ‘sterilized’ by flushing with lysis buffer for 30 seconds followed by wash buffer for 60 seconds. Each chip contained four such chemotaxis modules (figure 6.3).

6.2.2 Experimental Procedure

To observe chemotaxis of a cell strain, two adjacent chambers of a chemotaxis module (ring section, any of the four segments, or their combinations) are loaded, one with a specific cell strain culture and the other with an attractant or control solution. The (bacterial or attractant) solutions in each chamber are initially physically isolated using peristaltic valves. Under these conditions, cell density readings can be performed in each segment, to determine the initial densities in the cell-bearing chamber and to ascertain that the attractant chamber is void of any cells. Next, the valves separating the two chambers are opened, which removes the boundary between the cells and the attractant solution. By analyzing the number of cells that migrate into the attractant chamber as a function of time, we were able to quantify the chemotactic response of the cell strain to the attractant.

6.3 Results

6.3.1 Observation of Chemotaxis on a Chip

We measured the chemotactic responses of various strains of *E. coli* to two key attractants; ribose (0.1 mM) and aspartate (0.1 mM), under different conditions of growth. Typical results showing the chemotactic response of strain K12 (figures 6.4 and 6.5), in which approximately equal densities of cells were initially loaded into segments 1 and 4, and then either control (data points 1 to 25, 0 to ~25 minutes) or attractant (data points 26 to 50, ~25 to 50 minutes) solution was loaded into segments 2 and 3. The valves separating all segments were closed for the first five data points in each experimental test, and then at trial 6 the valves separating segment 1 from 2 and 3 from 4 were opened (as illustrated in figure 6.2) for the next 20 data points (recorded at approximately 1 min intervals). Between data points 25 and 26, cells and solution were washed out of all chambers and then cells, at approximately the same density as before, were introduced into segments 1 and 4 and attractant solutions were loaded into segments 2 (aspartate medium) and 3 (serine medium). Figure 6.4 shows the processed images of the source cells in segment 1 and of cells accumulated in segment 2 in response to control and aspartate-containing media 15 min after opening the valve separating the attractant from the source cells. Data in figure 6.5 are cell counts from images recorded at approximately the midpoints of segments 2 and 3.

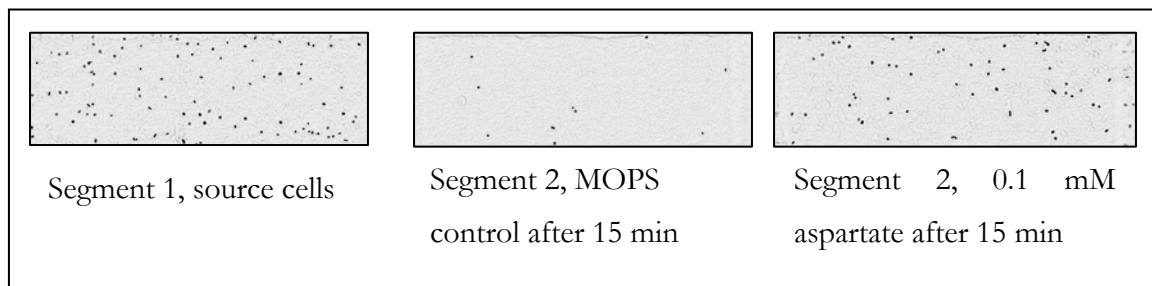


Figure 6.4. Matlab processed images of bacterial cells. Calibration = 40 μm .

As illustrated in figure 6.5 and observed in virtually all experiments with motile cells, the number of cells in a segment containing attractant (aspartate or serine) increased more than when tested with the control solution lacking attractant, thereby demonstrating the occurrence of chemotaxis. The cells responded in less than a minute and, in the case of aspartate, reached a plateau in about 10 minutes. In most experiments, the response of K12 to aspartate was larger and often more rapid than to that of serine, as illustrated here; however, differences in cell density of the source cells between segments 1 and 4 and also in the relative distance of the images in segments 2 and 3 from their respective cell sources could account for some of the quantitative differences in this experiment.

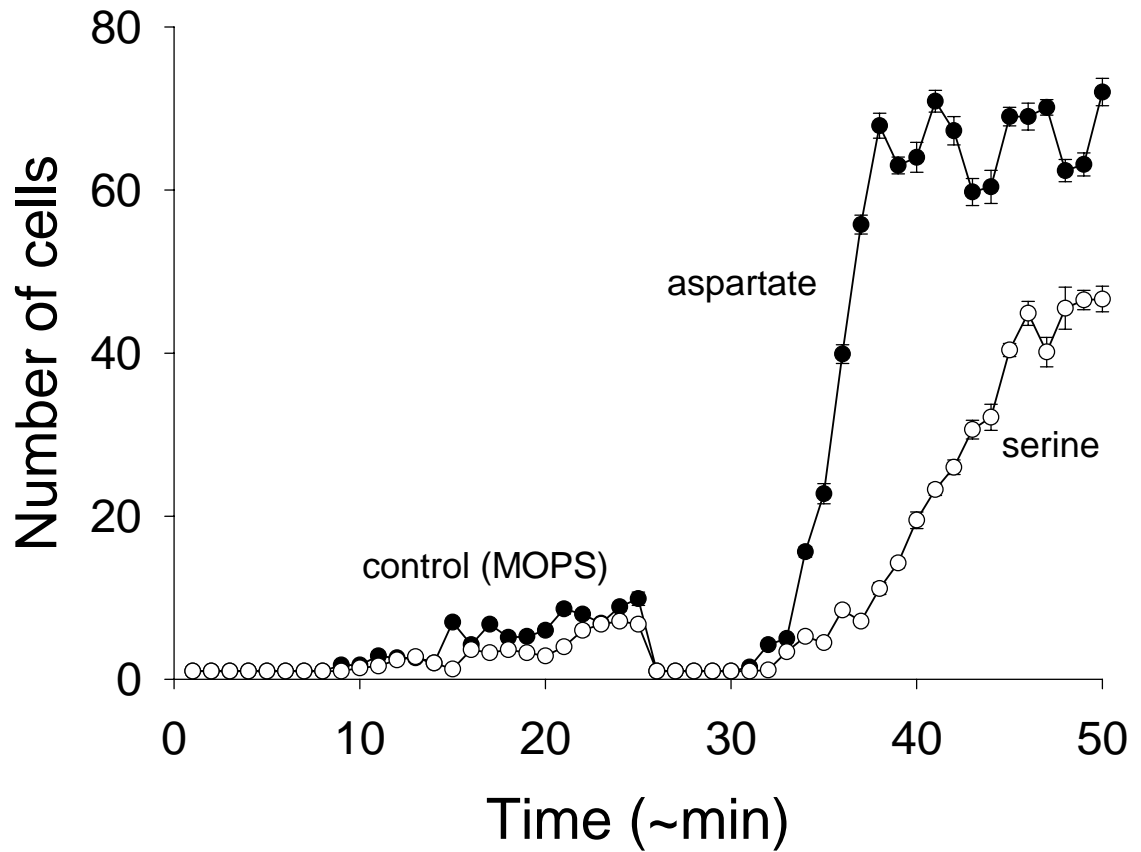


Figure 6.5. Density of cells in the imaged section of segment 2 (aspartate) and 3 (serine). For both segments, cells were first tested with control medium (trials 1 to 25), and then with 0.1 mM of the indicated attractant in the segment.

6.3.2 Long-Term Chemotaxis Response

Typical results of a long-term representative experiment involving the *E. coli* strain 1529 are illustrated in figures 6.6, in which cells were initially loaded into the ring section (see figure 6.2) and then control, aspartate (0.1 mM) or serine (0.1 mM) solution was loaded into segments 1 and 2 (combined).

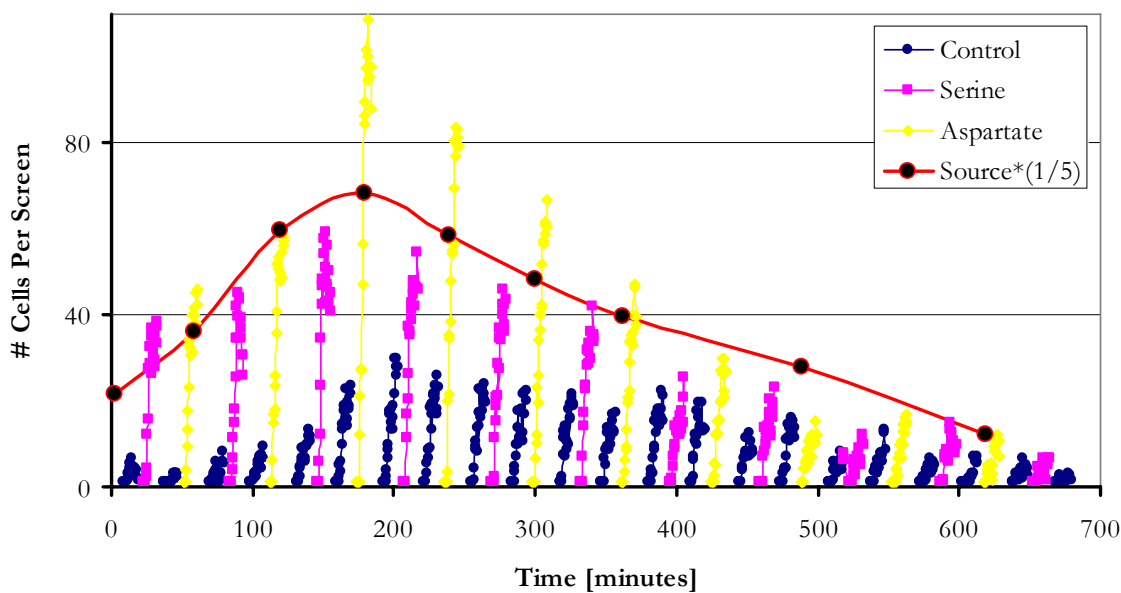


Figure 6.6. Response of cells to 0.1 mM of attractant (serine or aspartate) and control solutions. In this experiment, the source cells are placed in ring section and the attractants were placed in segments 1 and 2 (combined). The above data were generated from a location in the first segment, $\sim 200 \mu\text{m}$ away from the source cells.

The chemotactic response was retested over a long period of time (over 10 hours) using the same cells and attractant solutions. Although there was greater accumulation of cells in attractant solutions compared to control medium in almost all experiments, the magnitude of the chemotactic response to attractant varied over time: the absolute difference in the migrant cells or the rate at which they accumulated in the attractant chambers first increased and then decreased. Figure 6.7 shows the first iterative response of the bacteria. Figure 6.7 shows the first iteration response to aspartate, serine or control.

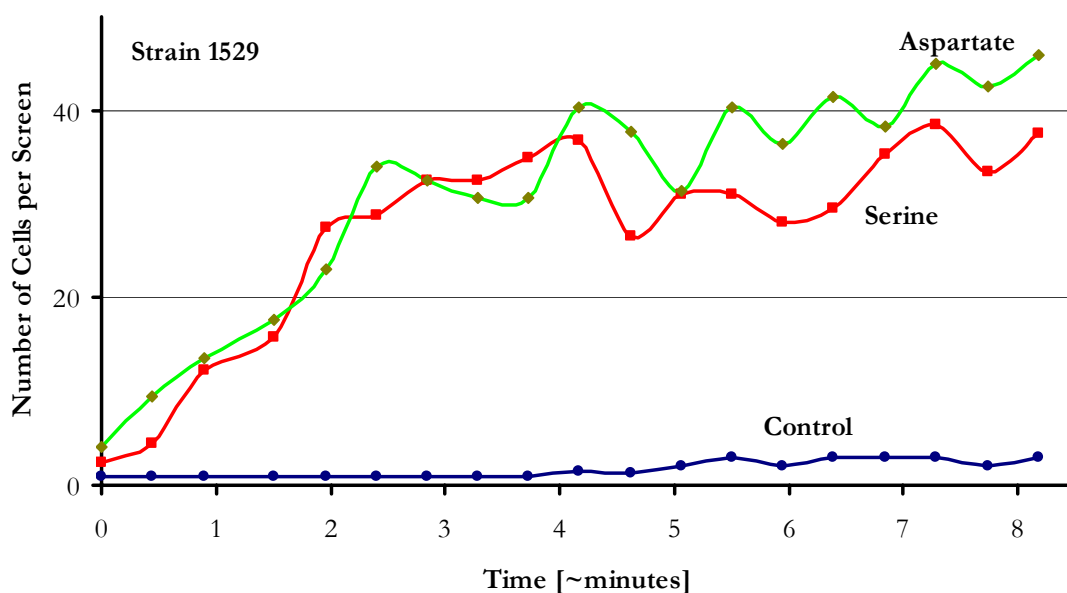


Figure 6.7. Zoom in on the first response iteration showing the response of cells to 0.1 mM of attractant (serine or aspartate) and control solutions.

In this experiment, the source cell density was measured periodically throughout the experiment, and it was observed that the density of source cells increases in the apparatus for several hours and subsequently decreases. The variation in cell density is presumably taking place in the tygon tubing in which cells are held prior to loading into the chip. Perhaps gravity gradually sets up a cell density gradient in the tygon tubing such that the density that is fed into the chip increases (as the gradient forms) and then decreases over time. Therefore the changes in the response observed over time could be due to the variations in the source cell density. Other possible sources of variation include the cell motility and degradation of the dissolved attractants.

To get a cell density-independent interpretation of the data, we normalized the observed cell density by the source cell density, using only the maximum density for each response to yield figure 6.8.

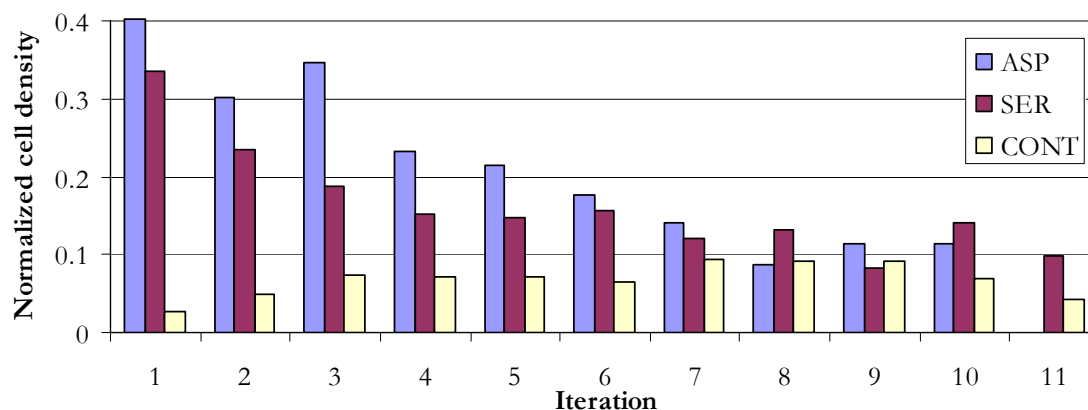


Figure 6.8. A monotonic decrease in the normalized response of bacteria to serine and aspartate over time.

The monotonic decrease in the response magnitude over time suggests one of two things: either the physiological state of the bacteria is changing over time, affecting their ability to chemotax (motility), or the attractants themselves degrade over time and lose their chemotactic flavor. The decrease in the attractant response, relative to the control response over time further underscores the weakening of the chemotactic force.

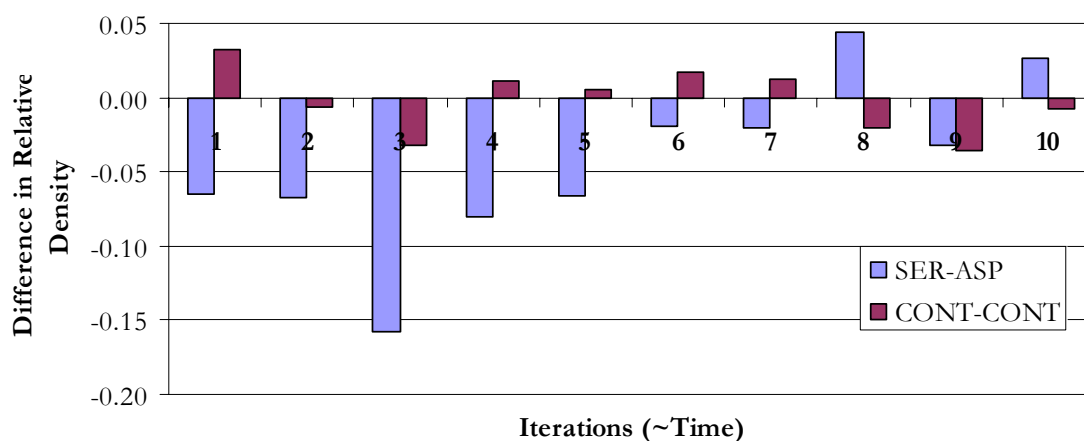


Figure 6.9. Graph showing the difference between the serine and aspartate response of strain 1529.

Control response measurements were made after each serine or aspartate reading, such that there were twice as many control measurements as there were for serine or aspartate. Therefore, we plotted the difference between serine and aspartate chemotaxis using the difference between consecutive control responses as a control (figure 6.9). The results show that this strain has a stronger chemotactic response for aspartate as compared to serine. The “control-control” internal controls set the sensitivity (noise

level) of the measurement. Moreover the preference of aspartate over serine was highest when the cell density of the incoming cells was at its peak.

6.4 Discussion and Conclusion

The experiments showed clearly that bacterial chemotaxis can be observed in microfluidic devices constructed and operated according to the principles of multi-layer soft lithography. Bacteria migrated rapidly and to high levels into attractant media compared to control media. Computer-controlled sequencing of experiments and image analysis enabled rapid demonstration of chemotaxis within minutes of loading bacteria into the microfluidics chip. The system allows simultaneous video recording of cell motility and thereby makes measurement of movements underlying the chemotactic accumulation of cells accessible. Almost certainly, one could easily model the relationship of the “run and tumble” movements and their temporary suppression by attractant to the movement of the migrating bacteria in response to attractant.

The changes in chemotactic responses with time in these experiments represent both a problem and an opportunity for understanding the role of chemotaxis in the life of the organism. It is a problem if one wishes to compare the chemotaxis of specific strains of *E. coli* since the instantaneous result that one observes is not a fixed property of the strain but likely to be dependent on its physiological state. However, it is an opportunity because it demonstrates that analysis of chemotaxis as the cells change physiological state may be possible.

In figure 6.8, the monotonic decrease in the normalized response magnitude over time suggests one of two things: either the physiological state of the bacteria is changing over time, affecting their ability to chemotax (motility), or the attractants themselves degrade over time and lose their chemotactic flavor. The decrease in the attractant response, relative to the control response over time further underscores the weakening of the chemotactic force.

Controlling the density and growth of bacteria in the apparatus would also seem to be a prerequisite for comparing the chemotactic responses of different *E. coli* strains, one of the original goals of these experiments. In figure 6.9, the preference of aspartate over serine seems to be dependent on the initial cell density.

In future experiments, it would be very useful for understanding the role of chemotaxis in the life of the organism if the effects of specific manipulations of physiological state on chemotaxis could be measured. For example, it is known from microarray experiments that when *E. coli* are shifted to a diet in which propionate is the only carbon source that the expression of genes mediating chemotaxis and flagellar biosynthesis are upregulated up to 7-fold (142). One would presume that measurable changes in motility and chemotaxis would result; however, behavioral correlations to these changes in gene expression have apparently not been determined. In other cases, engineered changes in the expression of specific modified chemotactic components have been created but changes in chemotaxis could not be detected by the relatively inefficient swarm plate and capillary chemotaxis measurements (119). The detailed behavioral

analysis made possible by microfluidic devices may be able to provide the requisite analysis.

In order to provide better control of the density and growth of bacteria whose motility and chemotaxis are being analyzed, it would therefore be desirable to culture the bacteria *in situ* (right in the chip), comparable to the microchemostat designed by Balagaddé et al. (6) and to provide access for cells in the microchemostat to chemotaxis test segments.

6.5 Materials and Methods

Cells and solutions: *E. coli* were grown from a standard laboratory strain (K12) or from stock cultures originally isolated by the Ram laboratory from fecal samples of various animals and humans and stored as frozen stocks in 14% glycerol at -80°C . Cultures were grown overnight in LB medium that had been inoculated with a scraping from the frozen stock. Overnight cultures were then reinoculated (5 uL/5 mL) into various media and grown for a few hours to reach midgrowth phase prior to loading into the microfluidics apparatus. If overnight cultures were not inoculated promptly (i.e., in the morning) for re-growth, they were usually stored for up to 24 hr at 4°C until use.

In some experiments “conditioned medium” was used as the chemotaxis buffer. To prepare conditioned medium (CLB), LB medium was inoculated with *E. coli* and incubated at 37°C with shaking at 280 rpm. Upon reaching stationary phase, the culture

was cold filtered using a 0.2 μm filter, pH adjusted and autoclaved. The supernatant was reinoculated with *E. coli* and grown to stationary phase. This process of inoculation, growth and sterilization was repeated multiple times until the freshly inoculated supernatant was incapable of supporting any *E. coli* growth. At this point, the medium was filter sterilized for the last time, pH adjusted, autoclaved and stored at room temperature. Conditioned medium is considered to be a medium rich in all trace elements but void of all carbon sources (including metabolizable attractants). This notion is supported by the observation that CLB medium did not support any microbial growth except when supplemented with glucose. For this reason, it was sometimes supplemented with glucose and used to grow cells for chemotaxis experiments.

In some experiments, we used “Conditioned LB,” (CLB) supplemented with glucose (CLB plus 5 mg/mL BSA and 10 μl /mL 20% glucose) or glucose-supplemented-MOPs medium (MOPS medium contains, per mL, 0.1 mL of 10X MOPs medium [Teknova], 1 μL 0.132 M K_2HPO_4 , and 5 mg of BSA). The attractant and other solutions were:

Control or wash buffer: MOPs minimal medium (see previous paragraph), used without glucose.

Aspartate: 0.1 mM aspartate in MOPs medium without glucose

Serine: 0.1 mM serine in MOPs minimal medium without glucose

Lysis buffer: B-PER, from Pierce, Rockford, IL

All media and buffers used in the chip were supplemented with 5 mg/mL bovine serum albumin (source) as an anti adhesion adjuvant.

All the solutions loaded onto the chip were kept in tygon tubing and interfaced to the chip using stainless-steel pins.

APPENDIX A: CHEMOSTAT MATHEMATICAL PARAMETERS

QUANTITY	SYMBOL	UNITS
Number of cells in reactor	n	<i>cells</i>
Size of inoculum	n_0	<i>cells</i>
Carrying capacity of growth environment	N_∞	<i>cells</i>
Cell density	ρ	<i>cells length⁻³</i>
Cell density at maximum carrying capacity	ρ_{\max}	<i>cells length⁻³</i>
Volume of reactor	V	<i>length³</i>
Time	t	<i>time</i>
Limiting substrate concentration in reactor	S	<i>mass length⁻³</i>
Limiting substrate concentration in reservoir	S^0	<i>mass length⁻³</i>
Specific growth rate	μ	<i>time⁻¹</i>
Time interval between two consecutive discretized dilution events	T	<i>time</i>
Fraction of cells removed during each discretized dilution event	F	<i>dimensionless</i>

APPENDIX B: FABRICATION PROTOCOLS

Fabrication Protocol: Microchemostat device

3" silicon wafer substrate

Mold Fabrication:

I. Push-up control molds

Spin SU8 2025: 3000 rpm x 45 seconds / 15 second ramp up

film thickness = 22 microns

Pre-Exposure Bake: contact bake hotplate

3 min x 65° C / 5 min x 95° C

Expose Wafer: 15 s at 7 mW/cm²

Post-Exposure Bake: 5 min x 65° C / 15 min x 95° C

Develop: 100 % Shipley SU8 Nanodeveloper

rinse with fresh developer

dry under nitrogen

II. Push-down control molds

Spin SU8 2050: 3000 rpm x 45 seconds / 15 second ramp up

film thickness = 50 microns

Pre-Exposure Bake: contact bake hotplate

3 min x 65° C / 5 min x 95° C

Expose Wafer: 15 s at 7 mW/cm²

Post-Exposure Bake: 5 min x 65° C / 15 min x 95° C

Develop: 100 % Shipley SU8 Nanodeveloper

rinse with fresh developer

dry under nitrogen

III. Flow Hybrid Mold

SU8-template

Spin SU8 2010: 3000 rpm x 60 seconds / 15 second ramp up

film thickness = 9 microns

Pre-Exposure Bake: contact bake hotplate

1 min x 65° C / 2 min x 95° C

Expose Wafer: 15 s at 7 mW/cm²

Post-Exposure Bake: 1 min x 65° C / 2 min x 95° C

Develop: 100 % Shipley SU8 Nanodeveloper

rinse with fresh developer

dry under nitrogen

Hard Bake: 1 hour 200° C

Ma-p1215 rounded geometry

Priming: HDMS vapor 1 min in tuperware container (STP)

Spin ma-p1275 positive tone resist: 2000 rpm x 60 s / 10 s ramp

Film thickness = 10 microns

Soft Bake: contact bake hotplate

65° C x 120 s / 115° C x 120 s / 65° C x 120 s

Expose Wafer: define channel structure

30 s at 7 mW/cm²

Develop: 3:1 dilution of Shipley 2401 developer

rinse DI H₂O

dry under nitrogen

Reflow: contact hotplate

115° C x 15 minutes

IV. MSL Fabrication

Priming: all molds

TMCS vapor 5 min in tuperware container (STP)

Cast Thick Layer: combine 5:1 GE 615 RTV (36 g A: 7 g B)

199

mix in hybrid mixer: 2 min mix / 2 min degas

36 g onto flow mold (petri dish lined with Al foil)

Spin Flow Layer 1: combine 20:1 GE 615 RTV (20 g A: 1 g B)

mix hybrid mixer: 2 min mix / 2 min degas

dispense 5 mL on flow layer

2300 rpm x 60 s / 15 s ramp

film thickness = 18 microns

1st Cure Thick Layer: convection oven

80 °C for 60 min

1st Cure Flow Layer: convection oven

80 °C for 60 min

Punching push up control input holes: peel thick layer from mold

punch control input holes

align to spin-coated and cured flow layer mold

bake in convection oven

80 C x 60 min

Spin push-down control layer: combine 20:1 GE 615 RTV (20 g A: 1 g B)

mix hybrid mixer: 2 min mix / 2 min degas

dispense 5 mL on flow layer

1800 rpm x 30 s / 15 s ramp

film thickness = 28 microns

1st cure push-up control Layer: convection oven

80 °C x 60 min

Control/flow/control bonding: peel thick/flow bonded layer from mold

take care to not rip membranes

punch flow input and output port holes

align to spin-coated and cured push-up control layer mold

ensure no air bubbles under membranes

ensure no collapsed valves

bake in convection oven

80 C x 60 min

Spin blank layer: combine 30:1 GE 615 RTV (60 g A: 2 g B)

mix hybrid mixer: 2 min mix / 2 min degas

dispense 5 mL clean glass substrate

2300 rpm x 60 s / 15 s ramp

film thickness = 18 microns

1st Cure Blank Layer: convection oven

80 C x 60 min

Control/flow/control/blank bonding: peel control 1/flow/control 2 bonded

layer from mold

take care to not rip membranes

punch control 2 (push-up) input port holes

align to spin-coated and cured blank mold

ensure no air bubbles under membranes

ensure no collapsed valves

bake in convection oven

80 C x 3 hr

* spin parameters need to be optimized for each batch.

APPENDIX C: MATLAB SCRIPT FOR IMAGE PROCESSING

```
% script 1: Determining the region of interest

% This is an interactive routine is performed once at the beginning
% of each experiment for each imaging location to determine appropriate values for the
% region of interest

%Initial values for the Region Of Interest (roi) within the image

roi = [11 265 50 455 400];    %[angle, xo, yo, delta_x, delta_y]
% rotation angle is the angle through which the image is rotated, xo & y0 are the top left
% coordinates of the region of interest in the rotated image delta_x and delta_y are the
width
% and height of the image

% rotate and crop the image according to roi
box1 = imcrop(imrotate(fig1, roi(1), 'nearest','crop'), [roi(2) roi(3) roi(4) roi(5)]);
figure, imshow(box1);

% script 2: process phase-contrast image set

a = 8;          % specify number of images in image set
e = 0.01;      % specify image thresholding factor (values range from 0 to 1) and depend on
camera lighting conditions
```

```

d = 10;          % specify image multiplication factor (values range from 5 to 20)
n = log2(a);
gb = a;         % store the set size in gb

% Store set of a images (a=8) in 4 dimensional array, A
for seq = 1:a
    A(:,:,:,seq) = imread(strcat(picdirect,'\OR',num2str(seq),'.PNG'));
    pix(seq) = mean(mean(A(:,:,:,seq))); % store mean pixel value of each image in pix
end

% determine the image with the lowest contrast
min = 1;
for mint= 1:8
    if(pix(mint) < pix(min))
        min = mint;
    end
end

% Normalize image set and extract region of interest
for q = 1:a
    emp(q) = pix(q)/pix(min); % get normalization factor
    Q(:,:,:,q) = imdivide(A(:,:,:,q),emp(q)); % normalize image
    B(:,:,:,q) = imcrop( imrotate( Q(:,:,:,q), roi(1), 'nearest','crop'), [roi(2) roi(3) roi(4) roi(5)] );
    B2(:,:,:,q) = B(:,:,:,q);
end

```

```
end
```

```
% average image set and store the average image as E
```

```
if (n>=2)
```

```
    for r=1:(n-1)
```

```
        b = a/2;
```

```
        for s=1:b
```

```
            B(:,:,s) = imlincomb(.5,B(:,:,s),.5,B(:,:,s+b));
```

```
        end
```

```
        a = a/2;
```

```
    end
```

```
end
```

```
if(n>=1)
```

```
    E = imlincomb(.5,B(:,:,1),.5,B(:,:,2));
```

```
end
```

```
% subtract each image from the average, threshold and convert to binary
```

```
for c = 1:gb
```

```
    F(:,:,c) = immultiply((imsubtract(E,B2(:,:,c))),d); % subtract image from background
```

```
    H = filter2(fspecial('average',4),F(:,:,c))/65535;
```

```
    J = imadjust(H,[e 1], [0 1]); % threshold the image
```

```
    K = graythresh(J);
```

```
    L(:,:,c) = im2bw(J,K); % convert image to binary
```

```
    [labeled,nCells(c)] = bwlabel(L(:,:,c),8); % count # bright particles
```

```

fprintf(fidx, '%g \t', nCells(c));           % Record the bright particles on a file
end

aver = mean(nCells(1:gb));   % determine average cell count
fprintf(fidx, '%g \t', aver); % record average cell count on file

% script 3: process fluorescent image set

gf = af; % number of fluorescence images in this set
nf = log2(af);

mult = 10; % specify fluorescent image multiplication factor (usually 10)
divi = 2; % specify fluorescent image division factor (usually 1)
sizF = 4; % filtering scalar (usually 3), controls the sharpness of the extracted blobs
sizdisk=3; % approximage disk size of particles to be counted, a small sizdisk value excludes
counting of large blobs

% read the fluorescent images into the program, then crop them according to roi. The
images have a file

% name structure that looks like: picdirect\F1.PNG
for qf = 1:af
    AF(:,:,,qf) = imread(strcat(picdirect, '\F', num2str(qf), '.PNG'));
    BF(:,:,,qf) = imcrop(imrotate( AF(:,:,,qf), roi(1), 'nearest', 'crop'),
[roi(2),roi(3),roi(4),roi(5)]);
    B2F(:,:,,qf) = BF(:,:,,qf);

```

end

% count the number of particles in each image

for cf = 1:gf

FF(:,:,cf) = filter2(fspecial('average',sizF),B2F(:,:,cf))/65535;

background = imopen(FF(:,:,cf), strel('disk', sizdisk)); % determine image background

FK = imsubtract(FF(:,:,cf), background); % subtract background from image

FKB = immultiply(FK,mult);

FK2 = graythresh(FKB/divi);

LF(:,:,cf) = im2bw(FKB,FK2); % convert image to binary

[labeled,nCellsf(cf)] = bwlabel(LF(:,:,cf),8); % count number of fluorescent blobs

fprintf(fidx, '%g \t',nCellsf(cf)); % record number of fluorescent particles

% store sample processed images if necessary

imwrite(LF(:,:,cf),strcat(picdirect,'LF',num2str(cf),'.PNG'));

imwrite(FF(:,:,cf),strcat(picdirect,'Ofn',num2str(cf),'.PNG'));

end

averf3 = mean(nCellsf(1:gf)); %average fluorescent cell count

fprintf(fidx, '%g \t \t', averf3); %store the average fluorescent cell count

Bibliography

1. Manz A, Eijkel JCT. Miniaturization and chip technology. What can we expect? *Pure and Applied Chemistry* 2001;73(10):1555-1561.
2. El-Ali J, Sorger PK, Jensen KF. Cells on chips. *Nature* 2006;442(7101):403-411.
3. Hansen C, Quake SR. Microfluidics in structural biology: smaller, faster, better. *Current Opinion in Structural Biology* 2003;13(5):538-544.
4. Unger MA, Chou HP, Thorsen T, Scherer A, Quake SR. Monolithic microfabricated valves and pumps by multilayer soft lithography. *Science* 2000;288(5463):113-116.
5. You L, Cox RS, Weiss R, Arnold FH. Programmed population control by cell-cell communication and regulated killing. *Nature* 2004;428(6985):868-871.
6. Balagadde FK, You LC, Hansen CL, Arnold FH, Quake SR. Long-term monitoring of bacteria undergoing programmed population control in a microchemostat. *Science* 2005;309(5731):137-140.
7. Sprinzak D, Elowitz MB. Reconstruction of genetic circuits. *Nature* 2005;438(7067):443-448.
8. Chin JW. Programming and engineering biological networks. *Current Opinion in Structural Biology* 2006;16(4):551-556.
9. Chin JW. Modular approaches to expanding the functions of living matter. *Nature Chemical Biology* 2006;2(6):304-311.
10. Desai MM, Fisher DS, Murray AW. The speed of evolution and maintenance of variation in asexual populations. *Current Biology* 2007;17(5):385-394.

11. Jannasch HW, Mateles RI. Experimental Bacterial Ecology Studied in Continuous Culture. In: Rose AH, Tempest DW, editors. *Advances in Microbial Physiology*. London: Academic Press; 1974. p. 165-212.
12. Novick A, Szilard L. Description of the Chemostat. *Science* 1950;112(2920):715-716.
13. Rotman B. A Simplified Device for Continuous Growth of Microorganisms. *Journal of Bacteriology* 1955;70(4):485-486.
14. Spicer CC. The Theory of Bacterial Constant Growth Apparatus. *Biometrics* 1955;11(2):225-230.
15. Herbert D, Elsworth R, Telling RC. The Continuous Culture of Bacteria - a Theoretical and Experimental Study. *Journal of General Microbiology* 1956;14(3):601-622.
16. Herbert D. Continuous Culture of Bacteria. *Journal of General Microbiology* 1956;15(1):R4-R4.
17. Herbert D. Continuous Culture of Bacteria - Principles and Applications. *Chemistry & Industry* 1958(13):381-381.
18. Monod J. La Technique De Culture Continue Theorie Et Applications. *Annales De L Institut Pasteur* 1950;79(4):390-410.
19. Dykhuizen DE. Experimental Studies of Natural-Selection in Bacteria. *Annual Review of Ecology and Systematics* 1990;21:373-398.
20. Fox MS. Mutation Rates of Bacteria in Steady State Populations. *The Journal of General Physiology* 1955;39:267-278.

21. Smith HL, Waltman P. The Theory of the Chemostat - Dynamics of Microbial Competition. 1 ed. Cambridge: Press Syndicate of the University of Cambridge; 1995.
22. Novick A. Growth Of Bacteria. Annual Review of Microbiology 1955;9:97-110.
23. Pilyugin SS, Waltman P. The simple chemostat with wall growth. Siam Journal on Applied Mathematics 1999;59(5):1552-1572.
24. DeLisa MP, Valdes JJ, Bentley WE. Mapping stress-induced changes in autoinducer AI-2 production in chemostat-cultivated Escherichia coli K-12. Journal of Bacteriology 2001;183(9):2918-2928.
25. Shuler ML, F. K. In: Guerrieri P, editor. Bioprocess Engineering: Basic Concepts. 2nd ed. Upper Saddle River: Prentice Hall PTR; 2002. p. 155-200.
26. Maresova H, Stepanek V, Kyslik P. A chemostat culture as a tool for the improvement of a recombinant E. coli strain over-producing penicillin G acylase. Biotechnology and Bioengineering 2001;75(1):46-52.
27. Nielson J, Villadsen J, Liden G. Strain Improvement. In: Bioreaction Engineering Principles. 2nd ed. New York: Kluwer Academic/Plenum Publishers; 2003. p. 42-45.
28. Parekh S, Vinci VA, Strobel RJ. Improvement of microbial strains and fermentation processes. Applied Microbiology and Biotechnology 2000;54(3):287-301.
29. Wiebe MG, Robson GD, Shuster J, Trinci APJ. Evolution of a recombinant (gucoamylase-producing) strain of Fusarium venenatum A3/5 in chemostat culture. Biotechnology and Bioengineering 2001;73(2):146-156.

30. Novick A, Szilard L. Experiments with the Chemostat on Spontaneous Mutations of Bacteria. *Proceedings of the National Academy of Sciences of the United States of America* 1950;36(12):708-719.
31. Lane PG, Oliver SG, Buttlar PR. Analysis of a Continuous-Culture Technique for the Selection of Mutants Tolerant to Extreme Environmental Stress. *Biotechnology and Bioengineering* 1999;65(4):397-406.
32. Qu MB, Bhattacharya SK. Toxicity and biodegradation of formaldehyde in anaerobic methanogenic culture. *Biotechnology and Bioengineering* 1997;55(5):727-736.
33. Costerton JW, Lewandowski Z, Caldwell DE, Korber DR, Lappinscott HM. Microbial Biofilms. *Annual Review of Microbiology* 1995;49:711-745.
34. Hancock REW. A brief on bacterial biofilms. *Nature Genetics* 2001;29(4):360-360.
35. Lawrence JR, Korber DR, Hoyle BD, Costerton JW, Caldwell DE. Optical Sectioning of Microbial Biofilms. *Journal of Bacteriology* 1991;173(20):6558-6567.
36. Topiwala HH, Hamer C. Effect of Wall Growth in Steady-State Continuous Culture. *Biotechnology and Bioengineering* 1971;13(6):919-922.
37. Larsen DH, Dimmick RL. Attachment and Growth of Bacteria on Surfaces of Continuous-Culture Vessels. *Journal of Bacteriology* 1964;88(5):1380-1387.
38. Zhe J, Jagtiani A, Dutta P, Hu J, Carletta J. A micromachined high throughput Coulter counter for bioparticle detection and counting. *Journal of Micromechanics and Microengineering* 2007;17(2):304-313.

39. Yokobayashi Y, Collins CH, Leadbetter JR, Weiss R, Arnold FH.
Evolutionary Design of Genetic Circuits and Cell-Cell Communication.
Advances in Complex Systems 2002;6(1):1-9.
40. Ingraham JL, Maaloe O, Niedhardt FC. In: Growth of the Bacterial Cell.
Sunderland: Sinauer Associates, Inc.; 1983. p. 230.
41. Carbonell X, Corchero JL, Cubarsi R, Vila P, Villaverde A. Control of
Escherichia coli growth rate through cell density. Microbiological Research
2002;157(4):257-265.
42. Squires TM, Quake SR. Microfluidics: Fluid physics at the nanoliter scale.
Reviews of Modern Physics 2005;77(3):977-1026.
43. Thorsen T, Maerkl SJ, Quake SR. Microfluidic large-scale integration.
Science 2002;298(5593):580-584.
44. Whitesides GM. The origins and the future of microfluidics. Nature
2006;442(7101):368-373.
45. Balagadde F.
46. Zhang ZY, Boccazzi P, Choi HG, Perozziello G, Sinskey AJ, Jensen KF.
Microchemostat - microbial continuous culture in a polymer-based,
instrumented microbioreactor. Lab on a Chip 2006;6(7):906-913.
47. Hansen CL. Microfluidic Technologies for Structural Biology. Pasadena:
California Institute of Technology; 2004.
48. Szita N, Zanzotto A, Boccazzi P, Sinskey AJ, Schmidt MA, Jensen KF.
Monitoring of Cell Growth, Oxygen and pH in Microfermentors. In: Baba Y,
Shoji S, Berg Avd, editors. Micro Total Analysis Systems 2002; 2002; Nara,
Japan: Kluwer Academic Publishers; 2002. p. 7-9.

49. Zanzotto A, Szita N, Boccazzi P, Lessard P, Sinskey AJ, Jensen KF. Membrane-Aerated Microbioreactor for High-Throughput Bioprocessing. *Biotechnology and Bioengineering* 2004;87(2):243-254.
50. Andrianantoandro E, Basu S, Karig DK, Weiss R. Synthetic biology: new engineering rules for an emerging discipline. *Molecular Systems Biology* 2006.
51. Baker D, Group BF, Church G, Collins J, Endy D, Jacobson J, et al. Engineering life: Building a fab for biology. *Scientific American* 2006;294(6):44-51.
52. You LC, Cox RS, Weiss R, Arnold FH. Programmed population control by cell-cell communication and regulated killing. *Nature* 2004;428(6985):868-871.
53. Basu S, Gerchman Y, Collins CH, Arnold FH, Weiss R. A synthetic multicellular system for programmed pattern formation. *Nature* 2005;434(7037):1130-1134.
54. Balagadde FK, Hao S, Ozaki J, Collins CH, Barnett M, Arnold FH, et al. A synthetic predator-prey ecosystem. In preparation.
55. Elowitz MB, Leibler S. A synthetic oscillatory network of transcriptional regulators. *Nature* 2000;403(6767):335-338.
56. McDaniel R, Weiss R. Advances in synthetic biology: on the path from prototypes to applications. *Current Opinion in Biotechnology* 2005;16(4):476-483.
57. Marguet P, Balagadde F, Tan CM, You L. Biology by design: reduction and synthesis of cellular components and behavior. *Journal of the Royal Society Interface* 2007.

58. You LC. Towards Computational Systems Biology. *Cell Biochemistry and Biophysics* 2004(40):167-184.
59. Neilson KH, Hastings JW. Bacterial Bioluminescence - Its Control and Ecological Significance. *Microbiological Reviews* 1979;43(4):496-518.
60. Miller MB, Bassler BL. Quorum sensing in bacteria. *Annual Review of Microbiology* 2001;55:165-199.
61. de Kievit TR, Iglewski BH. Bacterial Quorum Sensing in Pathogenic Relationships. *Infect. Immun.* 2000;68(9):4839-4849.
62. Drenkard E, Ausubel FM. Pseudomonas biofilm formation and antibiotic resistance are linked to phenotypic variation. *Nature* 2002;416(6882):740-743.
63. Fuqua C, Parsek MR, Greenberg EP. Regulation of gene expression by cell-to-cell communication: Acyl-homoserine lactone quorum sensing. *Annual Review Of Genetics* 2001;35:439-468.
64. Taga ME, Bassler BL. Chemical communication among bacteria. *Proceedings Of The National Academy Of Sciences Of The United States Of America* 2003;100:14549-14554.
65. Engebrecht J, Silverman M. Nucleotide-Sequence of the Regulatory Locus Controlling Expression of Bacterial Genes for Bioluminescence. *Nucleic Acids Research* 1987;15(24):10455-10467.
66. Engebrecht J, Silverman M. Identification of Genes and Gene-Products Necessary for Bacterial Bioluminescence. *Proceedings of the National Academy of Sciences of the United States of America-Biological Sciences* 1984;81(13):4154-4158.

67. Engebrecht J, Nealson K, Silverman M. Bacterial Bioluminescence - Isolation and Genetic-Analysis of Functions from *Vibrio Fischeri*. *Cell* 1983;32(3):773-781.
68. McNab R, Lamont RJ. Microbial dinner-party conversations: the role of LuxS in interspecies communication. *Journal of Medical Microbiology* 2003;52(7):541-545.
69. Federle MJ, Bassler BL. Interspecies communication in bacteria. *J. Clin. Invest.* 2003;112(9):1291-1299.
70. You LC, Cox RSI, Weiss R, Arnold FH. Programmed population control by cell-cell communication and regulated killing. *Nature* 2004;428(6985):868-871.
71. Weiss R, Knight TF. Engineering Communications for Microbial Robotics. In: Rozenberg G, editor. *Proceedings of the Sixth International Meeting on DNA-Based Computers*; 2000; Leiden, The Netherlands; 2000.
72. Collins CH, Arnold FH, Leadbetter JR. Directed evolution of *vibrio fischeri* LuxR for increased sensitivity to a broad spectrum of acyl-homoserine lactones. *Molecular Microbiology* 2004;0(0):-doi: 10.1111/j.1365-2958.2004.04437.x.
73. Lutz R, Bujard H. Independent and tight regulation of transcriptional units in *Escherichia coli* via the LacR/O, the TetR/O and AraC/I-1-I-2 regulatory elements. *Nucleic acids research* 1997;25(6):1203-1210.
74. Eglund KA, Greenberg EP. Quorum sensing in *Vibrio fischeri*: elements of the luxI promoter. *Molecular Microbiology* 1999;31(4):1197-1204.
75. You L.

76. You L, Hoonlor A, Yin J. Modeling biological systems using Dynetica – a simulator of dynamic networks. *Bioinformatics* 2003(19):435-436.
77. Colinvaux P. *Ecology*, 2nd Edition. 2 ed: John Wiley & Sons; 1993.
78. Ricklefs R, Miller G. *Ecology*, 4th Edition: W. H. Freeman; 1999.
79. Murray JD. *Mathematical Biology*, 3rd Edition: Springer; 2002.
80. Colinvaux P. *Ecology*, 2nd edition: John Wiley & Sons; 1993.
81. Ricklefs RE, Miller G. *Ecology*, 4th edition: W. H. Freeman; 1999.
82. Gilg O, Hanski I, Sittler B. Cyclic dynamics in a simple vertebrate predator-prey community. *Science* 2003;302(5646):866-8.
83. Sinclair AR, Mduma S, Brashares JS. Patterns of predation in a diverse predator-prey system. *Nature* 2003;425(6955):288-90.
84. McCauley E, Murdoch WW. Predator-prey dynamics in environments rich and poor in nutrients. *Nature* 1990;343:455-457.
85. Fussmann GF, Ellner SP, Shertzer KW, Hairston NG, Jr. Crossing the hopf bifurcation in a live predator-prey system. *Science* 2000;290(5495):1358-60.
86. Becks L, Hilker FM, Malchow H, Jurgens K, Arndt H. Experimental demonstration of chaos in a microbial food web. *Nature* 2005;435(7046):1226-9.
87. Yoshida T, Jones LE, Ellner SP, Fussmann GF, Hairston NG, Jr. Rapid evolution drives ecological dynamics in a predator-prey system. *Nature* 2003;424(6946):303-6.
88. Nelson WA, McCauley E, Wrona FJ. Stage-structured cycles promote genetic diversity in a predator-prey system of *Daphnia* and algae. *Nature* 2005;433(7024):413-7.
89. Abbott A. Microbiology: gut reaction. *Nature* 2004;427(6972):284-6.

90. Whitfield J. The ulcer bug: Gut reaction. *Nature* 2003;423(6940):583-4.
91. Lutz R, Bujard H. Independent and tight regulation of transcriptional units in *Escherichia coli* via the LacR/O, the TetR/O and AraC/I1-I2 regulatory elements. *Nucleic Acids Res* 1997;25(6):1203-10.
92. Eglund KA, Greenberg EP. Quorum sensing in *Vibrio fischeri*: elements of the luxI promoter. *Molecular Microbiology* 1999;31(4):1197-204.
93. Engelberg-Kulka H, Glaser G. Addiction modules and programmed cell death and antideath in bacterial cultures. *Annual Review Of Microbiology* 1999;53:43-70.
94. Fuqua C, Parsek MR, Greenberg EP. Regulation of gene expression by cell-to-cell communication: acyl-homoserine lactone quorum sensing. *Annual Review of Genetics* 2001;35:439-68.
95. Miller MB, Bassler BL. Quorum sensing in bacteria. *Annual Review of Microbiology* 2001;55:165-99.
96. You L, Cox RS, 3rd, Weiss R, Arnold FH. Programmed population control by cell-cell communication and regulated killing. *Nature* 2004;428(6985):868-71.
97. Gray KM, Passador L, Iglewski BH, Greenberg EP. Interchangeability and specificity of components from the quorum-sensing regulatory systems of *Vibrio fischeri* and *Pseudomonas aeruginosa*. *Journal of Bacteriology* 1994;176(10):3076-80.
98. Balagadde FK, You L, Hansen CL, Arnold FH, Quake SR. Long-term monitoring of bacteria undergoing programmed population control in a microchemostat. *Science* 2005;309(5731):137-40.

99. Eglund KA, Greenberg EP. Conversion of the *Vibrio fischeri* transcriptional activator, LuxR, to a repressor. *J Bacteriol* 2000;182(3):805-11.
100. Collins CH. unpublished data.
101. Zhu J, Winans SC. Autoinducer binding by the quorum-sensing regulator TraR increases affinity for target promoters in vitro and decreases TraR turnover rates in whole cells. *Proc Natl Acad Sci U S A* 1999;96(9):4832-7.
102. May RM. *Stability and complexity in model ecosystems*. 2 ed. Princeton, NJ, USA: Princeton University Press; 1974.
103. Basu S, Gerchman Y, Collins CH, Arnold FH, Weiss R. A synthetic multicellular system for programmed pattern formation. *Nature* 2005;434(7037):1130-4.
104. Chang CY, Nam K, Young R. S gene expression and the timing of lysis by bacteriophage lambda. *J Bacteriol* 1995;177(11):3283-94.
105. Kaplan HB, Greenberg EP. Diffusion of autoinducer is involved in regulation of the *Vibrio fischeri* luminescence system. *J Bacteriol* 1985;163(3):1210-4.
106. Schaefer AL, Val DL, Hanzelka BL, Cronan JE, Jr., Greenberg EP. Generation of cell-to-cell signals in quorum sensing: acyl homoserine lactone synthase activity of a purified *Vibrio fischeri* LuxI protein. *Proc Natl Acad Sci U S A* 1996;93(18):9505-9.
107. Schaefer AL, Hanzelka BL, Parsek MR, Greenberg EP. Detection, purification, and structural elucidation of the acylhomoserine lactone inducer of *Vibrio fischeri* luminescence and other related molecules. *Methods Enzymol* 2000;305:288-301.

108. Dong YH, Wang LH, Xu JL, Zhang HB, Zhang XF, Zhang LH. Quenching quorum-sensing-dependent bacterial infection by an N-acyl homoserine lactonase. *Nature* 2001;411(6839):813-7.
109. Leadbetter JR, Greenberg EP. Metabolism of acyl-homoserine lactone quorum-sensing signals by *Variovorax paradoxus*. *J Bacteriol* 2000;182(24):6921-6.
110. Collins CH, Arnold FH, Leadbetter JR. Directed evolution of *Vibrio fischeri* LuxR for increased sensitivity to a broad spectrum of acyl-homoserine lactones. *Mol Microbiol* 2005;55(3):712-23.
111. Elowitz MB, Leibler S. A synthetic oscillatory network of transcriptional regulators. *Nature* 2000;403(6767):335-8.
112. Weiss R, Knight TFJ. Engineered Communications for Microbial Robotics. In: *DNA6: Sixth International Meeting on DNA Based Computers*; 2000 June 2000: Springer-Verlag; 2000. p. 1-16.
113. Weiss R. Cellular Computation and Communication Using Engineered Genetic Regulatory Networks. [Ph.D. thesis]: Massachusetts Inst. Technology; 2001.
114. Webre DJ, Wolanin PM, Stock JB. Bacterial chemotaxis. *Current Biology* 2003;13(2):R47-R49.
115. Adler J, Tso WW. Decision-Making in Bacteria - Chemotactic Response of *Escherichia-Coli* to Conflicting Stimuli. *Science* 1974;184(4143):1293-1294.
116. Wadhams GH, Armitage JP. Making sense of it all: Bacterial chemotaxis. *Nature Reviews Molecular Cell Biology* 2004;5(12):1024-1037.

117. Alon U, Surette MG, Barkai N, Leibler S. Robustness in bacterial chemotaxis. *Nature* 1999;397(6715):168-171.
118. Gosink KK, Buron-Barral MD, Parkinson JS. Signaling interactions between the aerotaxis transducer Aer and heterologous chemoreceptors in *Escherichia coli*. *Journal of Bacteriology* 2006;188(10):3487-3493.
119. Lai WC, Hazelbauer GL. Carboxyl-terminal extensions beyond the conserved pentapeptide reduce rates of chemoreceptor adaptational modification. *Journal of Bacteriology* 2005;187(15):5115-5121.
120. Hendrixson DR, DiRita VJ. Identification of *Campylobacter jejuni* genes involved in commensal colonization of the chick gastrointestinal tract. *Molecular Microbiology* 2004;52(2):471-484.
121. Reinhold B, Hurek T, Fendrik I. Strain-Specific Chemotaxis of *Azospirillum* Spp. *Journal of Bacteriology* 1985;162(1):190-195.
122. Stanton TB, Savage DC. Motility as a Factor in Bowel Colonization by *Roseburia-Cecicola*, an Obligately Anaerobic Bacterium from the Mouse Cecum. *Journal of General Microbiology* 1984;130(JAN):173-183.
123. Tolliver JL, Schafer AL, Ruby EG, DeLoney-Marino CR. Characterization of chemotaxis to the chitin oligosaccharide chitoboise in *Vibrio fischeri*. In: American Society for Microbiology, 106th General Meeting Abstracts, Abstract I-075; 2006; Orlando, FL, U.S.A; 2006.
124. Hotic S, Luercio M, Ram J, L. Differences in low agar density (swarm plate) responses of *Escherichia coli* isolated from different hosts. In: American Society for Microbiology, 106th General Meeting, vol 2006, poster number: I-088; 2006; Orlando, FL., U.S.A; 2006.

125. Freter R, Brickner H, Fekete J, Vickerman MM, Carey KE. Survival and Implantation of *Escherichia-Coli* in the Intestinal-Tract. *Infection and Immunity* 1983;39(2):686-703.
126. Freter R, O'Brien PCM. Role of Chemotaxis in the Association of Motile Bacteria with Intestinal-Mucosa - Chemotactic Responses of *Vibrio-Cholerae* and Description of Motile Non-Chemotactic Mutants. *Infection and Immunity* 1981;34(1):215-221.
127. Lane M, Lloyd AL, Markyvech TA, Hagan EC, Mobley HLT. Uropathogenic *Escherichia coli* generally lack functional Trg and Tap methyl-accepting chemotaxis receptors found in nearly all diarrheagenic and commensal strains. In: American Society for Microbiology, 106th General Meeting Abstracts, pp. Abstract B-172; 2006; Orlando, FL., U.S.A; 2006.
128. Falke JJ, Hazelbauer GL. Transmembrane signaling in bacterial chemoreceptors. *Trends in Biochemical Sciences* 2001;26(4):257-265.
129. Parkinson JS, Ames P, Studdert CA. Collaborative signaling by bacterial chemoreceptors. *Current Opinion in Microbiology* 2005;8(2):116-121.
130. Quezada CM, Hamel DJ, Gradinaru C, Bilwes AM, Dahlquist FW, Crane BR, et al. Structural and chemical requirements for histidine phosphorylation by the chemotaxis kinase CheA. *Journal of Biological Chemistry* 2005;280(34):30581-30585.
131. Francis NR, Wolanin PM, Stock JB, DeRosier DJ, Thomas DR. Three-dimensional structure and organization of a receptor/signaling complex. *Proceedings of the National Academy of Sciences of the United States of America* 2004;101(50):17480-17485.

132. Alexandre G, Zhulin IB. Different evolutionary constraints on chemotaxis proteins CheW and CheY revealed by heterologous expression studies and protein sequence analysis. *Journal of Bacteriology* 2003;185(2):544-552.
133. Boukhvalova MS, Dahlquist FW, Stewart RC. CheW binding interactions with CheA and Tar - Importance for chemotaxis signaling in *Escherichia coli*. *Journal of Biological Chemistry* 2002;277(25):22251-22259.
134. Palleroni NJ. Chamber for Bacterial Chemotaxis Experiments. *Applied and Environmental Microbiology* 1976;32(5):729-730.
135. Harshey RM. Bees Arent the Only Ones - Swarming in Gram-Negative Bacteria. *Molecular Microbiology* 1994;13(3):389-394.
136. Henrichs J. Bacterial Surface Translocation - Survey and a Classification. *Bacteriological Reviews* 1972;36(4):478-503.
137. Williams FD, Schwarzhoff RH. Nature of Swarming Phenomenon in *Proteus*. *Annual Review of Microbiology* 1978;32:101-122.
138. Berg HC. The rotary motor of bacterial flagella. *Annual Review of Biochemistry* 2003;72:19-54.
139. Staropoli JF, Alon U. Computerized analysis of chemotaxis at different stages of bacterial growth. *Biophysical Journal* 2000;78(1):513-519.
140. Diao JP, Young L, Kim S, Fogarty EA, Heilman SM, Zhou P, et al. A three-channel microfluidic device for generating static linear gradients and its application to the quantitative analysis of bacterial chemotaxis. *Lab on a Chip* 2006;6(3):381-388.

141. Mao HB, Cremer PS, Manson MD. A sensitive, versatile microfluidic assay for bacterial chemotaxis. *Proceedings of the National Academy of Sciences of the United States of America* 2003;100(9):5449-5454.
142. Polen T, Rittmann D, Wendisch VF, Sahm H. DNA Microarray analyses of the long-term adaptive response of *Escherichia coli* to acetate and propionate. *Applied and Environmental Microbiology* 2003;69(3):1759-1774.